GRID CONNECTION OF WIND-SOLAR HYBRID RENEWABLE ENERGY SYSTEM, WITH ACTIVE POWER FILTER FUNCTIONALITY

Thesis

Submitted in partial fulfilment of the requirements for the degree of

DOCTOR OF PHILOSOPHY

by

JAYASANKAR V N

DEPARTMENT OF ELECTRICAL AND ELECTRONICS

ENGINEERING, NATIONAL INSTITUTE OF

TECHNOLOGY KARNATAKA, SURATHKAL,

MANGALORE - 575025

March 2019

DECLARATION

by the Ph.D. Research Scholar

I hereby declare that the Research Thesis entitled **Grid Connection of Wind-Solar Hybrid Renewable Energy System, with Active Power Filter Functionality** which is being submitted to the National Institute of Technology Karnataka, Surathkal in partial fulfilment of the requirements for the award of the degree of **Doctor of Philosophy** in **Electrical & Electronics Engineering** is a bonafide report of the research work carried out by me. The material contained in this Research Thesis has not been submitted to any University or Institution for the award of any degree.

148026EE14F08, Jayasankar V N

(Register Number, Name and Signature of the Research Scholar)

Department of Electrical & Electronics Engineering

Place: NITK-Surathkal

Date: 01-03-2019

CERTIFICATE

This is to certify that the Research Thesis entitled **Grid Connection of Wind-Solar Hybrid Renewable Energy System, with Active Power Filter Functionality** submitted by **Mr. Jayasankar V N** (Register Number: **148026EE14F08**) as the record of the research work carried out by him, is accepted as *the Research Thesis submission* in partial fulfilment of the requirements for the award of the degree of **Doctor of Philosophy**.

Research Guide(s)

(Name and Signature with Date and Seal)

Chairman-DRPC

(Signature with Date and Seal)

Acknowledgement

Dhanyasree, daughter Adwika and brother Shyam Krishnan for encouraging me and keeping me enthusiastic. I am also grateful to my in laws, other family members and friends who have supported me along the way.

And last but by no means least, I would like to express my heartfelt gratitude to all my well-wishers. Thank you all for all your encouragement.

Abstract

The incorporation of the abundantly available wind and solar energy to the grid using power electronic converter based interfaces makes a reliable hybrid renewable energy system. Assigning harmonic mitigation property to the grid interfacing inverter to mitigate the current harmonics created by the non-linear loads at the load centres, is a cost-effective solution. The inverter controller consists of an outer DC-link voltage control loop and an inner current harmonic mitigation loop. The limitations of existing DC-link voltage controllers are poor stability margin, steady-state error and chattering problem. The widely used pq theory based inner loop controller offers poor performance under non-ideal grid voltage conditions. The conventional low pass filter based fundamental component extraction methods used in pq theory possess some limitations such as additional time delays and low-frequency oscillations.

The main focus of this research is the design, simulation, implementation and analysis of a grid-tied wind-solar hybrid renewable energy system with shunt and series active filtering functionalities, under different system conditions. A Backstepping controller based outer loop, with enhanced DC-link loss compensation capability is proposed for the shunt active filter to overcome the limitations of the existing DC-link voltage controllers. The limitations of conventional low pass filter based fundamental component extraction methods are overcome by employing a self-tuning filter in the inner loop of the shunt active filter. An additional self-tuning filter is incorporated to improve the effectiveness of pq theory under non-ideal grid conditions. A self-tuning filter and a Fuzzy logic-based voltage controller are employed to control the series active filter effectively. A laboratory prototype of the shunt active power filter is implemented. The control algorithm is realised in Xilinx Basys-3 FPGA.

From the simulation and hardware test results under steady-state and dynamic conditions, it is found that the proposed controller offers better stability, robustness and speed compared to other existing control methods.

Keywords: Power quality, Active power filter, Grid-tied renewable system, Backstepping Control, Dual Self Tuning Filter, Fuzzy logic, DC-link voltage control.

Contents

List of Figures

viii

x

List of Tables

List of Abbreviations

AC	Alternating Current
ADC	Analog to Digital Converter
ANF	Adaptive Notch Filter
ANN	Artificial Neural Network
ASF	Adaptable Sampling Frequency
BSC	Backstepping Controller
DC	Direct Current
DFIG	Doubly Fed Induction Generator
DFT	Discrete Fourier Transform
DG	Distributed Generation
DSP	Digital Signal Processor
DSTF	Dual Self Tuning Filter
FACTS	Flexible Alternating Current Transmission System
FFT	Fast Fourier Transform
FPGA	Field Programmable Gate Array
IEEE	Institute of Electrical & Electronics Engineers
IGBT	Insulated Gate Bipolar Transistor
LPF	Low Pass Filter
MPPT	Maximum Power Point Tracking
PCC	Point of Common Coupling
PI	Proportional Integral
PLL	Phase Locked Loop
PMSG	Permanent Magnet Synchronous Generator

PSO	Particle Swarm Optimization
PSSR	Positive Sequence Sinusoidal Regulator
PV	Photovoltaic
PWM	Pulse Width Modulation
QPLL	Quadrature Phase Locked Loop
RAM	Random Access Memory
RES	Renewable Energy Source
RMS	Root Mean Square
SAPF	Series Active Power Filter
SHAF	Shunt Active Power Filter
SMC	Sliding Mode Control
STF	Self Tuning Filter
SV	Space Vector
TDD	Total Demand Distortion
THD	Total Harmonic Distortion
UPQC	Unified Power Quality Conditioner
VSI	Voltage Source Inverter
XADC	Xilinx Analog to Digital Converter
ZCD	Zero Crossing Detection

List of Nomenclature

β	Blade pitch angle (deg)
η	Turbine efficiency (%)
λ	Tip speed ratio
ω	Supply frequency(rad/s)
ω_e	Electrical rotating speed (rad/s)
ω_{nv}	Natural frequency of undamped oscillations(rad/s)
ω_s	Wind turbine power (W)
ω_w	Turbine rotor speed (rad/s)
Ψ_f	Permanent magnet flux (Wb)
ρ	Air density (kg/m^3)
ζ	Damping constant of PI controller
a	Diode constant ($1 \leq a \leq 1.5$)
A	Rotor area of wind turbine (m^2)
C_b	Capacitance of boost converter (F)
C_{dc}	Capacitance of DC-link capacitor (F)
C_P	Power Co-efficient
d	Duty ratio
f_{max}	Maximum switching frequency (Hz)
f_s	Switching frequency (Hz)
G_n	Nominal irradiation level (W/m^2)
G	Irradiation level (W/m^2)
h	Hysteresis band
I_0	Saturation Current (A)

i_{dc}^{abc}	DC voltage controller currents in abc frame (A)
$i_L^{\alpha\beta 0}$	Load currents in $\alpha\beta$ frame (A)
i_L^{abc}	Load currents in abc frame (A)
$i_{L1}^{\alpha\beta}$	Fundamental components of load currents (A)
$i_{Lh}^{\alpha\beta}$	Harmonic components of load currents (A)
I_{PV}	Photovoltaic Current (A)
I_{PVn}	Nominal Photovoltaic Current (A)
i_{ref}^{abc}	Reference currents for pulse generation (A)
I_{sc}	Short circuit current of PV cell (A)
I_{scn}	Nominal short circuit current of PV cell (A)
k_p, k_i	Proportional and integral gains of PI controller
K_i	Temperature co-efficient of current (A/K)
K_v	Temperature co-efficient of voltage (V/K)
k	Boltzmann Constant
L_b	Inductance of boost converter (H)
L_d, L_q	Inductance of PMSG on d and q axes (H)
L_f	Filter inductance (H)
N_p	Number of parallel and series PV cells
N_s	Number of series PV cells
p_h	Instantaneous real power needed for harmonic compensation (W)
P_{Rdc}	The losses in leakage resistance of dc link capacitor (W)
P_{RES}	The power injected by renewable sources (W)
P_{sw}	The inverter switching loss (W)
P_w	Wind turbine power (W)
P_s	The power supplied to maintain the charge in dc link capacitor (W)
p	Number of pole pairs of PMSG
q_e	Charge of electron (C)
q	Instantaneous reactive power (VAr)
R_b	Load resistance of boost converter (Ω)
R_p	Shunt resistance of PV cell (Ω)

R_s	Series resistance of PV cell (Ω)	
R_{st}	Stator resistance of PMSG (Ω)	
R	Radius of turbine rotor (m)	
T_w	Aerodynamic torque of wind turbine (Nm)	
T_e	Electromagnetic torque of PMSG (Nm)	
U_{abc}	Unit amplitude voltages in abc frame (V)	
V_{dc}	DC link voltage (V)	
V_{dcref}	DC-link voltage reference(V)	
v_f^{abc}	Compensating voltages of series active filter (V)	
V_{fref}^{abc}	Reference voltages of series active filter (V)	
V_i	Input voltage of boost converter (V)	
V_o	Output voltage of boost converter (V)	
V_{oc}	Open circuit voltage of PV cell (V)	
V_{ocn}	Nominal open circuit voltage of PV cell (V)	
$v_s^{\alpha\beta}$	Grid voltages in $\alpha\beta$ frame (V)	
v_s^{abc}	Grid voltages in abc frame (V)	
v_{sp1}^{abc}	Fundamental positive sequence components of grid voltage in abc frame (V)	
V_t	Thermal Voltage of the PV cell (V)	
v_w	Velocity of wind (m/s)	
v	Pitch angle (deg)	

Chapter 1

Introduction

1.1 THE BACKGROUND OF THE RESEARCH

The global increase in energy demand and depleting fossil fuel resources motivate the energy engineers to find a sustainable solution. Renewable energy sources (RES) opens a wide possibility in this context. RES can be in islanded mode or grid-connected mode. However, the need for energy storage devices such as a battery, and the capital cost, maintenance cost and chemical pollution associated with the battery make the islanded mode less feasible for large and medium scale energy generation. The injection of the generated power directly into the main grid at the distribution level assures the maximum utilisation of the locally available RES. As the wind and solar energy are complementary to each other in availability, a hybrid combination of both are preferred for a more reliable power system.

The recent trend in the area of grid-connected RES system is assigning an additional responsibility of an active power filtering to the grid interfacing inverter. The proliferation of power electronic converters aggravated the non-linearity of load centres and deteriorated the quality of grid current at the point of common coupling (PCC). The shunt active power filter (SHAF) is a common solution to improve the quality of grid current and brings the current THD within the permissible limit. The use of grid interfacing system as SHAF is a cost-effective way of power quality enhancement. However,

some of the common power quality issues in distribution systems such as sag, swell and distortions in voltage cannot be addressed by SHAF. Employing an additional series active power filter (SAPF) resolves this issue.

1.2 LITERATURE REVIEW

The existing topologies of wind and solar energy systems, their grid integration using voltage source inverter and the control methods for grid interfacing inverter are the major focus of this survey. Different power quality problems, their mitigation using active filters and the control methods of active filters proposed so far in literature are also studied. The Figure 1.1 shows the overall picture of the literature survey.

1.2.1 Wind Energy System

The wind turbine is the basic component of a wind energy system. It converts the energy available in flowing air mass to mechanical power (Anderson and Bose, 1983). The wind turbine is coupled with an AC generator to convert the generated mechanical power to electrical power. Other accessory components of the wind energy system are rotor speed controllers, pitch angle controllers, voltage controllers and protection system.

The wind turbine operates in variable speed conditions as the wind speed is varying in nature. De-coupling of electrical grid frequency and mechanical rotor frequency using AC-DC and DC-AC converters was a breakthrough in wind energy system technology. Slootweg et al. (2003) proposes the wind turbine coupled with a doubly fed induction generators (DFIG), employed with a three-phase controlled rectifier-inverter circuit at rotor side. In this topology, the rotor output power is supplied to the main grid using the power converter. The main limitation of this topology is that the wind turbine cannot operate in full range, as the converter size is commonly smaller than the machine size. For achieving a speed variation of around 60% of synchronous speed, the power converter rating needs to be about 30% of the nominal power of DFIG. An alternate topology with a power converter connected at stator side is put forward by Orabi et al. (2004). In this topology, the energy from the generator is rectified to a DC-link

2
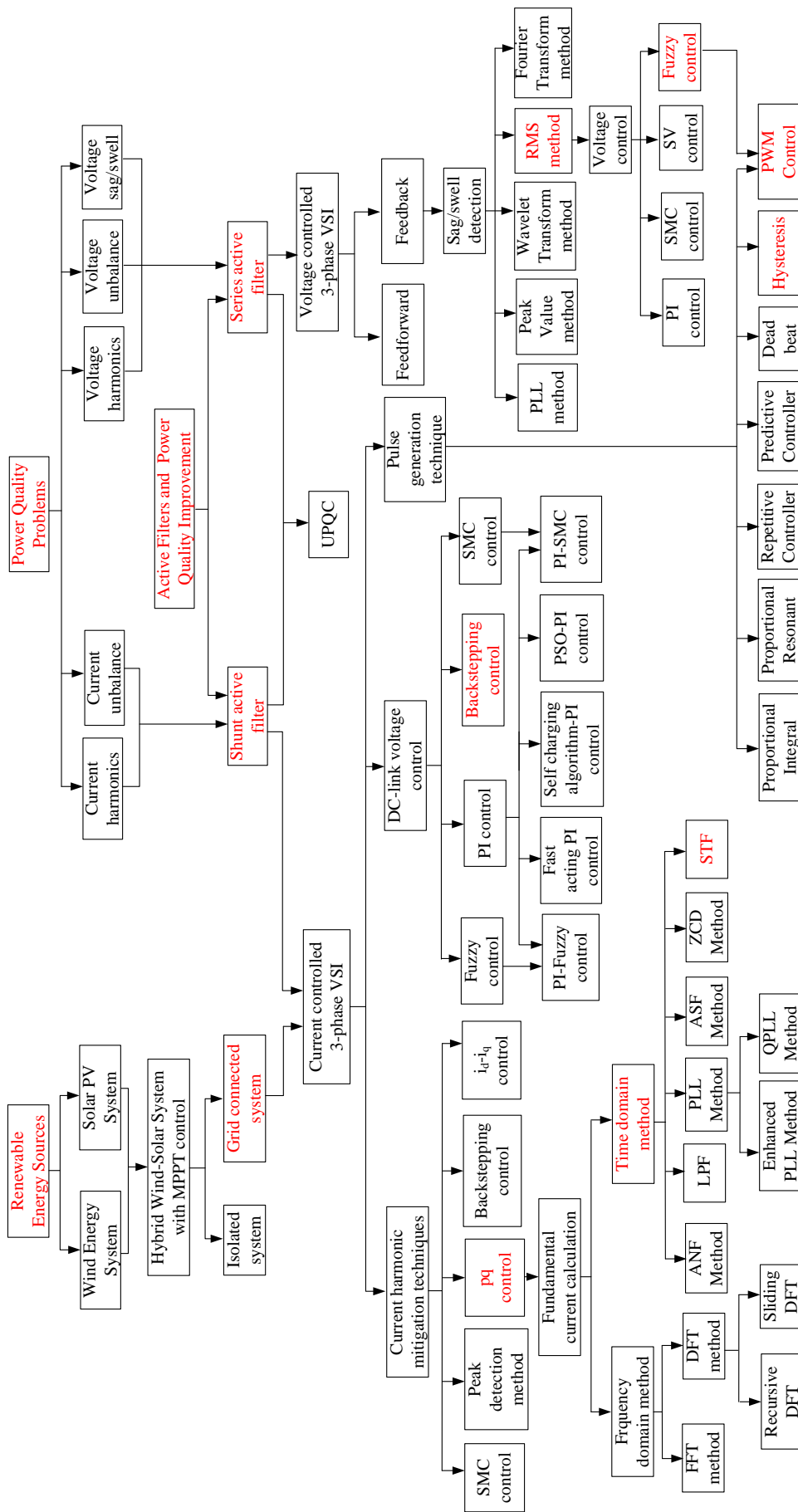
Figure 1.1: Literature review tree

and converted it to a suitable AC energy. The rectifier controls the machine torque and speed, whereas inverter controls the active and reactive power delivered to the grid. The advantage of this scheme from the previous topology is that the rotor can operate in a higher range of frequencies. In the topology proposed by Carrasco et al. (2006), a multipole synchronous generator is used. An uncontrolled rectifier cascaded with a step up chopper is used in place of the controlled converter. In this topology, any change in synchronous generator speed is reflected in DC-link voltage. The step-up chopper adapts the rectifier voltage to the DC-link voltage of the inverter. The machine torque and speed are controlled by controlling the chopper inductor current. The reduction in cost is the main advantage of this topology compared to the DFIG based topology. Replacing the synchronous generator by permanent magnet synchronous generator (PMSG) is another alternate topology (Blaabjerg et al., 2006; Patil and Mehta, 2014). The main advantage of using PMSG is that the gearbox can be eliminated and thereby overall weight and cost can be reduced. This improves the overall system performance and efficiency.

1.2.2 Solar Energy System

The solar photovoltaic panel is the basic component of a solar energy system, which converts the energy available in sunlight into electrical energy. The solar PV panels are connected in series-parallel fashion in order to meet the specific power requirement. Power electronic interfaces such as DC-DC converter and inverter are necessary for the grid integration of solar PV modules to facilitate effective power transfer.

The central inverter scheme, string inverter scheme, multi-string inverter scheme, the module integrated inverter scheme are some of the available schemes in literature for PV panel grid integration based on the inverter design. In the central inverter scheme, one universal inverter is used for the entire PV plant (Blaabjerg et al., 2006; Ding et al., 2010). The disadvantage of this topology is that power output may decrease due to factors such as partial shading and module mismatching. Moreover, the reliability is limited, as the entire plant depends on a single inverter, failure of which results in plant outage. In the string inverter scheme, the PV panels are connected as parallel

4

strings, with each string equipped with a string inverter. In this scheme, each string inverters possess maximum power point tracking (MPPT) capability. As a result, partial shading and module mismatching effects are reduced. Also, reliability is enhanced in this scheme. In the multi-string inverter scheme, each string is equipped with a DC-DC converter. A central inverter is employed for the entire plant. This scheme has the combined advantages of central and string inverter schemes. In the module integrated PV connection scheme, the individual solar PV modules are connected to dedicated inverters. The energy yield of the system is enhanced. However, the cost and maintenance efforts are more in this scheme (Carrasco et al., 2006).

1.2.3 Hybrid Renewable Energy System

The sustainability and reliability of power generation can be improved by combining wind and solar energy system. The AC-shunted scheme and DC-shunted scheme are the two different grid integration schemes of the hybrid wind-solar system, reported in the literature. The AC-shunted scheme consists of a dedicated DC-DC converter and an inverter for both wind and solar systems, whereas in the DC-shunted scheme, a common inverter is used. The rating of the inverter in DC shunted scheme is usually less than the total power rating of two inverters in AC shunted scheme (Chen et al., 2006).

The recent trend in the area of the grid-connected hybrid renewable system is assigning the additional responsibility of power quality mitigation to the grid interfacing inverter. Different power quality problems, their mitigation techniques and power quality standards are discussed in following subsections.

1.2.4 Power quality problems

According to IEEE-1159 (2009), "The term power quality refers to a wide variety of electromagnetic phenomena that characterise the voltage and current at a given time and a given location on the power system". The common power quality problems and the causes of occurrence are listed in table 1.1 (IEEE-1159, 2009).

5

Table 1.1: Categories and typical characteristics of power quality problems

Categories	Duration	Magnitude	Causes
Long duration rms variation			
1.1 Interruption	> 1 min	0.0 pu	
1.2 Undervoltage	> 1 min	0.8-0.9 pu	Switching off a large load, switching on a capacitor bank
1.3 Overvoltage	> 1 min	1.1-1.2 pu	Load switching on, switching off a capacitor bank
Short duration rms variation			
2.1 Interruption			Power system faults, equipment failures, control malfunctions
2.1.1 Momentary	0.5 cycles-3 s	< 0.1 pu	
2.1.2 Temporary	3 s - 1 min	< 0.1 pu	
2.2 Sag			System faults, switching on heavy loads, starting of large motors
2.2.1 Instantaneous	0.5-30 cycles	0.1-0.9 pu	
2.2.2 Momentary	30 cycles-3 s	0.1-0.9 pu	
2.2.3 Temporary	3 s - 1 min	0.1-0.9 pu	
2.3 Swell			System fault, large load switching off , load shedding, large capacitor bank switching on
2.3.1 Instantaneous	0.5-30 cycles	1.1-1.8 pu	
2.3.2 Momentary	30 cycles-3 s	1.1-1.4 pu	
2.3.3 Temporary	3 s - 1 min	1.1-1.2 pu	

... continued

Categories	Duration	Magnitude	Causes
Transients			
3.1 Impulsive	< 50 ns-1 ms		Lighting
3.2 Oscillatory	5 μs-50 ms	0-8 pu	Switching event, power electronic commutation, capacitor energization
Waveform distortion			
4.1 DC offset	Steadystate	0-1 %	Geomagnetic disturbance, effect of half-wave rectification
4.2 Harmonics	Steadystate	0-20 %	Nonlinear characteristics of devices and loads
4.3 Interharmonics	Steadystate	0-2 %	Effect of static frequency converters, induction furnaces, and arcing devices
4.4 Notching	Steadystate		Current commutation in three phase converters
4.5 Noise	Steadystate	0-1 %	Caused by power electronic devices, control circuits, arcing equipment
Imbalance			
5.1 Voltage	Steadystate	0.5-2%	Unbalanced single-phase loads, blown fuse on one phase of a three-phase bank, use of single-phase line regulators
5.2 Current	Steadystate	1-30%	
Voltage Fluctuations	Intermittent	0.1-7 %	Arc furnaces are the most common cause
Power frequency variations	<10 s	± 0.1 Hz	Faults on the bulk power transmission system, large block of load being disconnected, large source of generation going off line

The IEEE standard for power quality monitoring is IEEE-1159. The IEEE standard for harmonic control in electrical power systems is IEEE-519. According to IEEE-519 (2014), "in order to establish meaningful limits for harmonic emissions, it is necessary to consider the size of the end user, and the strength of the system. Harmonic limits shall be evaluated at the point of common coupling". The current distortion limits for general distribution systems, 120 V-69 kV are shown in table 1.2, where I_{SC} is the available fault current and I_{MD} is the maximum demand current. Voltage distortion limits are shown in table 1.3.

Table 1.2: Current distortion limits for general distribution systems, 120 V-69 kV

I_{SC}/I_{MD}	$3 \leq h < 11$ (%)	$11 \leq h < 17$ (%)	$17 \leq h < 23$ (%)	$23 \leq h < 35$ (%)	$35 \leq h \leq 50$ (%)	TDD (%)
<20	4.0	2.0	1.5	0.6	0.3	5.0
20-50	7.0	3.5	2.5	1.0	0.5	8.0
50-100	10.0	4.5	4.0	1.5	0.7	12.0
50-100	10.0	4.5	4.0	1.5	0.7	12.0
100-1000	12.0	5.5	5.0	2.0	1.0	15.0
≥1000	15.0	7.0	6.0	2.5	1.4	20.0

Table 1.3: Voltage distortion limits

Bus voltage at PCC	Individual harmonic magnitude (%)	Total voltage distortion (THD in %)
≤1.0kV	5.0	8.0
≤69kV	3.0	5.0
69.001-161kV	1.5	2.5
>161kV	1.0	1.5

1.2.5 Mitigation of power quality problems

Although passive filters can mitigate most of the power quality issues, the main disadvantage of them is the bulky nature of inductors and capacitors used in them. Moreover, the resonance experienced due to the interaction with line reactance and lack of dynamic response, demands for active filtering solutions. Mainly, active filters are of three types; shunt active filter, series active filter, and hybrid active filter. The shunt active filter mitigates the current related power quality problems, whereas the series

active filter solves the voltage related issues. The hybrid active filter is a combination of passive and active filters, which are having qualities of both active and passive filters (Halpin and Card, 2011).

1.2.6 Shunt active power filter interfacing renewable energy system to the grid

The shunt active power filter mitigate current harmonics by injecting compensating current. It operates as a current source, which injects the harmonic components of the load current phase shifted by 180^0. As a result, components of harmonic currents contained in the load current are cancelled by the effect of SHAF, and the source current remains sinusoidal and in phase with the respective phase-to-neutral voltage (Morain and Dixon, 2011). The SHAF can also be used for interfacing hybrid renewable system to the grid, by incorporating the additional functionality of grid interfacing inverter to it. The control system of the SHAF interfacing renewable system consists of a DC-link voltage control loop, a current harmonic mitigation loop and a current tracking controller for inverter pulse generation.

1.2.6.1 DC link voltage regulation

The effective exchange of active power from the renewable system to the grid is done by controlling the DC-link voltage of the system. Due to the intermittent nature of renewable sources, the active power generated is highly dynamic. The variations in load also create dynamic power variations in the system. The wide variations in DC capacitor energy cause stability related issues. The linear DC-link voltage controllers such as Proportional-Integral (PI), can be tuned for a certain steady-state range to have stable operating condition (Mikkili and Padamati, 2017). However, the stability for a whole wide range of dynamic conditions cannot be assured by them. Therefore, fast, non-linear and robust control of DC-link voltage is necessary for modern SHAF (Devassy and Singh, 2018; Liang, 2017; Samir et al., 2018). Hence, the robust controllers for DC-link voltage control of SHAF have been studied.

A modified PI controller with particle swarm optimization is reported in the liter-

ature, in which the gains of the PI controller are controlled by PSO algorithm (Demirdelen et al., 2016). A self-charging algorithm with PI controller is introduced by Zainuri et al. (2016) for improving the performance of DC-link voltage controller in SHAF. Even though the response time and overshoot are improved by these methods, the stability of the system for wide dynamic range is not discussed. Moreover, a slight error in the results from the PSO algorithm may result in a wrong selection of gain values for PI, which may lead to instability. The DC-link voltage regulation using a Fuzzy controller is reported in (Mikkili and Panda, 2011). Even though superior dynamic performance in balanced, unbalanced and distorted grid conditions is claimed, the performance of the Fuzzy controller in the presence of renewable energy sources is not discussed. The DC-link voltage of SHAF using Sliding Mode Control is proposed by Asadi et al. (2016). The hybrid combination of PI with Sliding Mode Controller (SMC) is also reported in literature (Ribeiro et al., 2015; Salimi et al., 2017). The control gains of PI controller are determined using SMC in (Ribeiro et al., 2015), whereas Salimi et al. (2017) proposed a combination of SMC in parallel with PI. However, the inbuilt chattering problem and poor steady-state performance of SMC are not addressed completely. The design of a Back Stepping Controller (BSC) for a grid-side converter of a wind power energy system is discussed by Wang et al. (2013). A BSC for DC-link voltage control of SHAF is also reported in the recent literature (Ghamri et al., 2015; Mahfouz et al., 2015). A faster response time compared to PI controller is claimed in (Ghamri et al., 2015; Mahfouz et al., 2015; Wang et al., 2013). However, the switching losses and the capacitor leakage losses are not considered in the design of the DC-link voltage controller. Moreover, the stability aspects of the system have not been discussed.

1.2.6.2 Current harmonic mitigation

The harmonic current compensation of local loads is also an important goal for the SHAF. Among the existing methods for current harmonic mitigation such as Discrete Fourier Transform (DFT) method, recursive DFT method, Fast Fourier Transform (FFT) method, Artificial Neural Network (ANN) method etc. (Bagheri et al., 2016; Chen et al., 2017; Lada et al., 2016; Mishra et al., 2017; Patel et al., 2017; Raheni and Thiru-

moorthi, 2017; Wang and Li, 2013), the Synchronous Reference Frame (SRF) method and instantaneous active and reactive power (pq) method are predominantly used (Akagi, 2005; Mikkili and Panda, 2011; Morain and Dixon, 2011). The advantage of pq method over SRF method is that the Phase Locked Loops (PLL) are not required in pq method, which reduces the overall complexity. However, conventional pq theory offers poor performance in non-ideal grid voltage conditions.

In pq method, Low Pass Filters (LPF) are widely used for extracting fundamental component of load currents. The main drawback of LPF is the inbuilt phase delays. The performance of the LPF improves with the increase in order. However, the order of the filter is often limited by the size of processors and control complexity. The limitations of LPF can be overcome by using Self-Tuning Filters (STF) (Benchouia et al., 2015; Hoon et al., 2017; Nejabatkhah et al., 2016).

1.2.6.3 *Current control for pulse generation*

Several current tracking controllers for inverter control are reported in the literature. The linear controllers reported so far in literature are Proportional Integral (PI) controller, Proportional Resonant controller, Repetitive Controller etc. The limitation of the PI method is the presence of high-frequency sub-harmonic oscillations (Hajizadeh and Golkar, 2007). The Proportional Resonant controller is another linear current controller, which offers high gain around natural resonant frequency and thereby eliminates the steady-state error between the reference and the controlled signal (Escobar et al., 2009). Another linear current controller is the Repetitive Controller, in which the steady state error is reduced by periodic control. It offers large gain at integral multiples of fundamental frequency. Different types of repetitive controllers are sliding mode repetitive controllers, odd harmonic repetitive controllers, and dual mode repetitive controllers. The slow dynamic response is the main limitation of the repetitive controller (Wei et al., 2013).

The commonly used non-linear current control methods are predictive control, dead-beat control, and hysteresis control. Predictive controller predicts the behaviour of

variables in each switching states using the mathematical model of the power converter. The main limitation of this method is the large control loop time period (Wu and Guo, 2008). In the dead-beat controller, the control algorithm calculates the phase voltage to make the phase current reach its reference by the end of the following modulation period. It is faster and simpler compared to predictive method (Xiaojie and Yongdong, 2002). Hysteresis current controller is another nonlinear current controller. It controls the switches in an inverter asynchronously to ramp the current through an inductor up and down so that it follows a reference. Among all the techniques discussed, hysteresis current control method is the most commonly used technique due to its simplicity and quick dynamic response (Vahedi et al., 2011).

1.2.7   Series Active Filter

The series active filter protects the consumer loads from inadequate supply voltage quality. It acts as a voltage regulator and a harmonic isolator between the utility system and the load. Series active filter was first introduced by Peng et al. (1990). Based on the topology, series active filters can be classified into two; Topology with no energy storage, and topology with energy storage. Comparison of different topologies of series active filters are presented in (Nielsen and Blaabjerg, 2005). In the topology with no energy storage, energy is taken from the main supply through a shunt converter. During voltage sags, the series active filter use the available source supply and injects the compensating voltage. The main drawback of this topology is that it takes more current from the line during sags and the upstream loads will see a higher voltage drop. On the other hand, it saves the cost of energy storage system (Woodley et al., 2000). In the topology with energy storage, battery energy storage system is present, which acts as a supply for the series active filter. In this topology, current flow from the grid remains unchanged during sags. Storing electrical energy is expensive, but for weak grids, this topology is recommended for improved performance(Nielsen and Blaabjerg, 2005).

The control methods commonly used for series active filters are mainly of two types; feedforward, and feedback methods. In feedforward control, by measuring the

grid voltage, the required compensation voltage is calculated and using a voltage controller, the inverter generates and injects the required compensation voltage into the system (Joos, 1999). It is a simple and robust way of controlling series active filter. In feedback controllers, the compensating voltages or load voltages are measured and used in a feedback loop. The controller tries to keep the error between the measured voltage and the calculated voltage as low as possible. Even though the tuning of voltage controllers is complex and it depends on the system parameters, they give more accurate response compared to feed forward controllers (Nielsen, 2002). The feedback controller performance depends on the type of voltage disturbance (sag/swell/distortion) detection algorithm and the voltage controller used.

Different voltage disturbance detection algorithms reported in the literature are Phase Locked Loop (PLL) method, Peak Value Detection method, Wavelet Transform method, Fourier Transform method, and Root Mean Square method. In the PLL method, the phase jumps in each phase of grid voltage are detected. The information regarding sag/swell depths are missing, and it can only be used for certain applications (Fitzer et al., 2002). The peak detection method is the simplest method to detect voltage disturbance. In this method, the peak value of the grid voltage is detected by finding the point at which the gradient of voltage is zero. The instantaneous value at peak value is compared with a reference value. The limitations are the lack of phase shift information and the possibility of noise affecting the gradient function (Ramachandaramurthy et al., 2004). In the wavelet transform method, a wavelet prototype function needs to be selected for each application, which reduces the flexibility of the controller for different applications (Saleh et al., 2008). Even though the Fourier Transform method gives exact information about the magnitude and phase information of each of the frequency components, it takes one complete cycle to provide the information (El-Gammal et al., 2011). In root mean square method, the grid voltage is sensed, and the Root Mean Square (RMS) value is calculated using abc to dq transformation. Both disturbance magnitude and phase information are available in this method. Moreover, it is relatively easier to implement in real-time control. The limitation of this method is that the low pass filters associated with it for detecting the harmonic components of grid

voltage add extra phase delays, which may deteriorate the compensation performance (Ali et al., 2013). Once the disturbances are detected, the reference voltage is generated for the compensation, and the inverter is controlled using a voltage controller.

Different voltage control methods reported in the literature are PI control, state variable control, Sliding Mode Control and Fuzzy control. In the PI controller based voltage controller, the detailed modelling of the entire system is necessary for effective control. Moreover, it does not guarantee a stable operation under a large supply or load variation (Joos et al., 2004; Ma et al., 2010). The state variable control offers a faster voltage compensation. However, detailed mathematical modelling of the system is required in this method also (Ezoji et al., 2012; Ruilin and Yuegen, 2005). The stability of the system is assured by Sliding Mode Controller. However, the chattering phenomena and considerable steady state error are the limitations. The Fuzzy controller design is comparatively simpler, and the controller is adaptive to system changes. Moreover, the tracking error and transient overshoots can be considerably reduced using the Fuzzy controller (Rajasekaran et al., 2011).

1.2.8   Unified Shunt-series active filter (UPQC) interfacing renewable energy system to the grid

The shunt and series active filters can be combined(UPQC) to achieve good control over several power quality problems simultaneously (Khadkikar, 2012). In UPQC, the shunt and series filters are connected back to back with a common DC-link (Fujita and Akagi, 1998). The UPQC mitigates both voltage and current related power quality issues. UPQCs are classified based on the topology, supply system, and system configuration. The following section deals with a review on UPQC classification.

Based on the converter topology used, UPQCs are of two types; current source inverter based, and voltage source inverter based. In current source inverter based UPQC, two current source inverters are connected back to back with a common DC-link with a series inductor (Melin et al., 2010). This topology is not popular because of the high cost and higher losses. The latter topology is using two voltage source inverters con-

nected back to back with a common DC-link and a shunt connected capacitor. This topology is highly popular because of its inherent flexibility on control, minor losses, and cheaper cost (Khadkikar and Chandra, 2011), (Kesler and Ozdemir, 2010).

Based on the supply system, UPQC can be classified as single phase and three phase UPQCs. This review is concentrated on three phase UPQCs; they are of two types; three wire and four wire type. Three phase- four wire type UPQCs are required in distribution level, as it contains a neutral conductor. Four wire UPQCs are mainly of three types; Split capacitor type, three H-bridge type, and four leg type. In split capacitor type, two capacitors are connected in series at the DC-link, and the midpoint is maintained at zero. The midpoint of the capacitor is connected to the neutral conductor. An additional control loop is needed to maintain the midpoint voltage as zero (Zhili and Dongjiao, 2010). In three H-bridge inverter type, three units of single phase H bridges are used. This topology reduces the voltage requirement by a factor of 1.732. However, this topology has a higher number of semiconductor switches, higher losses and higher cost compared to split capacitor topology (Khadkikar et al., 2011). In four leg topology, a dedicated inverter leg is present for neutral current control, which offers better neutral current control compared to other topologies (Khadkikar and Chandra, 2009).

UPQCs can be classified into several types based on the system configuration.

- Left shunt UPQC: The placement of the shunt filter is left of the series filter. It is used in special cases to avoid interference of passive filters with shunt active filters (Chen and Joos, 2001).
- Right shunt UPQC: The placement of the shunt filter is right to the series filter. This is most commonly used. In this topology, the interfacing transformer has sinusoidal current through it, irrespective of the nature of load current. The overall performance of UPQC is better in this configuration (Chen et al., 2000).
- Interline UPQC: The shunt active filter is connected to one feeder, and the series active filter is connected to an adjacent feeder. This is used in special cases where the current harmonic problems in the first feeder and the voltage harmonics problems in the second feeder can be mitigated simultaneously (Jindal et al.,

2007).

- Multi-converter UPQC: A third converter is connected to control and support the DC-link. This eliminates the additional DC-link voltage control loop in the shunt controller, but an additional converter increases the overall cost (Li et al., 2006).

- Multilevel UPQC: The three leg or four leg inverters are replaced by multi-level inverters. The complexity of the system increases as the number of switches increases, however, this offers better performance in high power configurations (Rubilar et al., 2007).

- UPQC-DG: Distributed generators can be connected at DC bus of three-phase, four leg UPQC. In addition to the voltage and current compensation, DG power flow can also be managed by UPQC using this configuration (Davari et al., 2009; Han et al., 2006; Park et al., 2003; Toodeji et al., 2009).

The UPQC-DG configuration can be further extended to connect the wind-solar hybrid system at the DC bus to exchange the generated real power to the grid. The controller for UPQC is the combination of SHAF and SAPF control methods, which are discussed in 1.2.6 and 1.2.7 respectively.

1.3 OBJECTIVES OF THE RESEARCH WORK

The following objectives are formulated based on the research gaps identified from the literature review.

1. Simulation and analysis of a three-phase, four leg shunt active power filter interfacing hybrid wind-solar system to the distribution grid.
2. Implementation of robust DC-link voltage control techniques and advanced harmonic current mitigation techniques for improving the performance of the shunt active power filter interfacing hybrid wind-solar system to the distribution grid.
3. Design, simulation, and analysis of a series active filter at the distribution level.
4. Design, simulation and analysis of a unified shunt-series active power filter interfacing hybrid wind-solar system to the distribution grid.
5. Laboratory scale hardware implementation of a single-phase shunt active power

filter and experimental verification of the proposed DC-link voltage control technique and harmonic current mitigation technique.

1.4 LAYOUT OF THE REPORT

The thesis has been organized as follows.

- Chapter. 2 deals with the design and modelling of the wind-solar hybrid system and grid interfacing inverter.

- Chapter. 3 deals with the design, simulation, and analysis of the control system for a three-phase shunt active filter, interfacing wind-solar hybrid system to the distribution grid. The simulation results for different steady-state and dynamic conditions are also presented and tabulated in this chapter.

- Chapter. 4 presents the control system design, simulation, and analysis of simulation results of UPQC interfacing wind-solar hybrid system to the distribution grid.

- Chapter. 5 discusses the hardware implementation of the laboratory prototype of single-phase SHAF. The FPGA implementation of the control algorithm and the details of sensing and signal conditioning circuits are also included in this chapter. The study and analysis of the hardware results are also presented.

- The conclusions and recommendations for future work are presented in Chapter 6.

Chapter 2

Design and Modelling of Wind-Solar Hybrid System and Grid Interfacing Inverter

2.1 INTRODUCTION

Commonly available renewable energy sources are wind, solar, tidal, micro-hydro and geothermal. Wind and solar are the most common renewable sources used for power generation. As wind and solar are abundant, and up to an extent complementary to each other in availability, a hybrid combination of them is preferred. In this study, A 15 kWp horizontal axis wind turbine coupled with PMSG is considered. The main advantage of PMSG based wind energy system is that the gearbox can be eliminated and thus overall weight and cost can be reduced, improving performance and efficiency of the system. The series-parallel combination of solar PV modules with overall rating 15 kWp is considered in this study. The DC-shunted scheme is considered for the grid interconnection of the wind-solar hybrid system, through a common DC-link and a DC-AC power converter. The schematic diagram of the overall system is shown in Figure 2.1, which consists of a wind energy system, solar energy system, DC-DC boost converters, DC-link capacitor, DC-AC power converter, AC filter and non-linear loads.

This chapter deals with the design and modelling of power circuit components of the system.
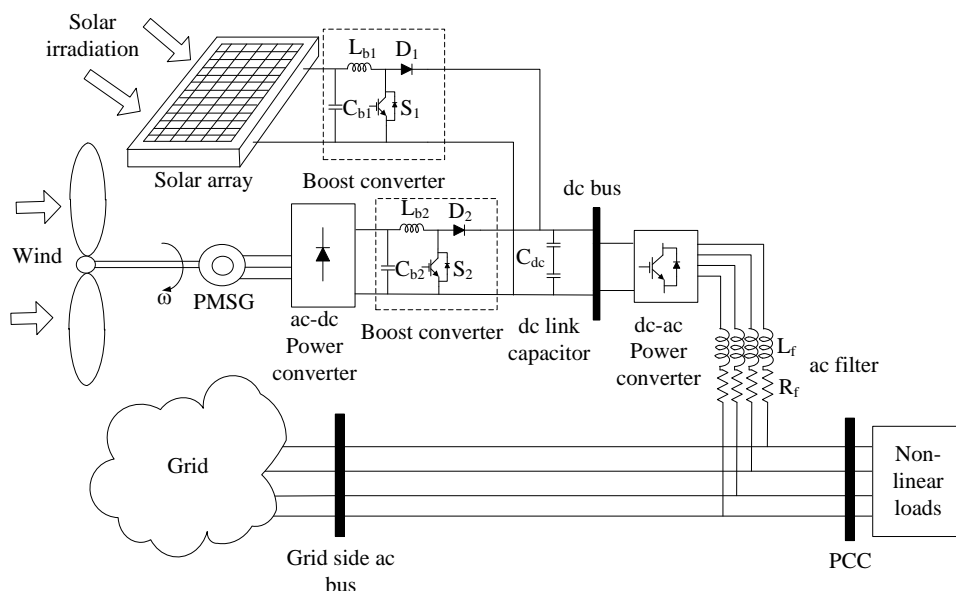
Figure 2.1: Schematic diagram of a DC shunted grid-connected renewable energy system with non-linear load at load centre

2.2 MODELLING OF WIND ENERGY SYSTEM

Wind Energy System consists of a variable wind speed turbine based on a multipole PMSG. The turbine rotor shaft is directly coupled with PMSG, without any gearbox. The generator output is converted to DC using an AC-DC power converter. A DC-DC boost converter is cascaded with the power converter. The output of the DC-DC converter is connected to a common DC bus. Design and modelling of each component of wind energy system are described in following subsections.

2.2.1 Modelling of Wind Turbine

The power output of a wind turbine can be expressed as shown in (2.1), and the aerodynamic torque is given by (2.2), where, "P_W = wind turbine power (W), η = efficiency of turbine, ρ = air density (kg/m^3), C_P = power coefficient, A = rotor area (m^2), v_w = velocity of wind (m/s), ω_w = turbine rotor speed (rad/s)" (Anderson and

20

Bose, 1983).

$$P_w = \frac{1}{2}\rho A v_w^3 C_P \eta \tag{2.1}$$

$$T_w = \frac{P_w}{\omega_w} \tag{2.2}$$

The power co-efficient C_P is a function of tip speed ratio (λ) and blade pitch angle (β), which is defined as (2.3), where, "R = radius of rotor (m), v = pitch angle (angle between plane of rotation and blade cross section in degrees), max value of C_P = 0.593 (Betzs limit), $C_1 = 0.5, C_2 = 116, C_3 = 0.4, C_4 = 0, C_5 = 5, C_6 = -21$" (Wang et al., 2013).

$$C_P(\lambda, \beta) = C_1 \left[\left(C_2 \frac{1}{\beta} - C_3 v - C_4 v^x - C_5 \right) \times exp \left(C_6 \frac{1}{\beta} \right) \right] + 0.0068\lambda \tag{2.3}$$

Tip speed ratio λ and β are calculated as shown in (2.4) and (2.5) respectively.

$$\lambda = \frac{\omega_w R}{v_w} \tag{2.4}$$

$$\frac{1}{\beta} = \frac{1}{\lambda + 0.08v} - \frac{0.035}{1 + v^3} \tag{2.5}$$

The turbine characteristics, the variation of C_P with λ for various pitch angles is shown in Figure 2.2. The value of C_P for a particular pitch angle is maximum at certain values
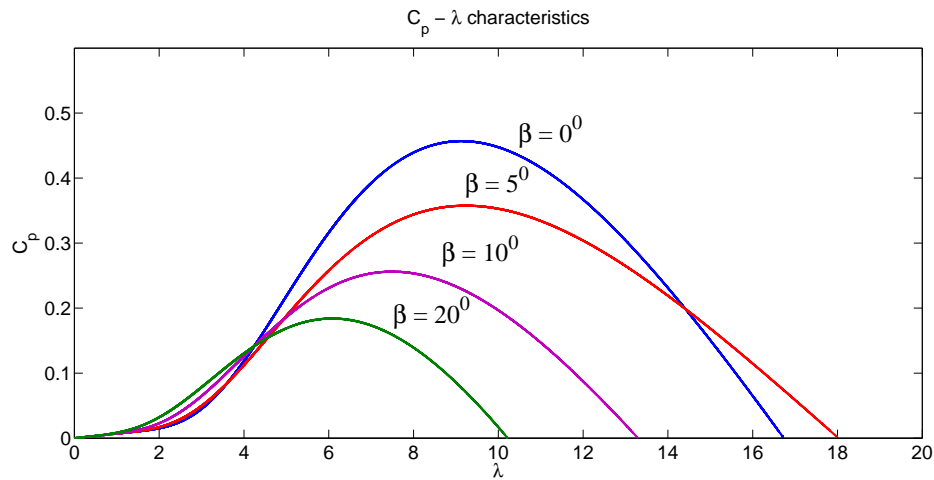
Figure 2.2: C_P vs λ Characteristics

of λ. The global maxima of C_P is observed as 0.44.

21

2.2.2 Modelling of PMSG

The mathematical model of PMSG in synchronous reference frame is given by 2.6 and 2.7, where, "R_{st} = stator resistance(Ω), L_d, L_q = inductance (H) of generator on d and q axis, Ψ_f = permanent magnet flux (Wb), ω_e = electrical rotating speed (rad/s), p = number of pole pairs of generator, u_d, u_q = d and q axis voltages, i_d, i_q = d and q axis currents".

$$\frac{di_d}{dt} = \frac{1}{L_d}[-R_{st}i_d + w_e L_q i_q + u_d] \tag{2.6}$$

$$\frac{di_q}{dt} = \frac{1}{L_q}[-R_{st}i_q - w_e(L_d i_d + \Psi_f) + u_q] \tag{2.7}$$

The electromagnetic torque of PMSG is given by (2.8).

$$T_e = 1.5p[(L_d - L_q)i_d i_q + i_q \Psi_f] \tag{2.8}$$

Wind power vs rotor speed curves for different wind speeds are shown in Figure 2.3. The power generation decreases as the wind speed decreases. The power for a particular
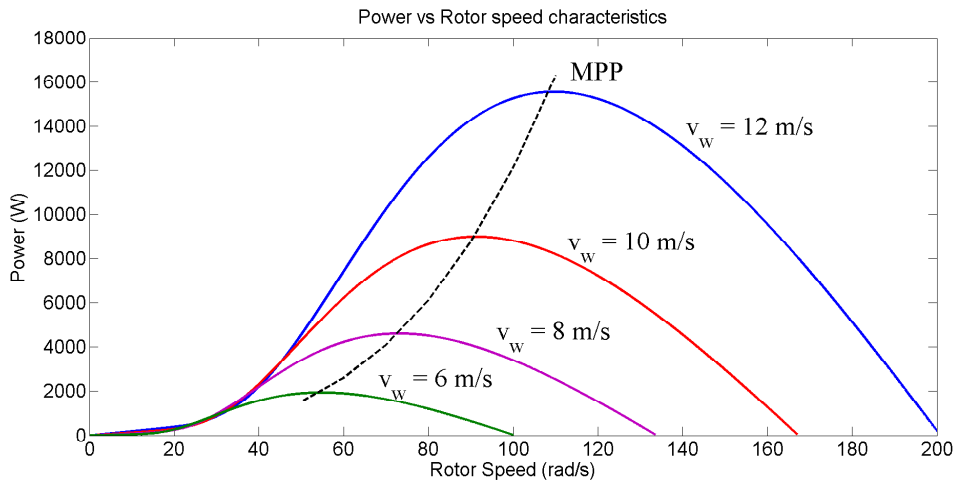
Figure 2.3: Wind power vs Rotor speed characteristics

wind speed is maximum at a certain value of rotor speed. In order to extract maximum available power, the turbine should be operated at optimum rotor speed.

22

2.3 MODELLING OF SOLAR ENERGY SYSTEM

Solar energy system contains solar PV arrays, which contain series and parallel PV modules. Mathematical modelling of solar energy system is explained in the following session.

2.3.1 Modelling of solar PV cell

The basic equations of a photovoltaic cell are given by (2.9), (2.10) and (2.11), where, "$V_t = kT/q_e$, I_{PV} = photovoltaic current, I_0 = saturation current, V_t = thermal voltage of the cell, k = Boltzmann constant, T = temperature in K, q_e = charge of electron, $I_{PV,n}$ = photovoltaic current in normal condition (25^0C, 1000 W/m^2), ΔT = $T - T_n$ in K, G = irradiation in W/m^2, G_n = nominal irradiation in W/m^2, K_I = temperature coefficient of current (A/K), K_V = Temperature coefficient of voltage (V/K), $I_{sc,n}$ = short circuit current nominal, $V_{oc,n}$ = open circuit voltage nominal, a = diode constant ($1 \leq a \leq 1.5$)" (Gow and Manning, 1996). Figure 2.4 shows the circuit diagram of a solar PV cell.

$$I = I_{PV} - I_0 \times exp\left(\frac{V + IR_s}{V_t a}\right) - \left(\frac{V + IR_s}{R_p}\right) \tag{2.9}$$
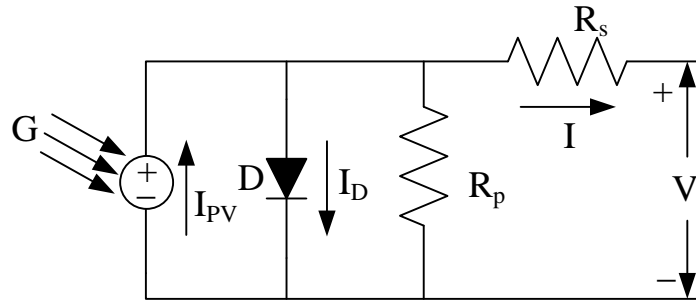
Figure 2.4: Basic Solar PV Cell

$$I_{PV} = (I_{PV,n} + K_I \Delta T)\frac{G}{G_n} \tag{2.10}$$

$$I_0 = \frac{I_{sc,n} + K_I \Delta T}{exp\left(\frac{V_{oc,n} + K_V \Delta T}{aV_t}\right) - 1} \tag{2.11}$$

23

The solar PV modules consists of several solar cells in series. The solar arrays are formed with the series-parallel combination of solar PV modules. The modelling of solar arrays are described in following subsection.

2.3.2 Modeling of Solar PV Array

The equivalent circuit of a solar PV array is shown in Figure 2.5 . Equation (2.12) represents the mathematical model of a solar array, where N_p = Number of parallel PV modules and N_s = Number of series PV modules (Tan et al., 2010; Villalva et al., 2009).
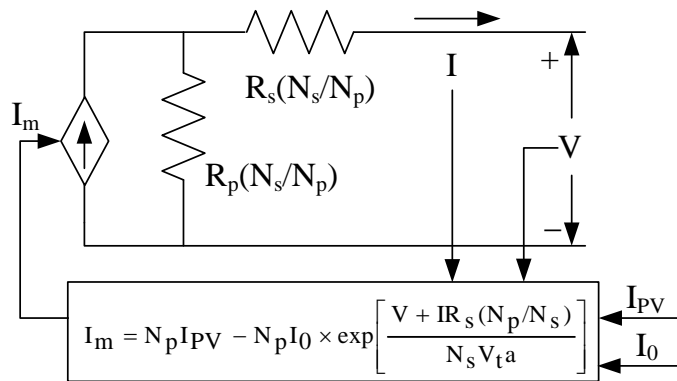
Figure 2.5: Solar PV array equivalent circuit

$$I_m = N_P I_{PV} - N_P I_0 \times exp\left[\frac{V + IR_s(N_s/N_p)}{N_s V_t a} - 1\right] - \left[\frac{V + IR_s(N_s/N_p)}{R_P(N_s/N_p)}\right] \quad (2.12)$$

The P-V characteristics at various irradiation levels with constant temperature are shown in Figure 2.6. As the irradiation level increases, the incident energy on the PV cells increases. The peak power generation from solar array increases with increase in irradiation level. The voltage at which maximum power generated also varies with change in irradiation level.
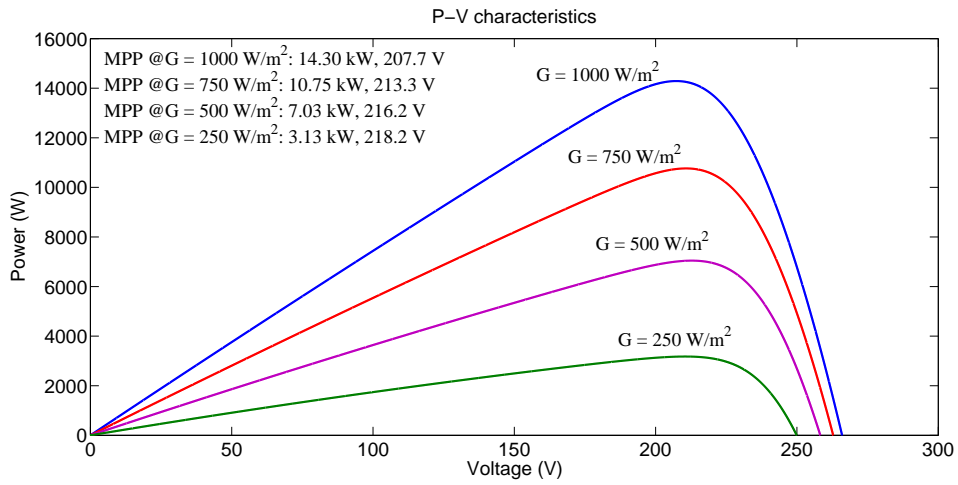
Figure 2.6: P-V characteristics of solar array for different solar irradiations at 25^0C
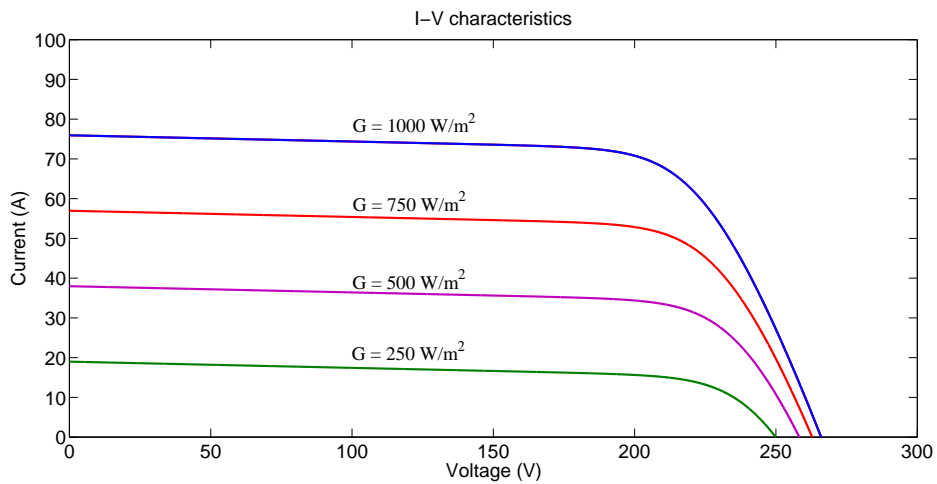
Figure 2.7: I-V characteristics of solar array for different solar irradiations at 25^0C

The I-V characteristics at various irradiation levels with constant temperature are shown in Figure 2.7. The PV array acts like a constant current source for a certain range of voltage values. The current as well as power abruptly reduces to zero with increase in the voltage beyond a certain value.

The P-V and I-V characteristics at various temperatures with constant irradiation level are shown in Figure 2.8 and 2.9.

25
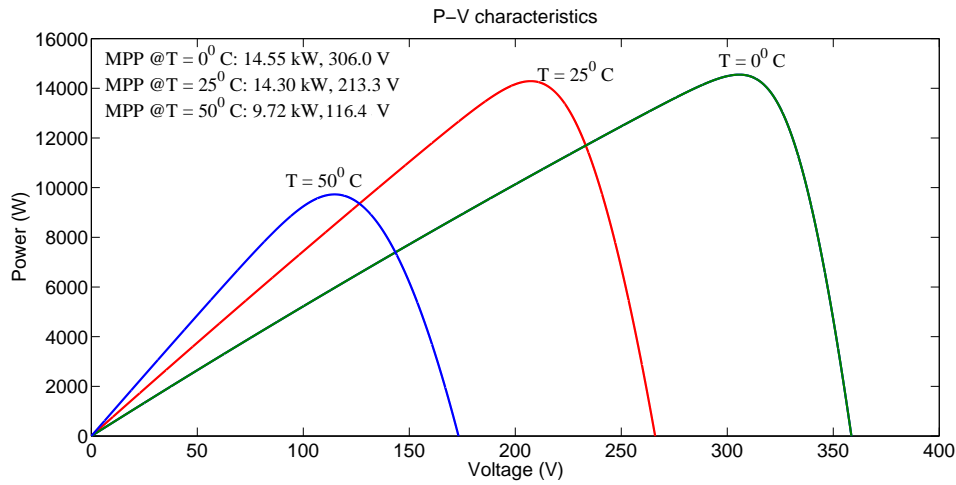
Figure 2.8: P-V characteristics of solar array for different temperature levels at 1000 W/m^2
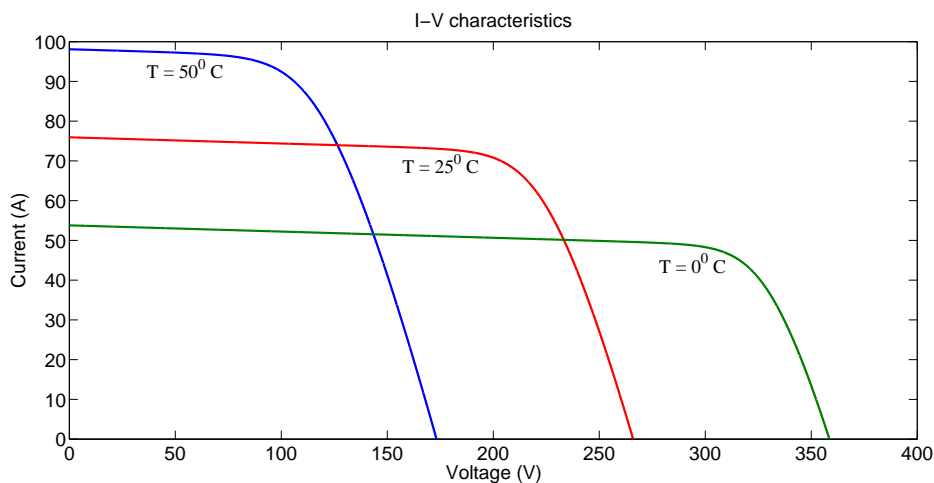
Figure 2.9: I-V characteristics of solar array for different temperature levels at 1000 W/m^2

As the ambient temperature increases, the semiconducting property of PV cells weakens. The peak power decreases with increase in ambient temperature. The voltage at which maximum power is generated also decreases with increase in temperature.

2.4   BOOST CONVERTER DESIGN

The wind and solar energy systems generate varying DC output. In order to connect them to a common DC-link, the variable DC voltage should be converted to constant DC using DC-DC boost converters. The maximum power point tracking (MPPT)

of solar energy system for varying irradiation is done by adaptively changing the duty ratio of boost converter and thereby setting the optimal operating voltage at the PV terminal. In wind energy system, the optimal rotor speed of PMSG for varying wind speed is set by changing the duty ratio of boost converter connected with it. The circuit diagram of boost converter is shown in Figure 2.10.
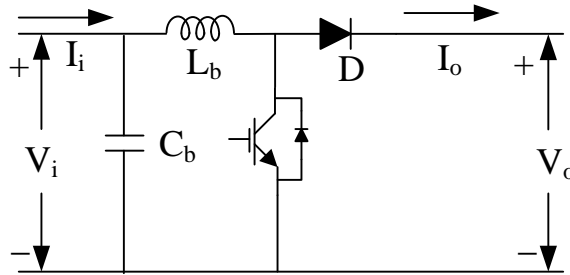
Figure 2.10: Circuit diagram of DC-DC boost converter

The design equations for boost converter are shown in (2.13) and (2.14), where V_i and I_i are the voltage and current from the renewable source respectively, ΔI_i is the input current ripple of boost converter, V_o and I_o are the output voltage and current of boost converter respectively, d is the duty ratio of boost converter switch and f_s is the switching frequency (Czarkowski, 2011; Krithiga and Ammasai Gounden, 2014; Malla et al., 2016).

$$L_b = \frac{V_i d}{2\Delta I_i f_s} \tag{2.13}$$

$$C_b = \frac{I_o d^2}{(\Delta V_o/V_o)(1-d)V_o f_s} \tag{2.14}$$

The maximum power from wind and solar system are tracked by adaptively changing the duty ratio of boost converter switch. The incremental conductance with integral regulator method is used for maximum power point tracking (MPPT), in the wind as well as in solar energy systems. The flowchart, shown in Figure 2.11 explains the incremental conductance method of MPPT (Boehringer, 1968; Wasynczuk, 1983).

The wind-solar hybrid renewable system is interfaced to the grid using voltage

27
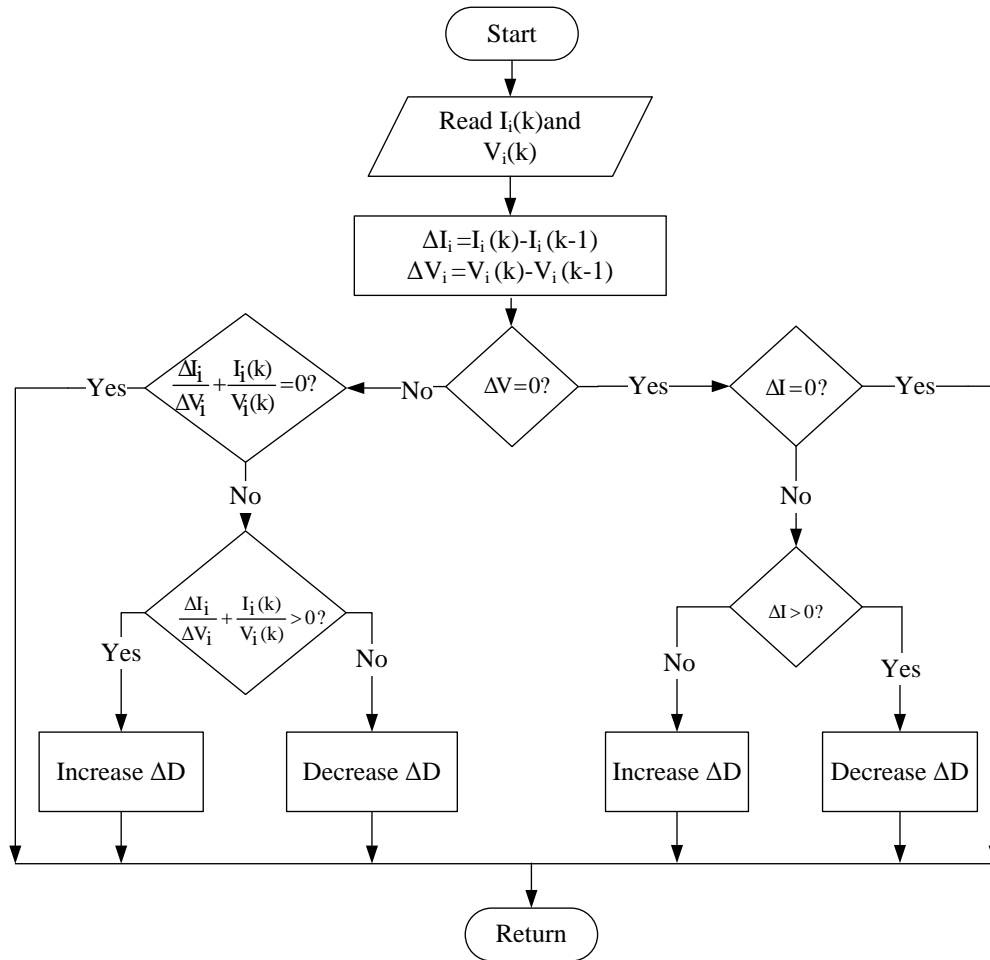
Figure 2.11: Flowchart of Incremental Conductance Method

source inverter. The design of VSI is discussed in the following section.

2.5 DESIGN OF VSI

The design of power circuit of VSI involves selection of four major parameters; DC-link voltage (V_{dc}), the DC-link capacitor (C_{dc}), filter inductor (L_f) and switching device.

2.5.1 Selection of V_{dc}

The value of DC-link voltage in SHAF is always selected greater than the peak value of grid voltage for the effective real power transfer from DC-link to load. How-

ever, with the increase in DC-link voltage, the switching losses in the inverter also increases. The maximum DC-link voltage V_{dcmax} is given by (2.15), where V_s is the line-line RMS value of grid voltage (Biricik et al., 2016). The value of DC-link voltage is selected using the inequality shown in (2.16).

$$V_{dcmax} = 1.5 \times \sqrt{2}V_s \tag{2.15}$$

$$\left(\sqrt{2}V_s\right) < V_{dc} < \left(1.5 \times \sqrt{2}V_s\right) \tag{2.16}$$

2.5.2 Selection of C_{dc}

DC link capacitors are used for reducing DC ripple. They also store energy during transients. The value of the DC-link capacitor is selected using (2.17), where, S is the capacity of the inverter, ω is the system frequency, V_{dc} is the DC-link voltage and ΔV_{dc} is the peak to peak DC-link voltage ripple (Karuppanan, 2012).

$$C_{dc} \geq \frac{S}{2\omega V_{dc}\Delta V_{dc}} \tag{2.17}$$

2.5.3 Selection of L_f

The inductive filter is used for removing switching frequency components from the inverter current. The filter inductance can be calculated using (2.18), where, h is the hysteresis band, f_{max} is the maximum switching frequency, and V_{dc} is the DC-link voltage. Hysteresis band is usually taken as 5 % of compensation current (Karuppanan, 2012).

$$L_f = \frac{V_{dc}}{6hf_{max}} \tag{2.18}$$

2.5.4 Switching device selection

Switching device selection depends on "maximum current flow through the device, maximum voltage stress on the device during the off period and switching frequency" (Karuppanan, 2012).

Maximum current flow: Maximum current flows through the switch when it is closed, and the other switch in the same leg is open. The maximum current through the switch is line current of the three-phase system. Maximum current is the same for all the switching devices in the inverter.

Maximum voltage stress on the device during the off period: When one switch is open, and the other one is closed in the same leg, the open switch blocks the maximum voltage which is V_{dc}. Generally, the blocking voltage is chosen slightly higher than V_{dc} to avoid device failure.

Switching frequency: Usually switching frequency is selected ten times the largest harmonic frequency to be compensated. However, with the increase in switching frequency, the switching losses also increase.

2.6 CONCLUSION

Summarising this chapter, the modelling of the wind energy system and solar energy system have been discussed. The design of boost converter for both wind and solar energy systems have also been discussed. The SHAF design has been explained, which includes switching device selection, DC-link capacitor design and filter inverter design. Next chapter deals with the control system design and simulation results of a three-phase VSI interfacing wind-solar hybrid system to the distribution grid.

Chapter 3

Control System Design and Simulation of a Three-phase, Four-leg SHAF Interfacing Wind-Solar Hybrid System to the Distribution Grid

3.1 INTRODUCTION

In recent years, shunt active power filters (SHAF) have found many applications such as photovoltaic, wind power generation systems etc. In addition to harmonic compensation of local loads, SHAF is capable of active power exchange from renewable sources to the grid. The effective exchange of active power is done by controlling the DC-link voltage (Devassy and Singh, 2018; Liang, 2017; Samir et al., 2018). Due to the intermittency in renewable sources, the active power generated is highly dynamic. The variations in load also create dynamic power variations in the system. The wide variations in DC-capacitor energy cause stability related issues. The linear DC-link voltage controllers such as Proportional-Integral (PI), can be tuned for a certain steady-state range to have stable operating condition (Mikkili and Padamati, 2017). However, the stability for a whole wide range of dynamic conditions cannot be assured by them.

31

Therefore, fast, non-linear and robust control of DC-link voltage is necessary for modern SHAF. Hence, the robust controllers for DC-link voltage control of SHAF have been studied.

The harmonic current compensation of local loads is also an important goal for SHAF. The widely used control technique for harmonic current compensation is instantaneous power theory (Akagi et al., 2017). In this method, low pass filters (LPF) are widely used for extracting fundamental component of load currents. The main drawback of LPF is the inbuilt phase delays. The performance of LPF improves with the increase in order. However, the order of the filter is often limited due to the size of processors and control complexity. The limitations of LPF can be overcome by using self-tuning filters (STF) (Benchouia et al., 2015; Hoon et al., 2017; Nejabatkhah et al., 2016). Another limitation of conventional instantaneous power theory is its poor performance in non-ideal grid voltage conditions. This limitation is overcome in (Biricik et al., 2014) by using an additional self-tuning filter for detecting the fundamental component of the grid voltage.

This chapter deals with the design, simulation and analysis of a double loop controller for a three-phase shunt active filter, interfacing wind-solar hybrid system to the distribution grid. The outer DC-link voltage control loop is realized in three different ways, (i) using fast-acting PI, (ii) using the Fuzzy controller and (iii) using an adaptive BSC. An estimation rule is employed in BSC to estimate the switching loss in the voltage source inverter. The accurate quantification of leakage and switching losses enhances the loss compensation capability of the network by effectively controlling the active power flow to the capacitor. The proposed BSC is stable and robust for a wide dynamic range of operation. The inner harmonic mitigation loop consists of a dual-self-tuning filter (DSTF) based instantaneous power theory controller which enhances the performance of SHAF under non-ideal grid voltage conditions and load unbalances. Numerical simulations are performed in MATLAB/Simulink platform to check the effectiveness of the controller in active power exchange of renewable sources with the grid, and the shunt active filtering. The performance of the proposed compensation al-

gorithm: DSTF based pq algorithm is compared with the existing low pass filter based pq algorithm under different steady-state system conditions. The proposed Back Stepping algorithm based DC-link controller is compared with PI and Fuzzy controllers under several dynamic conditions. The results are analysed and summarized at the end of this chapter.

3.2 DESIGN AND IMPLEMENTATION OF CONTROL SYSTEM

The main objectives of the control system are (i) to maintain the DC-link voltage and balance the power flow, (ii) to compensate the harmonic components of load current at PCC. The general block diagram of the overall control system is shown in Figure 3.2.

3.2.1 PI-DSTF-pq Controller for SHAF

In PI-DSTF-pq controller, the inner loop is realized by pq theory with dual-STF and outer DC-link voltage loop is realized by PI controller. The block diagram of PI-DSTF-pq controller is shown in Figure 3.1. The design of current harmonic compensation loop and DC-link voltage loop are discussed in following subsections.
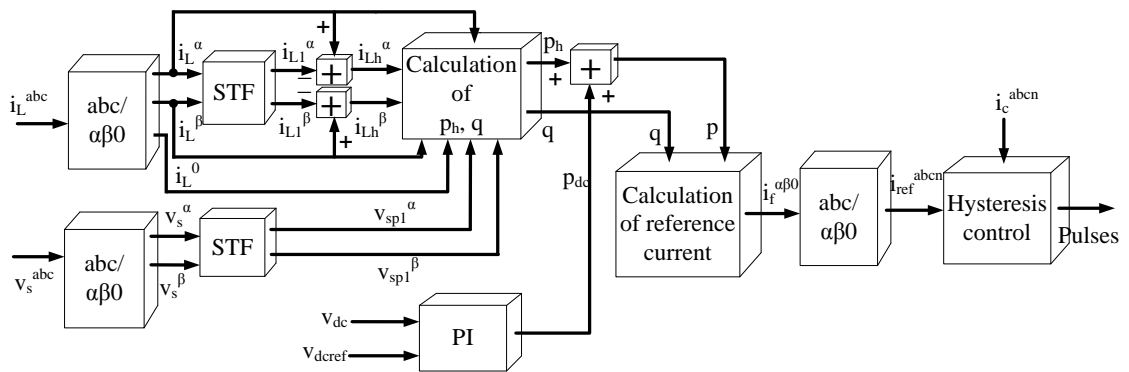
Figure 3.1: PI-DSTF-pq Controller

3.2.1.1 DC-link Voltage Control Loop

The DC-link voltage is sensed and the square of the sensed value is compared with the square of the DC-link reference value. The error signal is processed through PI controller.

33
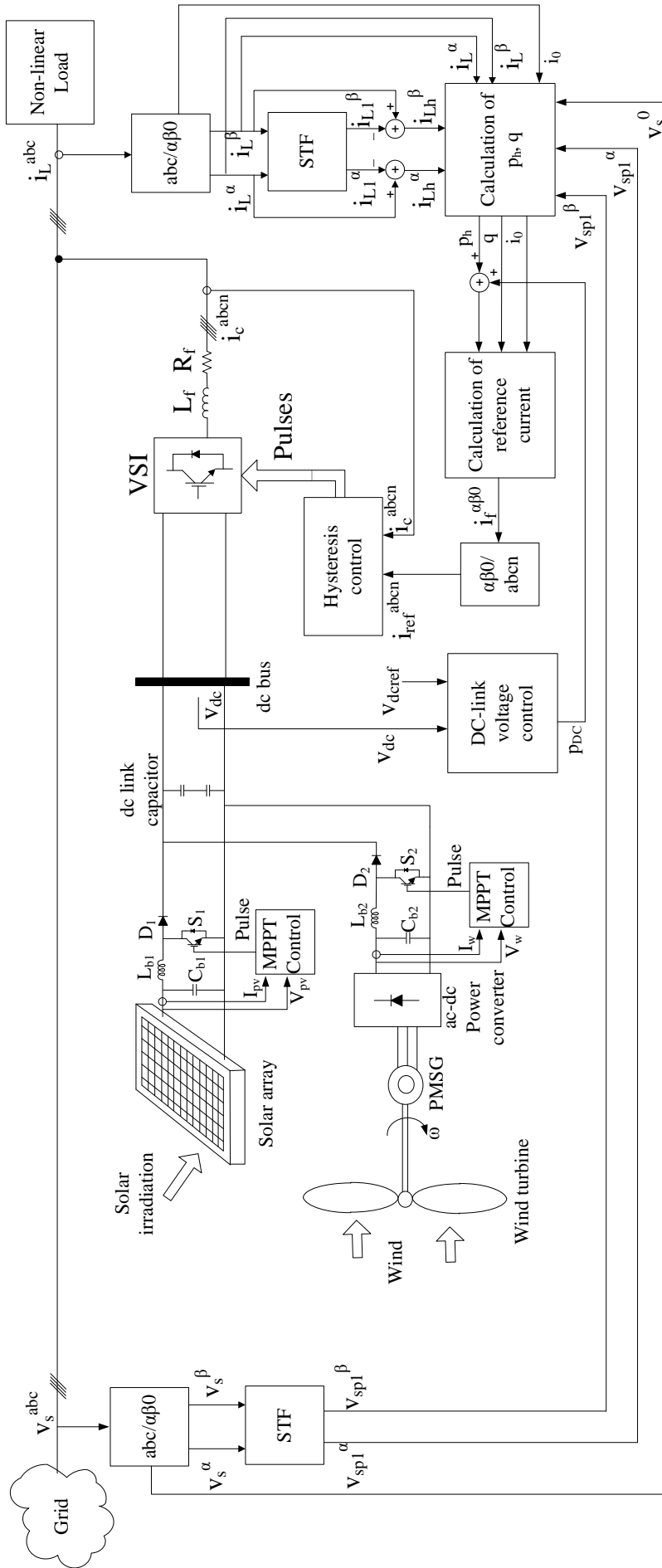
Figure 3.2: Overall Controller

34

The output of PI controller is considered as the amount of real power (P_{dc}) need to be injected from the network to the DC-link for maintaining the DC-link voltage as constant. The transfer function model of the DC-link voltage control loop as shown in (3.1) is considered for finding the k_p and k_i parameters of PI controller, where, ω_{nv} and ζ are natural frequency of undamped oscillations and damping constant of PI controller respectively.

$$\frac{V_{dc}^2(s)}{V_{dcref(s)}^2} = 2\zeta\omega_{nv}\frac{s + \dfrac{\omega_{nv}}{2\zeta}}{s^2 + 2\zeta\omega_{nv}s + \omega_{nv}^2} \tag{3.1}$$

Proportional and integral constants can be derived from the transfer function as (3.2). The values of k_p and k_i are selected by compromising between fast response time and small overshoot. The k_p and k_i values of PI controller are tuned by using Ziegler-Nicholas method.

$$k_p = 2\zeta\omega_{nv}C, k_i = \omega_{nv}^2 C \tag{3.2}$$

3.2.1.2   Design of Current Harmonic Compensation Loop

In the current harmonic compensation loop, the load currents and grid voltages are sensed and transformed to $\alpha\beta$ frame using (3.3) and (3.4). Where i_L^{abc} and v_s^{abc} are the three-phase load currents and grid voltages respectively. $i_L^{\alpha\beta 0}$ and $v_s^{\alpha\beta 0}$ are the load currents and grid voltages in $\alpha\beta 0$ frame.

$$\begin{bmatrix} i_L^\alpha \\ i_L^\beta \\ i_L^0 \end{bmatrix} = \sqrt{\frac{2}{3}} \begin{bmatrix} 1 & -\frac{1}{2} & -\frac{1}{2} \\ 0 & \frac{\sqrt{3}}{2} & -\frac{\sqrt{3}}{2} \\ \frac{1}{\sqrt{2}} & \frac{1}{\sqrt{2}} & \frac{1}{\sqrt{2}} \end{bmatrix} \begin{bmatrix} i_L^a \\ i_L^b \\ i_L^c \end{bmatrix} \tag{3.3}$$

$$\begin{bmatrix} v_s^\alpha \\ v_s^\beta \end{bmatrix} = \sqrt{\frac{2}{3}} \begin{bmatrix} 1 & -\frac{1}{2} & -\frac{1}{2} \\ 0 & \frac{\sqrt{3}}{2} & -\frac{\sqrt{3}}{2} \end{bmatrix} \begin{bmatrix} v_s^a \\ v_s^b \\ v_s^c \end{bmatrix} \tag{3.4}$$

The instantaneous real power needed for harmonic compensation, and instantaneous imaginary power needed for reactive power compensation are calculated using

(3.5) and (3.6), where i_{Lh}^{α} and i_{Lh}^{β} are the harmonic components of load currents and v_{sp1}^{α} and v_{sp1}^{β} are the fundamental components of grid voltage. The negative sign indicates that the power flow direction is from inverter to PCC.

$$p_h(t) = -(i_{Lh}^{\alpha} v_{sp1}^{\alpha} + i_{Lh}^{\beta} v_{sp1}^{\beta}) \tag{3.5}$$

$$q(t) = -(i_L^{\beta} v_s^{\alpha} - i_L^{\alpha} v_s^{\beta}) \tag{3.6}$$

The harmonic components of load current are extracted by subtracting fundamental component from the load current. The low pass filters are widely used for extracting fundamental components of load current. The main limitation of LPF is the inherit phase lag introduced by them. Moreover, the lower order harmonic components are not completely filtered out using LPF. The limitations of LPF is overcome using self-tuning filters (STF) for detecting the positive sequence fundamental component of load current. For enhancing the performance of the inner current loop under unbalanced and distorted grid voltage conditions, an additional STF is employed in the control system to extract fundamental component of the grid voltage. STF can be represented by (3.7) and (3.8), where x^{α} and x^{β} are the input signals and x_1^{α} and x_1^{β} are the output signals of STF in two-phase frame respectively (Refer Appendix B for derivation). Figure 3.3 shows the frequency response of STF for different K values.

$$x_1^{\alpha}(s) = \frac{K}{s} \left[x^{\alpha}(s) - x_1^{\alpha}(s) \right] - \frac{\omega_1}{s} x_1^{\beta}(s) \tag{3.7}$$

$$x_1^{\beta}(s) = \frac{K}{s} \left[x^{\beta}(s) - x_1^{\beta}(s) \right] + \frac{\omega_1}{s} x_1^{\alpha}(s) \tag{3.8}$$

The frequency response of STF shows that the phase angle at the fundamental frequency is zero, unlike the conventional low pass filters. Moreover, the passband cut off frequency is at the fundamental frequency, with a narrow bandwidth. The STF eliminates both the lower order and higher order harmonics effectively.

The power calculated in outer loop, P_{dc} is added with the instantaneous real power needed for harmonic compensation $p_h(t)$. The reference currents for compensation are

36
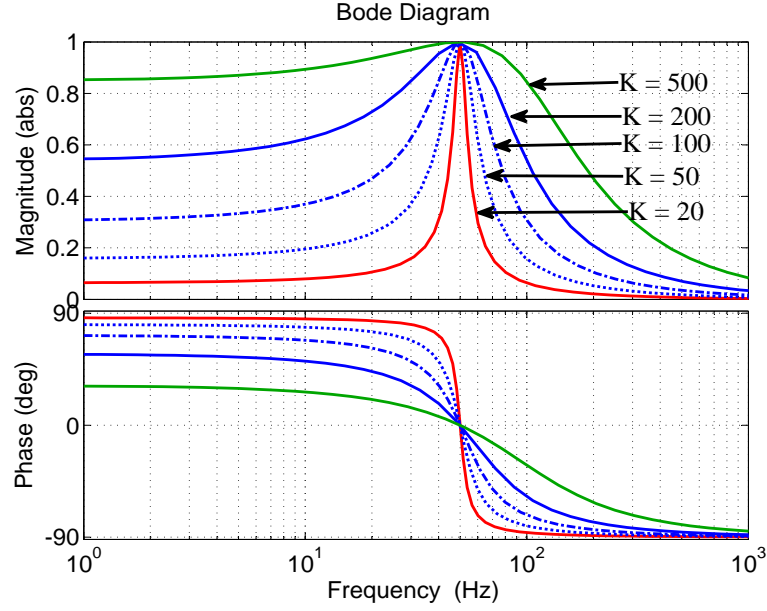
Figure 3.3: Frequency response of STF for different values of 'K'

calculated using (3.9), where $K_{\alpha\beta} = (v_{sp1}^{\alpha})^2 + (v_{sp1}^{\beta})^2$.

$$\begin{bmatrix} i_{ref}{}^{\alpha} \\ i_{ref}{}^{\beta} \\ i_{ref}{}^{0} \end{bmatrix} = \frac{1}{K_{\alpha\beta}} \begin{bmatrix} v_{sp1}^{\alpha} & -v_{sp1}^{\beta} & 0 \\ v_{sp1}^{\beta} & v_{sp1}^{\alpha} & 0 \\ 0 & 0 & K_{\alpha\beta} \end{bmatrix} \begin{bmatrix} p_h + p_{dc} - p_{RES} \\ q \\ i_0 \end{bmatrix} \tag{3.9}$$

The reference currents in abc frame are calculated using (3.10). The neutral current can be calculated using (3.11).

$$\begin{bmatrix} i_{ref}^{a} \\ i_{ref}^{b} \\ i_{ref}^{c} \end{bmatrix} = \sqrt{\frac{2}{3}} \begin{bmatrix} 1 & 0 & \frac{1}{\sqrt{2}} \\ -\frac{1}{2} & \frac{\sqrt{3}}{2} & \frac{1}{\sqrt{2}} \\ -\frac{1}{2} & -\frac{\sqrt{3}}{2} & \frac{1}{\sqrt{2}} \end{bmatrix} \begin{bmatrix} i_{ref}^{\alpha} \\ i_{ref}^{\beta} \\ i_{ref}^{0} \end{bmatrix} \tag{3.10}$$

$$i_{ref}^{n} = i_{ref}^{a} + i_{ref}^{b} + i_{ref}^{c} \tag{3.11}$$

The reference currents i_{ref}^{abcn} are compared with inverter currents i_c^{abcn}, and the gating signals for the inverter are generated using hysteresis control.

37

3.2.2   Fuzzy-DSTF-pq Controller for SHAF

The schematic diagram of the Fuzzy-DSTF-pq Controller based control system is shown in Figure 3.4. The outer loop is implemented using adaptive Fuzzy logic, and the inner loop using instantaneous power theory with DSTF. The inherent adaptive nature of the controller towards system parameter variations improves the dynamic performance of the system.
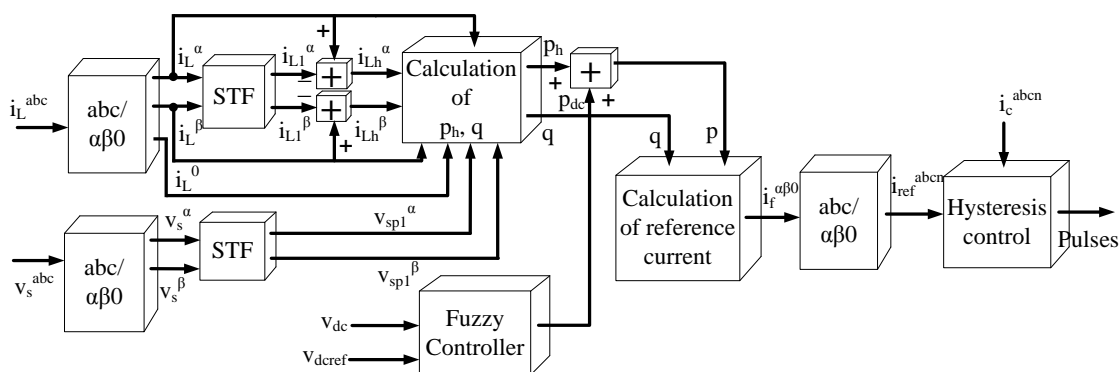
Figure 3.4: Fuzzy-DSTF-pq Controller

3.2.2.1   Dc-link Voltage Control Loop

In Fuzzy-DSTF-pq controller, the PI controller in PI-DSTF-pq controller is replaced by a non-linear adaptive Fuzzy controller. Following seven Fuzzy levels are chosen for each input and output variables; '–ve big (NB)', '–ve medium (NM)', '–ve small (NS)', 'zero error (ZE)', '+ve small (PS)', '+ve medium (PM)' and '+ve big (PB)'. Fuzzy rule table is formed as shown in Table3.1 based on the fact that control output should be large if the error is large. When the error is small, the control output should be small for fine tuning the error (Mikkili and Panda, 2011). Fuzzy rules are formed according to the rule table, where 'e' is the DC-link voltage error and '$\int e$' is the integral of DC-link voltage error.

Input membership functions are normalized by multiplying input variables with input control gains k_e and k_{ie}. Normalized input and output membership functions are shown in Figure 3.5. Centroid method is used for defuzzification. The output variable

38

Table 3.1: Fuzzy Rule Table

$\int e$ e	NB	NM	NS	ZE	PS	PM	PB
NB	NB	NB	NB	NB	NM	NS	ZE
NM	NB	NB	NB	NM	NS	ZE	PS
NS	NB	NB	NM	NS	ZE	PS	PM
ZE	NB	NM	NS	ZE	PS	PM	PB
PS	NM	NS	ZE	PS	PM	PB	PB
PM	NS	ZE	PS	PM	PB	PB	PB
PB	ZE	PS	PM	PB	PB	PB	PB
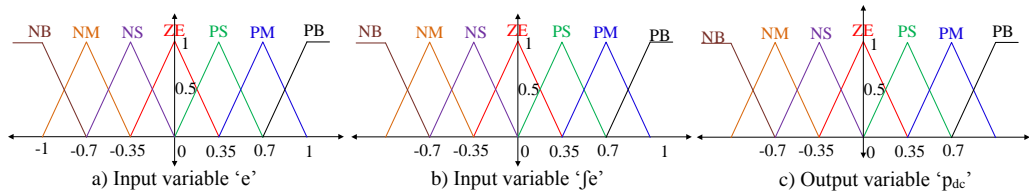
Figure 3.5: Normalized membership functions of a) Input variable 'e', b) input variable '$\int e$' and c) Output variable 'p_{dc}'

is multiplied with the output control gain (k_o) to get the output 'P_{dc}', which represents the power flow to the capacitor for keeping DC-link voltage constant.

3.2.2.2 *Design of Current Harmonic Compensation Loop*

The current harmonic compensation loop remains same as in PI-DSTF-pq controller, as shown in (3.3 – 3.11). The gating signals for the inverter are generated using hysteresis control.

3.2.3 BSC-DSTF-pq Controller for SHAF

The schematic diagram of the Back Stepping Controller based control system is shown in Figure 3.6.
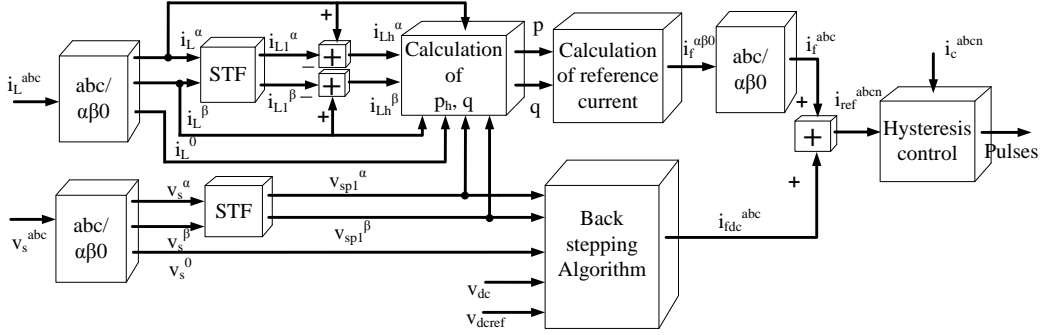
Figure 3.6: BSC-DSTF-pq Controller

3.2.3.1 Dc-link Voltage Control Loop

The Back Stepping algorithm is a non-linear control algorithm, where Lyapunov theory of stability is used for deriving the control law. According to Lypunov theory,

"A system is stable at the point x if there is a function continually derivable $U(x)$ that satisfy:

$U(0) = 0$

$U(x) > 0; \forall x \neq 0, x \in \Omega$

$\dot{U}(x) < 0; \forall x \neq 0, x \in \Omega$; Where Ω is the domain of study ", (Ghamri et al., 2015).

Energy stored in DC-link capacitor can be written as a function of V_{dc} as shown in (3.12).

$$E_{dc} = \frac{1}{2} C_{dc} V_{dc}^2 \tag{3.12}$$

The derivative of E_{dc} can be written as shown in (3.13).

$$\dot{E_{dc}} = P_{dc} = P_s + P_{RES} - P_{Rdc} - P_{sw} \tag{3.13}$$

P_s is the power supplied by the network to maintain the charge in DC-link capacitor, P_{RES} is the power injected by renewable sources, P_{Rdc} is the losses in leakage resistance of DC-link capacitor, , and P_{sw} is the inverter switching loss. Mathematical models of P_s, P_{Rdc} & P_{RES} are shown in (3.14), (3.15) and (3.16) respectively. P_{sw} is treated as

an unknown parameter.

$$P_s = v_s^a i_{dc}^a + v_s^b i_{dc}^b + v_s^c i_{dc}^c \tag{3.14}$$

Where v_s^a, v_s^b, $\& v_s^c$ are the three phase grid voltages and i_{dc}^a, i_{dc}^b, $\& i_{dc}^c$ are the three phase inverter current components for DC voltage control.

$$P_{RES} = i_{dc} v_{dc} \tag{3.15}$$

$$P_{Rdc} = \frac{v_{dc}^2}{R_{dc}} \tag{3.16}$$

Where i_{dc} is the DC current from RES to DC-link capacitor and R_{dc} is the leakage resistance of DC capacitor.

The control objective is to keep the DC voltage tracking error as small as possible. If z is the voltage tracking error, it can be represented as shown in (3.17).

$$z = x^* - x \tag{3.17}$$

Where x is energy stored in DC capacitor and x^* is the reference value of energy stored in DC-link voltage. The derivative of (3.17) can be written as shown in (3.18).

$$\dot{z} = \dot{x^*} - \dot{x} = \dot{x^*} - P_s - P_{RES} + P_{Rdc} + P_{sw} \tag{3.18}$$

Equation (3.19) is obtained by substituting (3.15) and (3.16) in (3.18).

$$\dot{z} = \dot{x^*} - P_s - i_{dc}\sqrt{\frac{2x}{C_{dc}}} + \frac{2x}{C_{dc}R_{dc}} + P_{sw} \tag{3.19}$$

For obtaining a stabilized control law, introducing a Lyapunov function as shown in (3.20).

$$V = \frac{1}{2}z^2 + \frac{1}{2\gamma}\tilde{P_{sw}}^2 \tag{3.20}$$

Where $\tilde{P_{sw}} = \hat{P_{sw}} - P_{sw}$ is the estimation error of P_{sw} and γ is a positive design

parameter. Equation (3.21) is obtained by differentiating (3.20).

$$\dot{V} = z\dot{z} + \frac{1}{\gamma}\tilde{P_{sw}}\dot{\tilde{P}}_{sw} \tag{3.21}$$

Substituting (3.19) in (3.21), equation (3.22) can be derived.

$$\dot{V} = z\left[\dot{x^*} - P_s - i_{dc}\sqrt{\frac{2x}{C_{dc}}} + \frac{2x}{C_{dc}R_{dc}} + P_{sw}\right] + \frac{1}{\gamma}\tilde{P_{sw}}\dot{\tilde{P}}_{sw} \tag{3.22}$$

Substituting $P_{sw} = \hat{P_{sw}} - \tilde{P_{sw}}$ in (3.22), equation (3.23) is obtained.

$$\dot{V} = z\left[\dot{x^*} - P_s - i_{dc}\sqrt{\frac{2x}{C_{dc}}} + \frac{2x}{C_{dc}R_{dc}} + \hat{P_{sw}} - \tilde{P_{sw}}\right] + \frac{1}{\gamma}\tilde{P_{sw}}\dot{\tilde{P}}_{sw} \tag{3.23}$$

Rearranging (3.23), equation (3.24) is derived.

$$\dot{V} = z\left[\dot{x^*} - P_s - i_{dc}\sqrt{\frac{2x}{C_{dc}}} + \frac{2x}{C_{dc}R_{dc}} + \hat{P_{sw}}\right] + \tilde{P_{sw}}\left(\frac{1}{\gamma}\dot{\tilde{P}}_{sw} - z\right) \tag{3.24}$$

For making $\dot{V} <= 0$, equating the terms in square bracket to $-cz$ as shown in (3.25); where c is a positive design parameter.

$$\dot{x^*} - P_s - i_{dc}\sqrt{\frac{2x}{C_{dc}}} + \frac{2x}{C_{dc}R_{dc}} + \hat{P_{sw}} = -cz \tag{3.25}$$

The control law, shown in (3.26) and the parameter adaptation law, shown in (3.27) are derived from (3.25) and (3.24) respectively.

$$P_s = \dot{x^*} - i_{dc}\sqrt{\frac{2x}{C_{dc}}} + \frac{2x}{C_{dc}R_{dc}} + \hat{P_{sw}} + cz \tag{3.26}$$

$$\dot{\hat{P}}_{sw} = \gamma z \tag{3.27}$$

Equation (3.28) is derived from (3.14)and (3.26). The inverter current references for

DC voltage control can be calculated using (3.28).

$$
\begin{bmatrix} i_{dc}^a \\ i_{dc}^b \\ i_{dc}^c \end{bmatrix} = \frac{1}{(v_s^a)^2 + (v_s^b)^2 + (v_s^c)^2} \begin{bmatrix} v_s^a \left(\dot{x}^* - i_{dc}\sqrt{\dfrac{2x}{C_{dc}}} + \dfrac{2x}{C_{dc}R_{dc}} + \hat{P_{sw}} + cz \right) \\ v_s^b \left(\dot{x}^* - i_{dc}\sqrt{\dfrac{2x}{C_{dc}}} + \dfrac{2x}{C_{dc}R_{dc}} + \hat{P_{sw}} + cz \right) \\ v_s^c \left(\dot{x}^* - i_{dc}\sqrt{\dfrac{2x}{C_{dc}}} + \dfrac{2x}{C_{dc}R_{dc}} + \hat{P_{sw}} + cz \right) \end{bmatrix}
$$
(3.28)

The neutral current can be calculated using (3.29).

$$
i_{dc}^n = i_{dc}^a + i_{dc}^b + i_{dc}^c
$$
(3.29)

3.2.3.2   *Design of Current Harmonic Compensation Loop*

In the current harmonic compensation loop, the instantaneous real power needed for harmonic compensation, and instantaneous imaginary power needed for reactive power compensation are calculated using (3.5) and (3.6) respectively. The reference currents for harmonic compensation are calculated using (3.30), where $K_{\alpha\beta} = (v_{sp1}^\alpha)^2 + (v_{sp1}^\beta)^2$.

$$
\begin{bmatrix} i_f{}^\alpha \\ i_f{}^\beta \\ i_f{}^0 \end{bmatrix} = \frac{1}{K_{\alpha\beta}} \begin{bmatrix} v_{sp1}^\alpha & -v_{sp1}^\beta & 0 \\ v_{sp1}^\beta & v_{sp1}^\alpha & 0 \\ 0 & 0 & K_{\alpha\beta} \end{bmatrix} \begin{bmatrix} p_h \\ q \\ i_0 \end{bmatrix}
$$
(3.30)

The reference currents in abc frame are calculated using (3.31). The neutral current is calculated using (3.32).

$$
\begin{bmatrix} i_f^a \\ i_f^b \\ i_f^c \end{bmatrix} = \sqrt{\frac{2}{3}} \begin{bmatrix} 1 & 0 & \frac{1}{\sqrt{2}} \\ -\frac{1}{2} & \frac{\sqrt{3}}{2} & \frac{1}{\sqrt{2}} \\ -\frac{1}{2} & -\frac{\sqrt{3}}{2} & \frac{1}{\sqrt{2}} \end{bmatrix} \begin{bmatrix} i_f^\alpha \\ i_f^\beta \\ i_f^0 \end{bmatrix}
$$
(3.31)

$$
i_f^n = i_f^a + i_f^b + i_f^c
$$
(3.32)

The reference currents for the inverter is the sum of i_f^{abcn} and i_{dc}^{abcn}. The reference

43

currents i_{ref}^{abcn} are compared with inverter currents i_c^{abcn}, and the gating signals for the inverter are generated using hysteresis control.

3.2.3.3   Stability analysis of BSC

The closed loop control system can be expressed in the form of $\dot{X} = AX$ as shown in (3.33), where c and γ are positive real values. The eigenvalues of the matrix A are the zeroes of the polynomial $P(\theta) = \theta^2 + c\theta + \gamma$

$$
\begin{bmatrix} \dot{z} \\ \dot{\tilde{P}_{sw}} \end{bmatrix} = \begin{bmatrix} -c & 1 \\ \gamma & 0 \end{bmatrix} \begin{bmatrix} z \\ \tilde{P}_{sw} \end{bmatrix}
\tag{3.33}
$$

The roots of the polynomial have negative real values if $c > 2\sqrt{\gamma}$. Hence, according to Hurwitz criterion, z(t) and $\tilde{P}_{sw}(t)$ are bounded. The Lyapunov function V is given by (3.20). Taking the derivative of V with respect to time, after some mathematical simplifications, expression (3.34) is obtained.

$$
\dot{V} = -cz^2 + \frac{3}{2}\tilde{P}_{sw}z
\tag{3.34}
$$

Taking derivative of $\dot{V}$ with respect to time and simplifying, (3.35) is obtained.

$$
\ddot{V} = -2c^2z^2 - 2cz\tilde{P}_{sw} + \frac{3}{2}(cz\tilde{P}_{sw} + \tilde{P}_{sw}^2 + z^2\gamma)
\tag{3.35}
$$

Since z(t) and $\tilde{P}_{sw}(t)$ are bounded, $\ddot{V}$ is also bounded. Therefore, according to Barbalat's Lemma, it can be said that $\dot{V} \to 0$ as $t \to \infty$. From (3.35), it can be said that $z(t), \tilde{P}_{sw}(t) \to 0$ as $t \to \infty$ (Jean-Jacques Slotine, 1991).

3.3   SIMULATION RESULTS AND ANALYSIS

Numerical simulations are carried out in MATLAB/Simulink platform with dynamic models of wind and solar systems. The system parameters used in simulation are listed in Table 3.2. List of harmonic components present in the load considered is shown in 3.3. The power circuit of the system considered for simulation is shown in Figure 3.7.

The rated power generations from the wind and solar systems are considered as 15 kW (at wind speed of 12 m/s and solar irradiation 1 kW/m^2 respectively). Three-phase four leg IGBT inverter is used as grid interfacing inverter (Mikkili and Panda, 2011). The k_p and k_i values used for simulation are 0.11 and 1.05 respectively. The input control gains (k_e and k_{ie}) and output control gain (k_o) used in Fuzzy controller are ($1/700^2$), ($20/700^2$) and 5.6×10^4 respectively. The Back Stepping Controller parameters c and γ used in the simulation are 200 and 2500 respectively. The effectiveness of controllers are tested by simulating different system conditions.
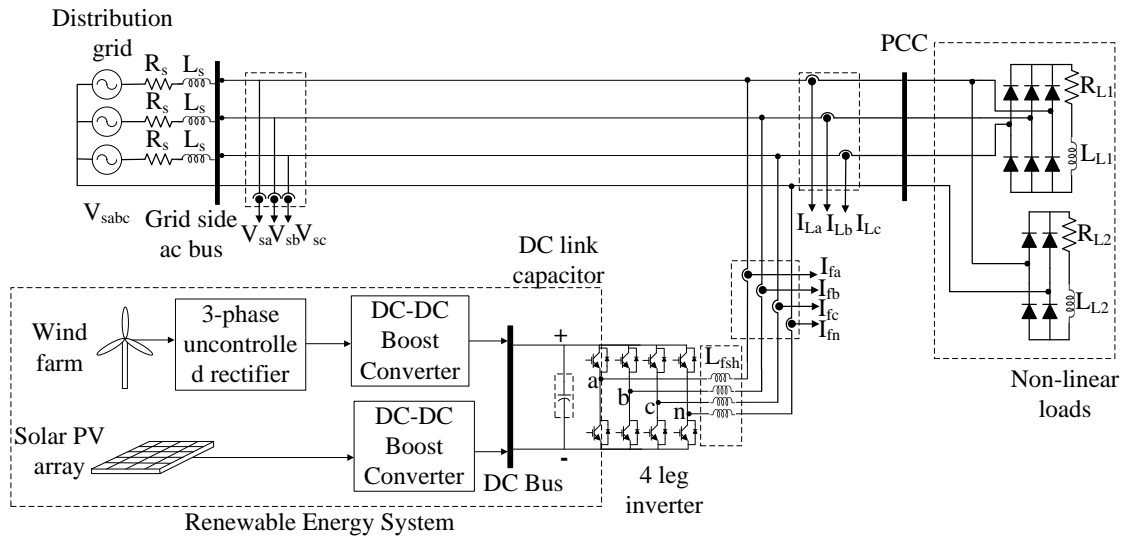
Figure 3.7: Power circuit of the system considered for simulation

Table 3.2: SHAF parameters

Sl. No	Particulars	Values
1	Supply Voltage	3Φ, 400 V (Line–line, RMS), 50Hz
2	Source Parameters	0.01mH, 0.1 Ω
3	DC-link capacitance	2350 μF
4	DC-link voltage	700V
5	Filter Parameters	5mH, 0.1 Ω
6	Load parameters	9 kW Non-linear load. (Three-phase rectifier with 30 Ω, 48 mH load)
7	Inverter parameters	4-leg IGBT H-bridge inverter

Table 3.3: List of harmonic components present in the load considered

Order of harmonics	Magnitude in %
1	100
5	19.59
7	11.27
11	6.08
13	4.28
17	2.22

3.3.1 Steady state condition

The performance of the controller is analysed for two different cases, (i) renewable power generation is greater than the load demand ($P_{RES} > P_L$), and (ii) renewable power generation is less than the load demand ($P_{RES} < P_L$). The steady state waveforms for $P_{RES} > P_L$ is shown in Figure 3.8(a). In this case, 12 m/s wind speed and 1 kW/m^2 solar irradiation are considered.

The active power plots, DC-link voltage, grid voltages, load currents, compensation currents and grid currents for $P_{RES} > P_L$ are shown in Figure 3.8(a). It is observed that the load demand is met by the power generated by renewable sources, and the excess power is injected into the grid. The grid currents and grid voltages in each phase are out of phase by 180^0, as the power is injected into the grid. The steady-state waveforms for $P_{RES} < P_L$ is shown in Figure 3.8(b). In this case, 3 m/s wind speed and 250 W/m^2 solar irradiation are considered.

It is observed that the total power generated by renewable sources are less than load demand, and power flows from grid to the load to meet the load demand. The grid currents and grid voltages in each phase are in phase. The grid current harmonics are effectively reduced to the IEEE prescribed limit by the proposed BSC-DSTF controller in both the cases. The steady state performance of BSC-DSTF is compared with PI-LPF, PI-DTSF and Fuzzy-DSTF controllers under (i) ideal grid voltage, (ii) unbalanced grid voltage, (iii) distorted grid voltage and (iv) unbalanced load conditions. Following subsections discusses the results of steady-state comparative study.
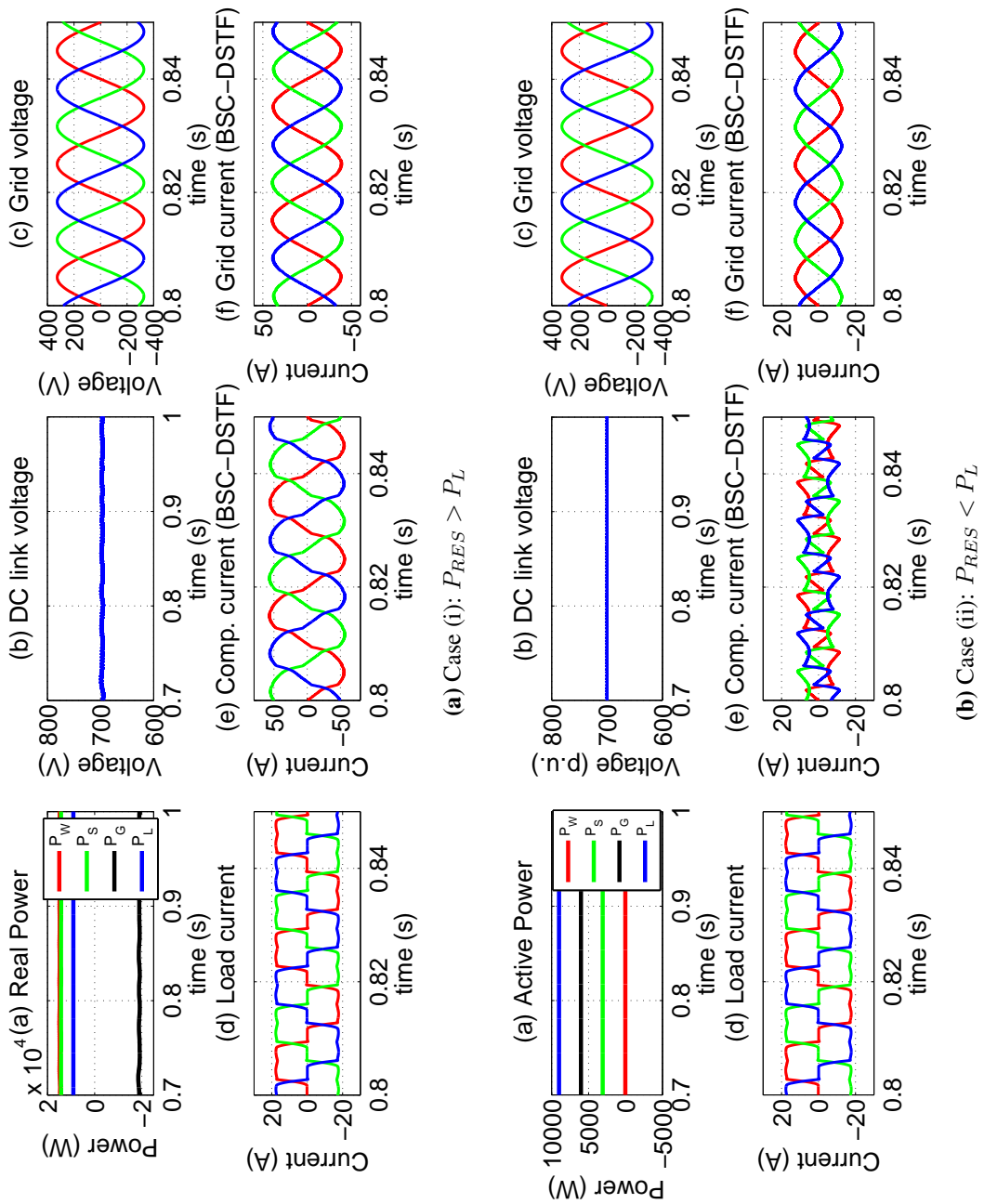
Figure 3.8: Steady state waveforms

3.3.1.1 Case 1: Ideal grid voltage condition

In this case, undistorted and balanced grid voltage condition is considered. The load is non-linear and balanced. The grid voltage and current waveforms for $P_{RES} > P_L$ condition, with PI-LPF, PI-DTSF, Fuzzy-DSTF and BSC-DSTF controllers are shown in Figure 3.9. The harmonic analysis results are shown in Figure 3.10. The results show that PI-DTSF, Fuzzy-DSTF and BSC-DSTF controllers offer similar harmonic current mitigation property. They are superior to PI-LPF controller, for $P_{RES} > P_L$ case, under ideal grid voltage condition.

Figure 3.11 shows the grid voltage and current waveforms for $P_{RES} < P_L$ condition. The harmonic analysis results for this case is shown in Figure 3.12. In this case also PI-DTSF, Fuzzy-DSTF and BSC-DSTF controllers show improved harmonic current mitigation property compared to PI-LPF. The controllers PI-DTSF, Fuzzy-DSTF and BSC-DSTF offer similar steady state results in this case too.

3.3.1.2 Case 2: Unbalanced grid voltage condition

An unbalance in grid voltage is simulated by increasing phase A voltage by 10%, keeping all other phase voltages at nominal values. The load is non-linear and balanced. The grid voltage and current waveforms and corresponding harmonic analysis results with all four controllers, for $P_{RES} > P_L$ condition are shown in Figure 3.13 and 3.14 respectively. It is observed that the grid current THD exceeds the prescribed IEEE limit when PI-LPF controller is used. The grid current THDs similar and are within the limits with PI-DTSF, Fuzzy-DSTF and BSC-DSTF controllers.

Figure 3.15 and 3.16 shows the grid voltage and current waveforms, and harmonic analysis results for $P_{RES} < P_L$ condition respectively. In this case also an unbalance in grid voltage is considered. The results shows that in this case also PI-DTSF, Fuzzy-DSTF and BSC-DSTF controllers controllers offers better harmonic current mitigation compared to PI-LPF controller. Grid current THD in all three phases are within IEEE standards.

3.3.1.3 Case 3: Distorted grid voltage condition

In this case, a 5% grid voltage distortion (4% fifth harmonics and 3% seventh harmonics) is simulated. The load is non-linear and balanced. The grid voltage and current waveforms under distorted grid voltage condition for $P_{RES} > P_L$ case is shown in Figure 3.17. From the harmonic analysis results shown in Figure 3.18, it is observed that, with PI-LPF controller, the grid current THD exceeds the harmonic limits prescribed by IEEE-519. The grid current THD's with PI-DTSF, Fuzzy-DSTF and BSC-DSTF controllers are well within the limits.

The grid voltage and current waveforms under distorted grid voltage condition for $P_{RES} < P_L$ case is shown in Figure 3.19. The harmonic analysis results for this case is shown in Figure 3.20. It is observed that in this case also DSTF based controllers offer better harmonic mitigation property than PI-LPF controller. PI-DTSF, Fuzzy-DSTF and BSC-DSTF offer similar steady state performance in this case too.

3.3.1.4 Case 4: Unbalanced load condition

In this case, the load is non-linear and unbalanced. Along with the existing three-phase rectifier load, a single phase rectifier with 60 Ω, 48 mH load is connected in A phase for simulating unbalanced load condition. The grid voltage condition is considered as balanced and undistorted. The grid voltage and current waveforms for $P_{RES} > P_L$ condition, with different controllers are shown in Figure 3.21. The harmonic analysis results are shown in Figure 3.22. it is observed that all three DSTF based controllers offer better harmonic current mitigation than PI-LPF controller.

Figure 3.23 shows the grid voltage and current waveforms for $P_{RES} < P_L$ condition. The harmonic analysis results for this case is shown in Figure 3.24. In this case, the grid current THD limits are violated when PI-LPF controller is used. The grid current THDs are under limits with PI-DTSF, Fuzzy-DSTF and BSC-DSTF controllers, for $P_{RES} < P_L$ case, under unbalanced load condition.
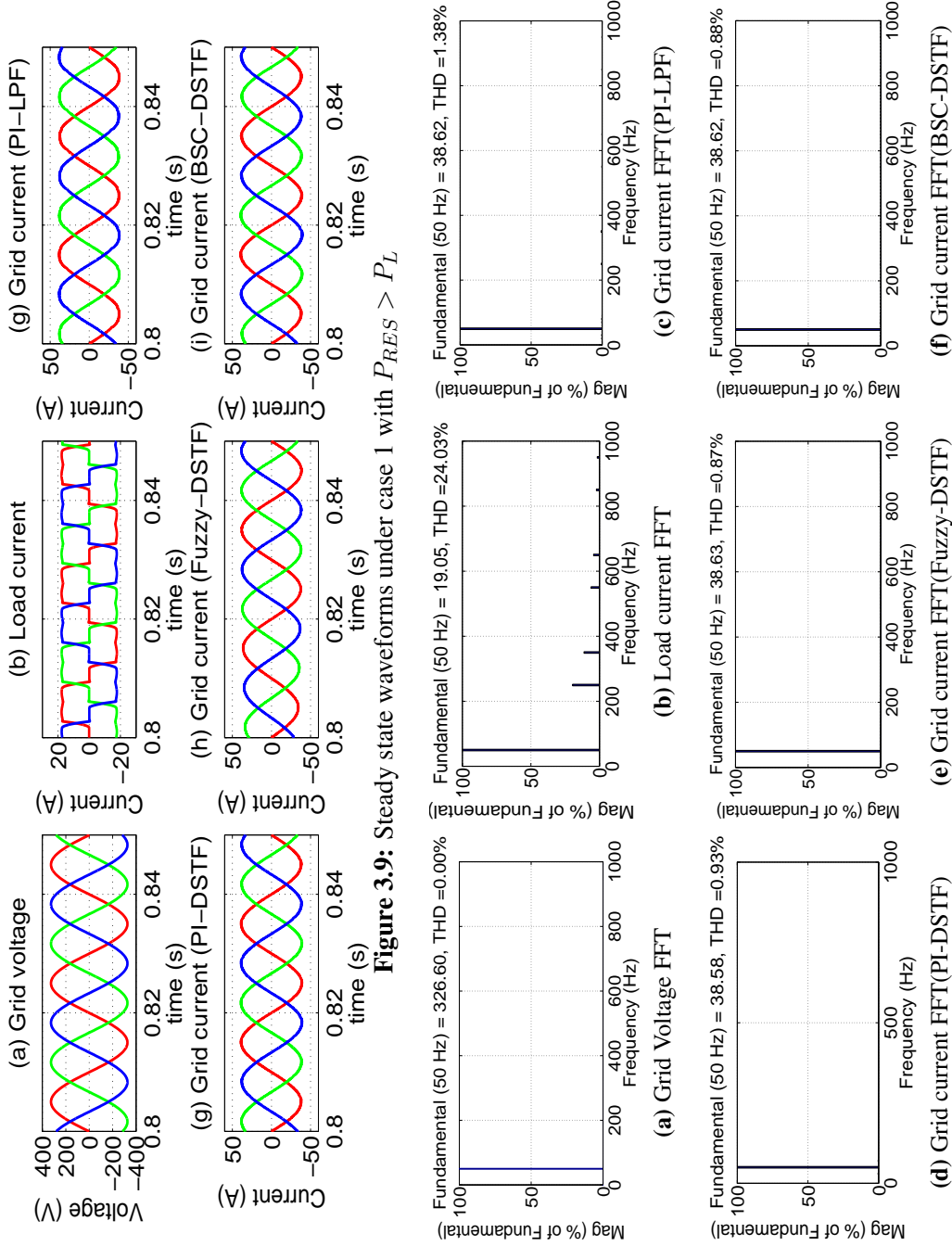
Figure 3.9: Steady state waveforms under case 1 with $P_{RES} > P_L$

Figure 3.10: Steady state harmonic analysis results of phase A under case 1 with $P_{RES} > P_L$
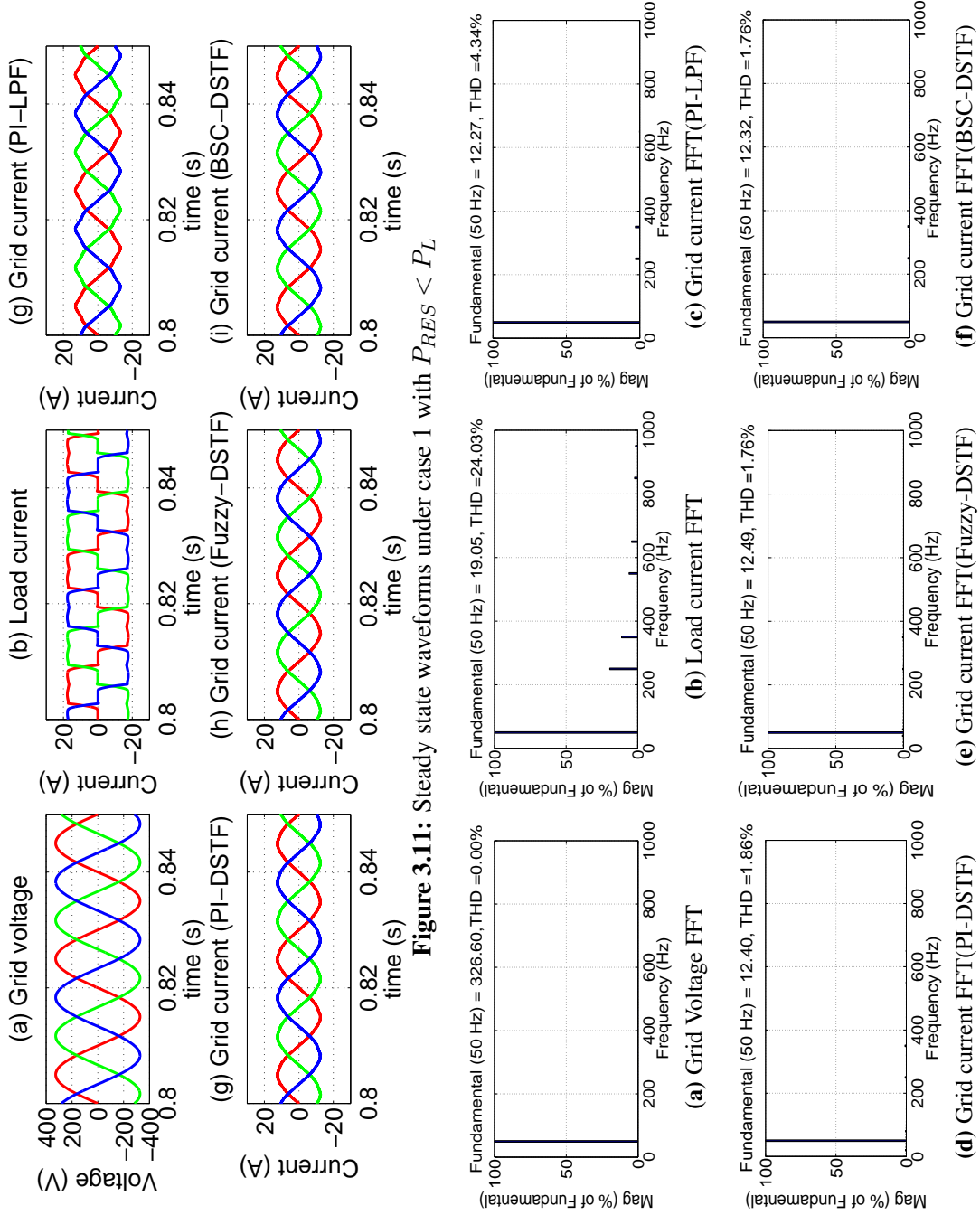
Figure 3.11: Steady state waveforms under case 1 with $P_{RES} < P_L$

Figure 3.12: Steady state harmonic analysis results of phase A under case 1 with $P_{RES} < P_L$

Figure 3.13: Steady state waveforms under case 2 with $P_{RES} > P_L$
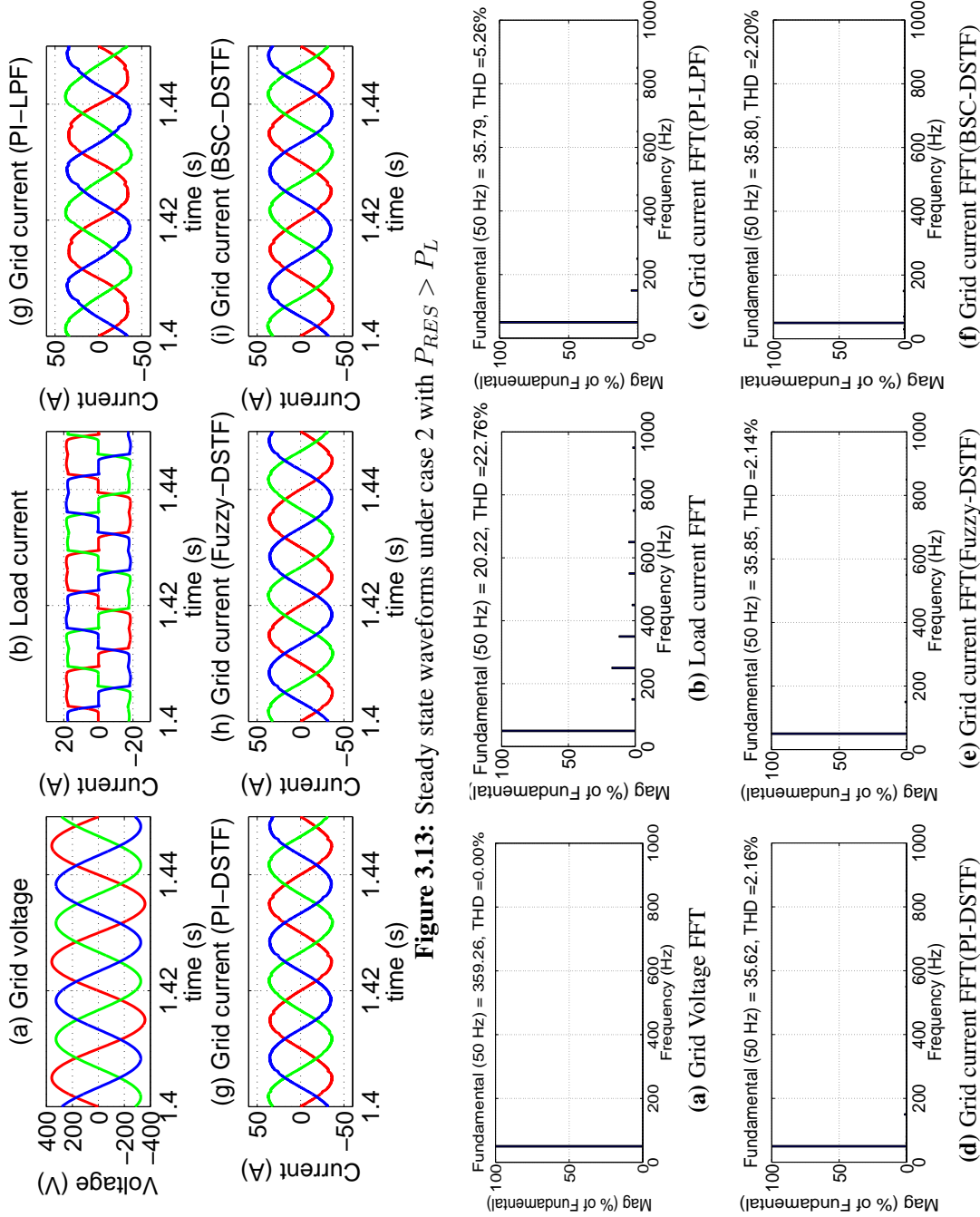
Figure 3.14: Steady state harmonic analysis results of phase A under case 2 with $P_{RES} > P_L$
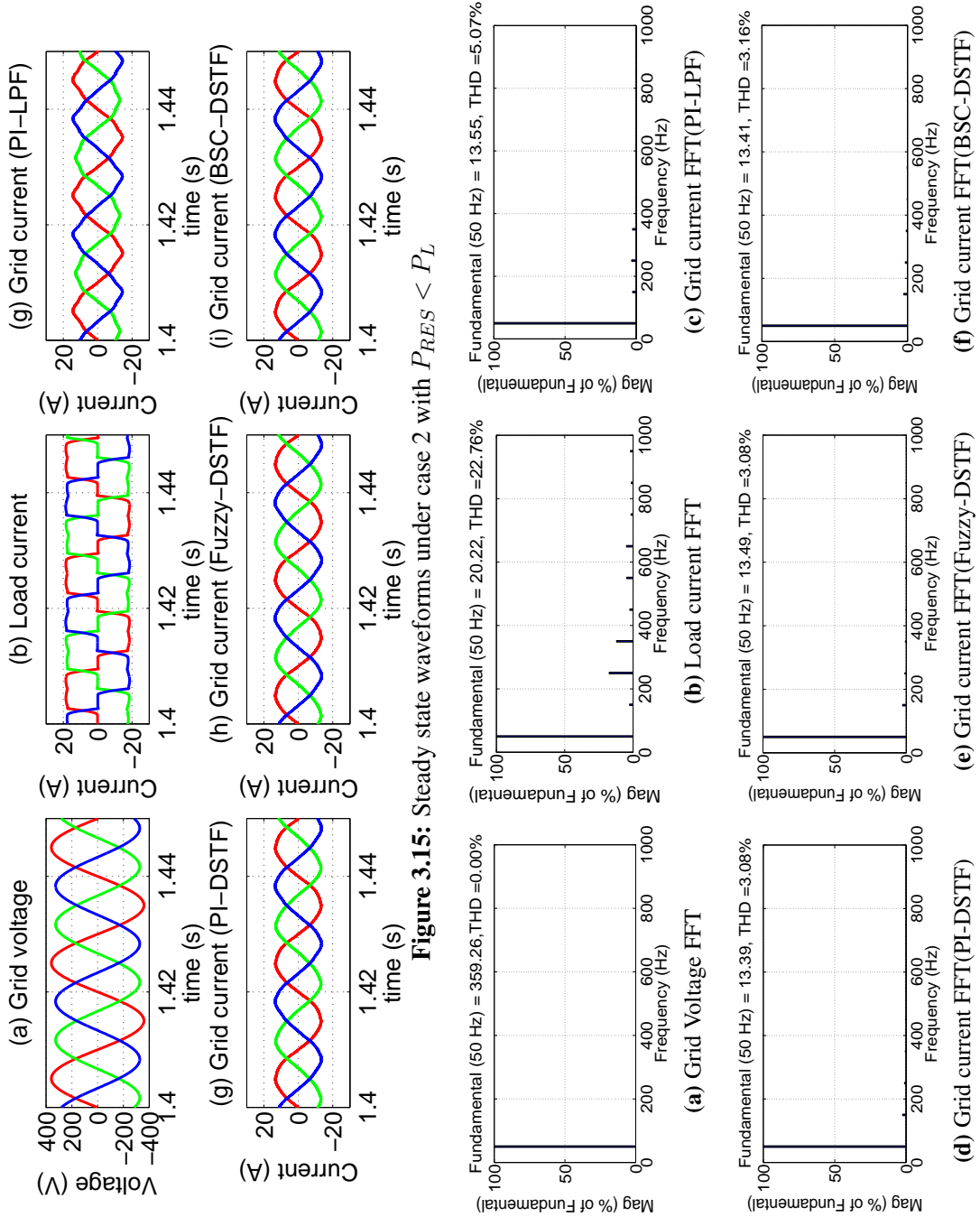
Figure 3.15: Steady state waveforms under case 2 with $P_{RES} < P_L$

Figure 3.16: Steady state harmonic analysis results of phase A under case 2 with $P_{RES} < P_L$
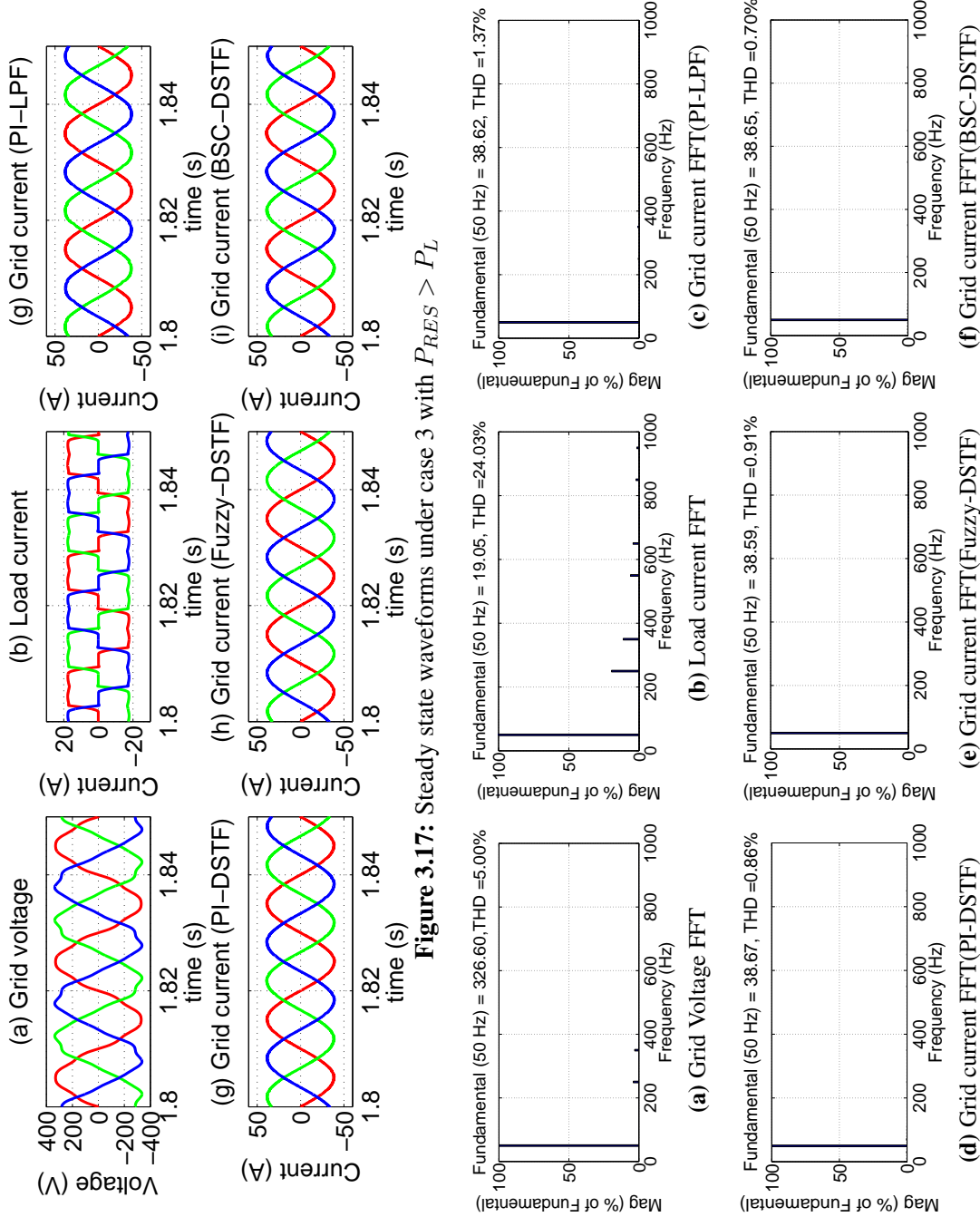
Figure 3.17: Steady state waveforms under case 3 with $P_{RES} > P_L$

Figure 3.18: Steady state harmonic analysis results of phase A under case 3 with $P_{RES} > P_L$
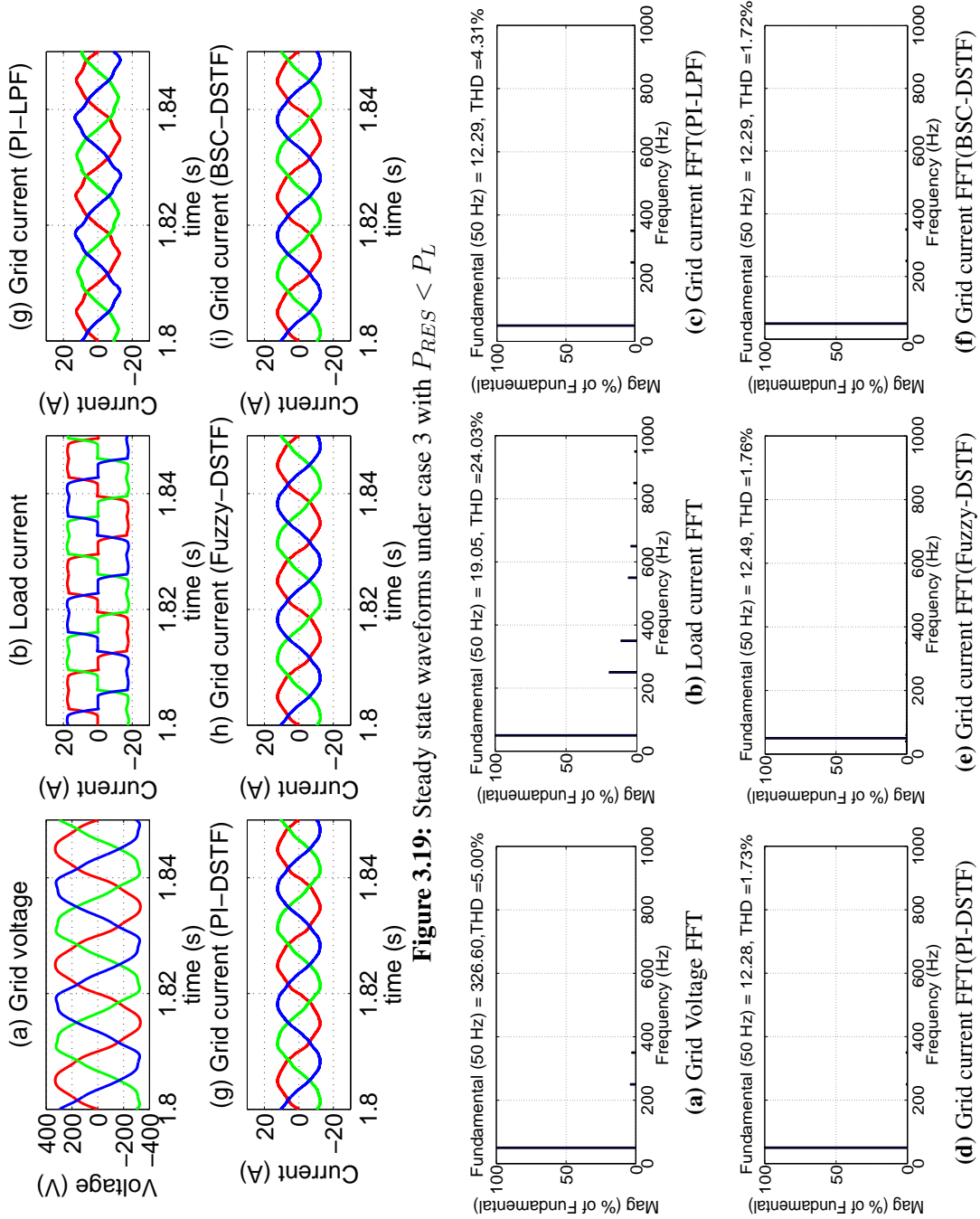
Figure 3.19: Steady state waveforms under case 3 with $P_{RES} < P_L$

Figure 3.20: Steady state harmonic analysis results of phase A under case 3 with $P_{RES} < P_L$
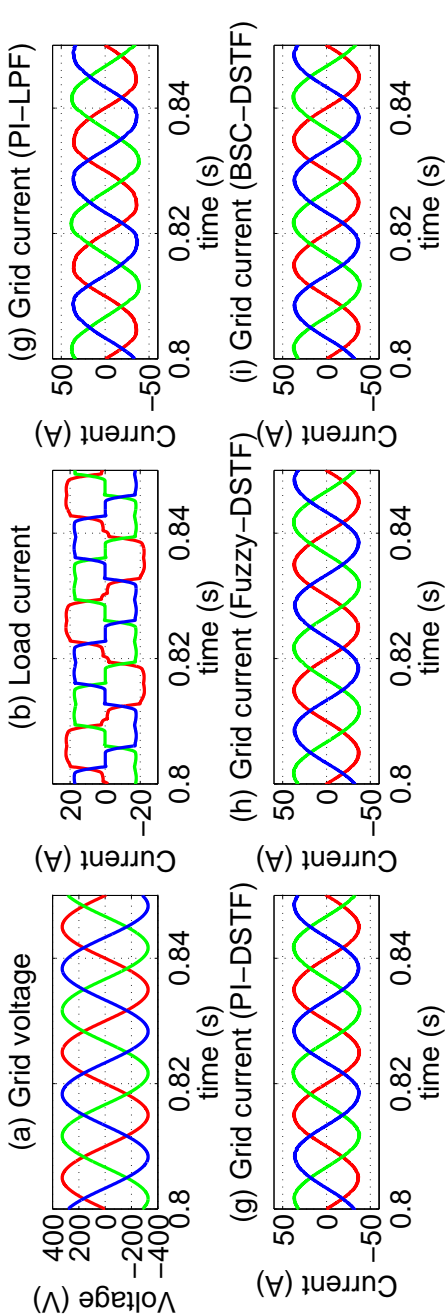
Figure 3.21: Steady state waveforms under case 4 with $P_{RES} > P_L$
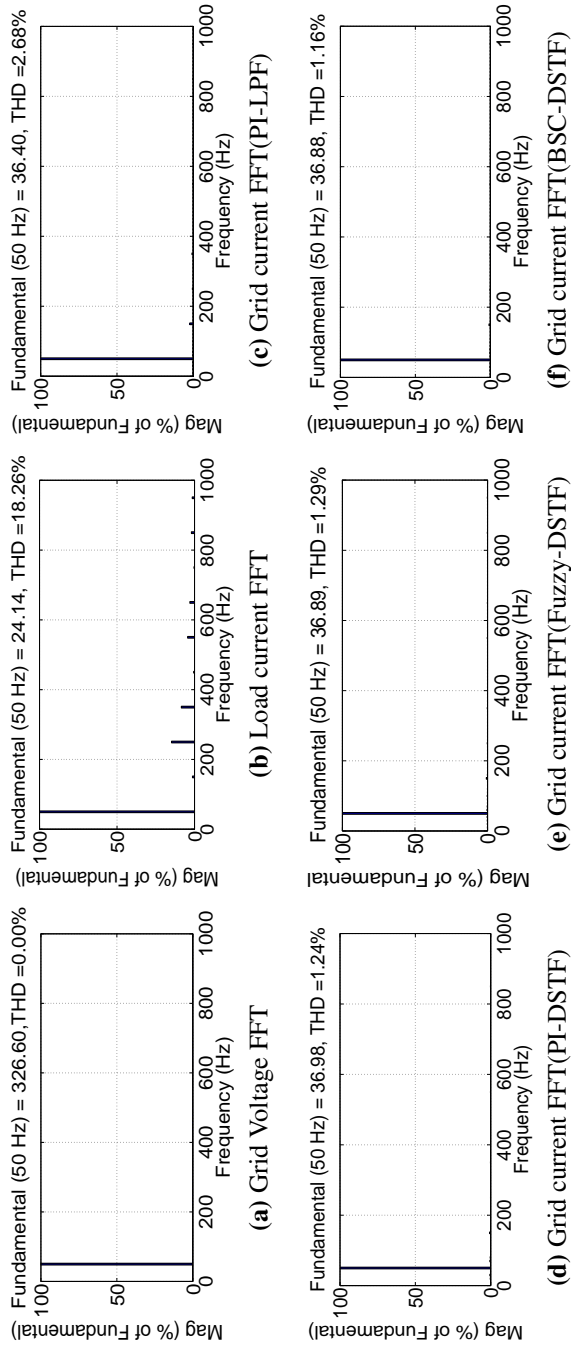
Figure 3.22: Steady state harmonic analysis results of phase A under case 4 with $P_{RES} > P_L$
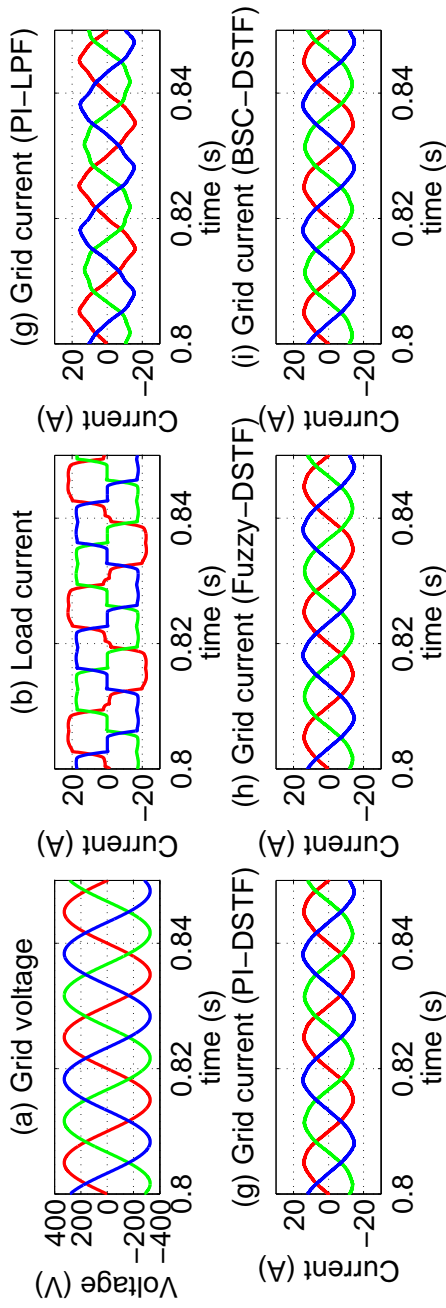
Figure 3.23: Steady state waveforms under case 4 with $P_{RES} < P_L$
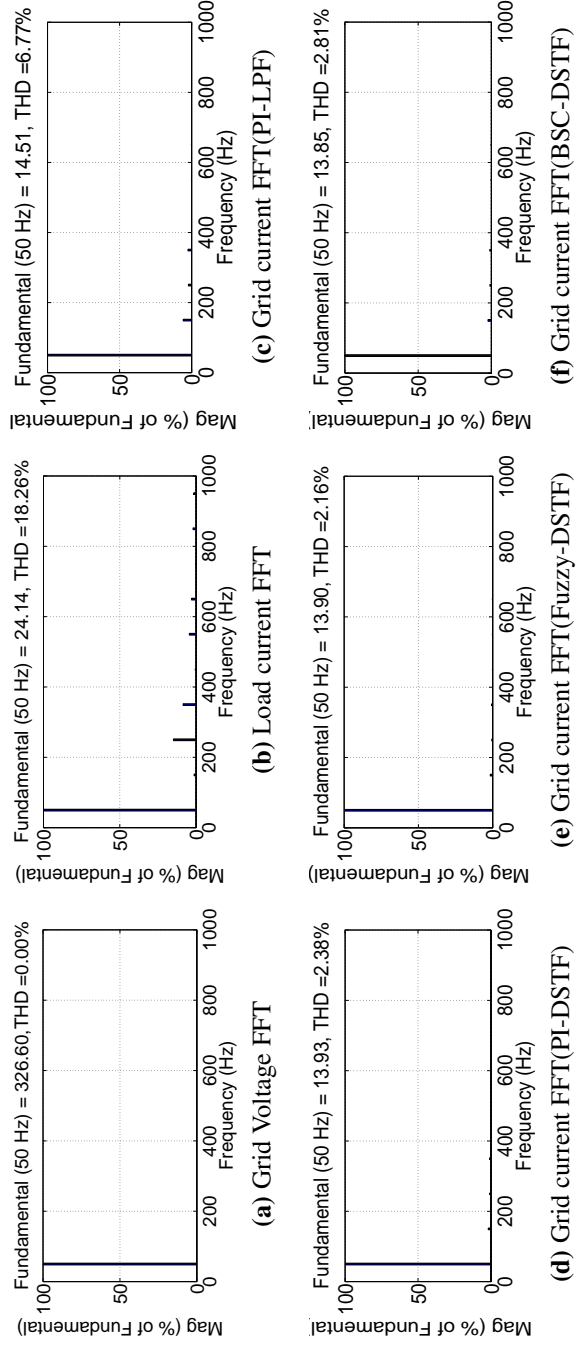
Figure 3.24: Steady state harmonic analysis results of phase A under case 4 with $P_{RES} < P_L$

The steady state results are summarized in table 3.4. From the grid current THD values for different steady state conditions listed in table, it is observed that DSTF based controllers possess superior harmonic current mitigation property compared to LPF based controller. The PI-DSTF, Fuzzy-DSTF and BSC-DSTF controllers have similar performance under different steady state conditions, because the outer DC-link voltage control loop have not affected the performance of the inner harmonic current mitigation loop.

Table 3.4: Summary of steady state results

Condition	Case	Phase	Load current THD	Grid current THD			
				PI-LPF	PI-DSTF	Fuzzy-DSTF	BSC-DSTF
Ideal grid	$P_{RES} > P_L$	A	24.03	1.38	0.93	0.87	0.88
		B	24.03	1.37	0.96	0.89	0.97
		C	24.03	1.38	0.97	0.87	0.94
	$P_{RES} < P_L$	A	24.03	4.34	1.86	1.76	1.76
		B	24.03	4.31	1.88	1.77	1.75
		C	24.03	4.34	1.88	1.79	1.74
Unbalanced grid voltage	$P_{RES} > P_L$	A	22.67	5.26	2.16	2.14	2.20
		B	24.59	4.72	1.72	1.57	1.83
		C	24.69	5.01	1.69	1.64	1.79
	$P_{RES} < P_L$	A	22.67	5.07	3.08	3.08	3.16
		B	24.59	5.46	3.44	3.22	3.42
		C	24.69	5.24	3.08	3.05	3.20
Distorted grid voltage	$P_{RES} > P_L$	A	24.03	1.37	0.86	0.91	0.70
		B	24.03	1.38	0.86	0.91	0.70
		C	24.03	1.38	0.87	0.90	0.75
	$P_{RES} < P_L$	A	24.03	4.31	1.73	1.76	1.72
		B	24.03	4.31	1.73	1.77	1.72
		C	24.03	4.29	1.74	1.79	1.74
Unbalanced load	$P_{RES} > P_L$	A	18.26	2.68	1.24	1.29	1.16
		B	24.11	2.76	1.25	1.08	1.19
		C	23.92	2.83	1.26	1.32	1.19
	$P_{RES} < P_L$	A	18.19	6.77	2.38	2.16	2.81
		B	24.03	7.94	2.38	2.16	2.81
		C	23.84	7.46	2.39	2.64	2.86

3.3.2 Dynamic conditions

Different dynamic conditions considered for analysing the dynamic behaviour of the system are starting, step change in wind speed and solar irradiation, a step change in load and a step change in DC-link reference voltage.

3.3.2.1 Starting

During starting, a 5 Ω resistor is included in series with the AC inductor filter to limit the huge inrush current. The resistor is removed after a few cycles by closing the switch connected across it. The real power and DC-link voltage waveforms are shown in Figure 3.25. It is observed that the DC-link voltage response is faster for BSC-DSTF controller compared to PI-DSTF and Fuzzy-DSTF. The grid currents during starting with each controller are shown in Figure 3.26. The initial transients are due to the DC-link capacitor charging and MPPT controller dynamics.
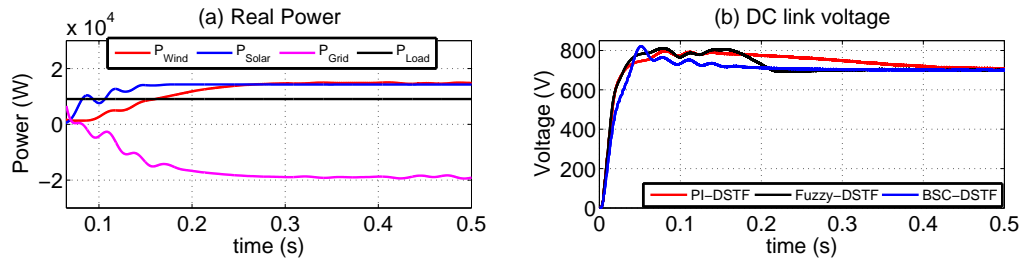
Figure 3.25: Power and DC-link voltage plots during starting
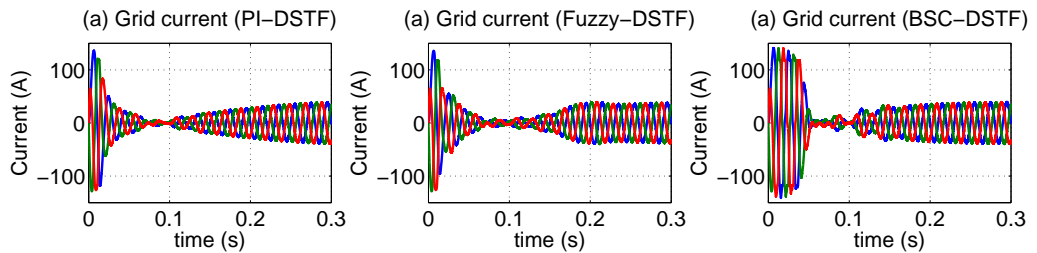
Figure 3.26: Grid current waveforms during starting

3.3.2.2 Step change in load

A 50% step decrement in load is simulated at 1 s. The real power and DC-link voltage waveforms during load increment are shown in Figure 3.27. It is observed that the DC-link voltage response is faster for BSC-DSTF controller compared to PI-DSTF and Fuzzy-DSTF. The grid currents during load decrement with each controllers are shown in Figure 3.28.
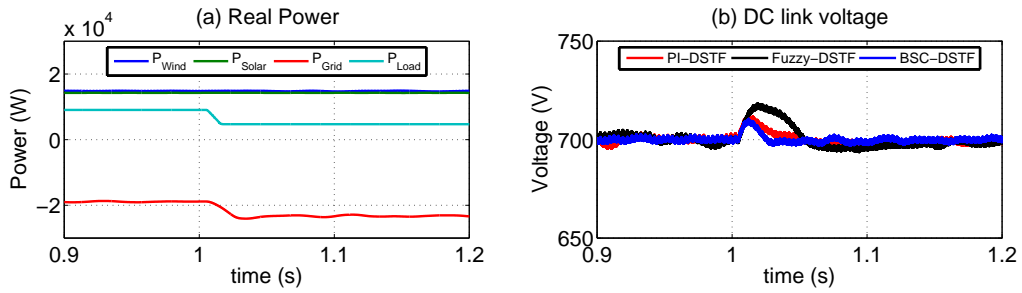
Figure 3.27: Power and DC-link voltage plots during 50% step decrement in load
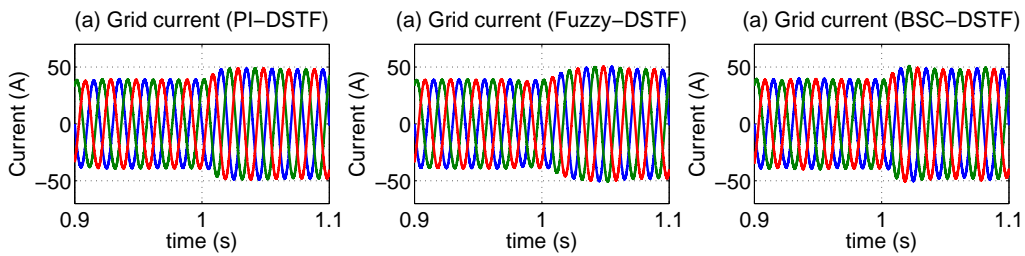
Figure 3.28: Grid current waveforms during during 50% step decrement in load

The load is brought back to the nominal value by step incrementing it 50% at 1.5 s . The real power and DC-link voltage are shown in Figure 3.29 and the grid current waveforms are shown in Figure 3.30. In this case also BSC-DSTF-pq controller offers faster response.
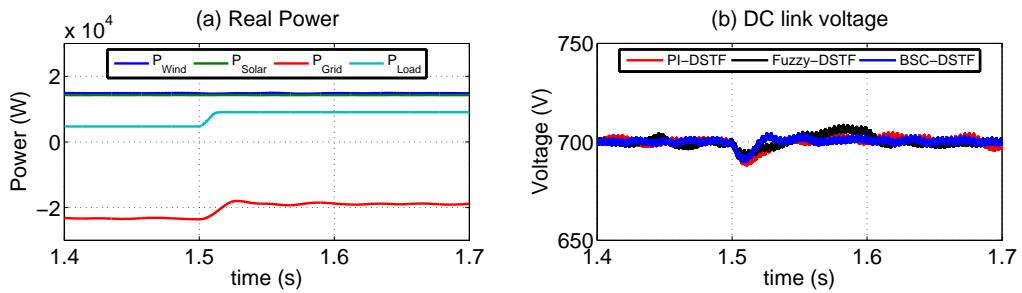
Figure 3.29: Power and DC-link voltage plots during during 50% step increment in load
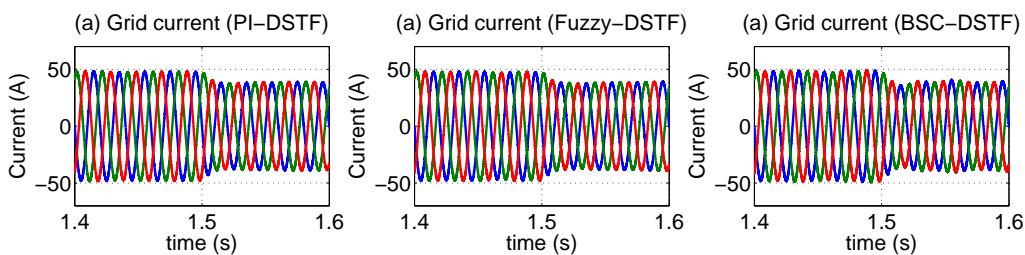
Figure 3.30: Grid current waveforms during during 50% step increment in load

The step change in wind speed from 12 to 10 m/s is simulated at 2 s. The real power and DC-link voltage in this condition are shown in Figure 3.31. The grid current waveforms are shown in Figure 3.32.
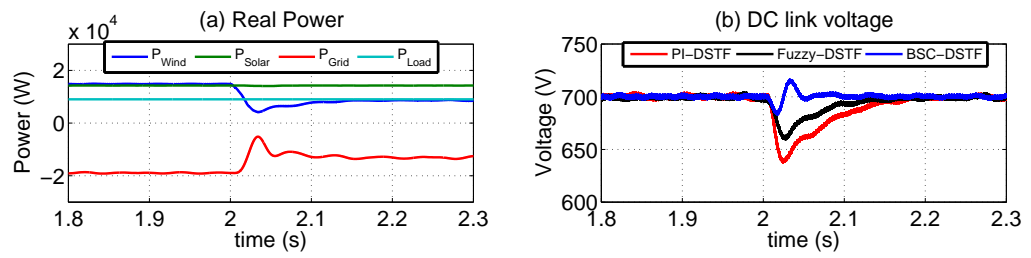
Figure 3.31: Power and DC-link voltage plots during step change in wind speed
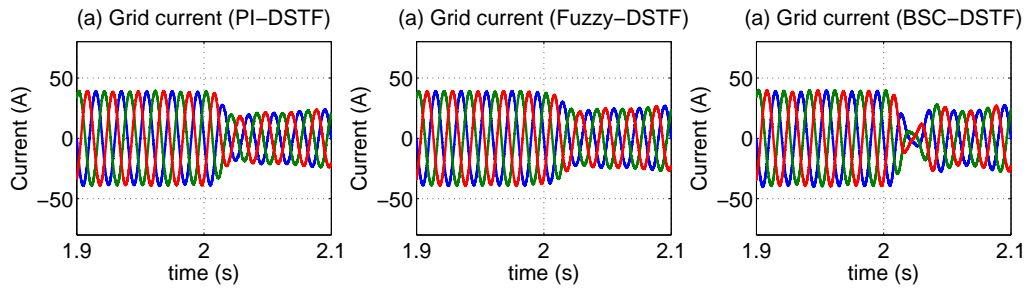
Figure 3.32: Grid current waveforms during step change in wind speed

A step decrement in the solar irradiation level from 1 to 0.8 kW/m^2 is simulated at 2.5 s. The real power and DC-link voltage in this condition are shown in Figure 3.33. The grid current waveforms are shown in Figure 3.34.
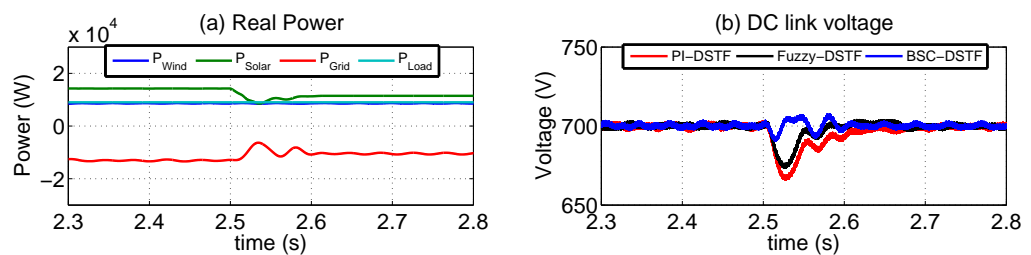
Figure 3.33: Power and DC-link voltage plots during step change in solar irradiation

61
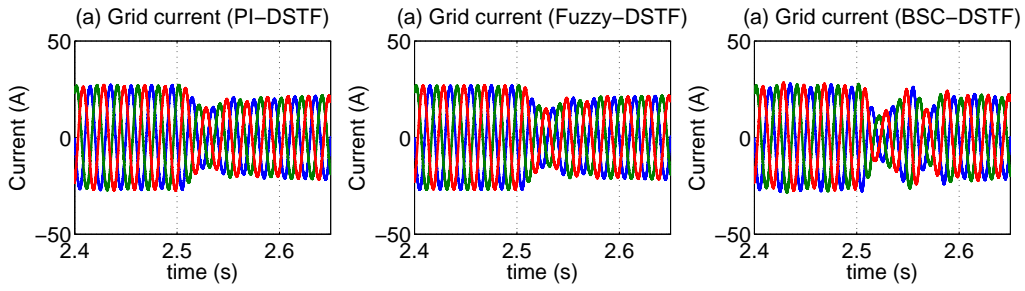
Figure 3.34: Grid current waveforms during step change in solar irradiation

The power generation from both wind and solar energy systems reduces to zero at 3 s. The real power and DC-link voltage in this condition are shown in Figure 3.35. The grid current waveforms are shown in Figure 3.36.
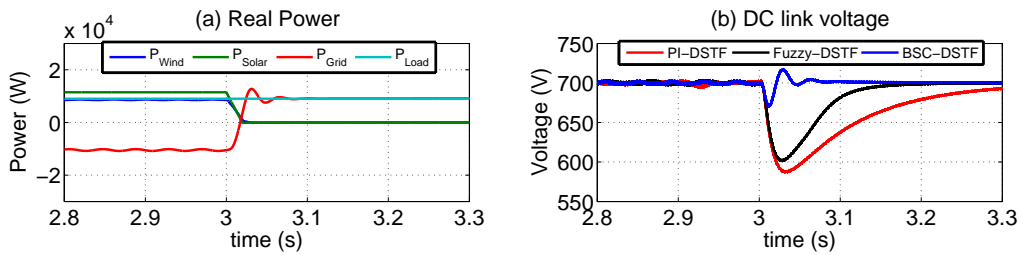
Figure 3.35: Power and DC-link voltage plots when renewable power generation reduces to zero
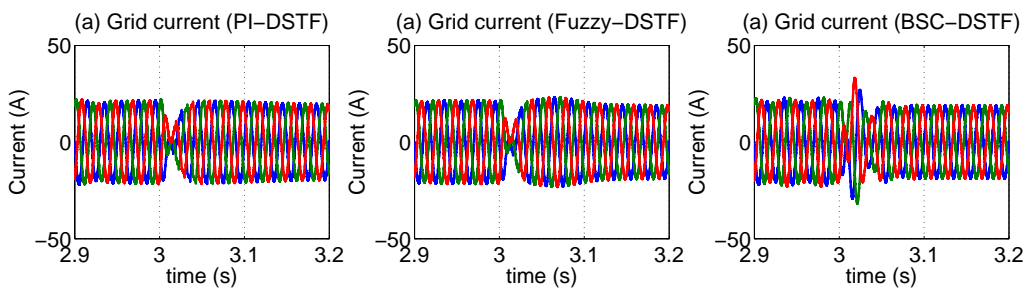
Figure 3.36: Grid current waveforms when renewable power generation reduces to zero

In the above discussed three cases, the integral square error and integral time square error are observed as minimum for BSC-DSTF-pq controller.

3.3.2.4 Step change in DC-link reference voltage

The DC-link voltage reference is changed from 700 V to 800 V at 1 s and changed back
to 700 V at 1.5 s. The real power and DC-link voltage waveforms during step increment
in reference voltage are shown in Figure 3.37. Corresponding grid current waveforms
are shown in Figure 3.38. The real power and DC-link voltage waveforms when DC-
link reference changes from 800 to 700 V is shown in Figure 3.39. Corresponding grid
current waveforms are shown in Figure 3.40.
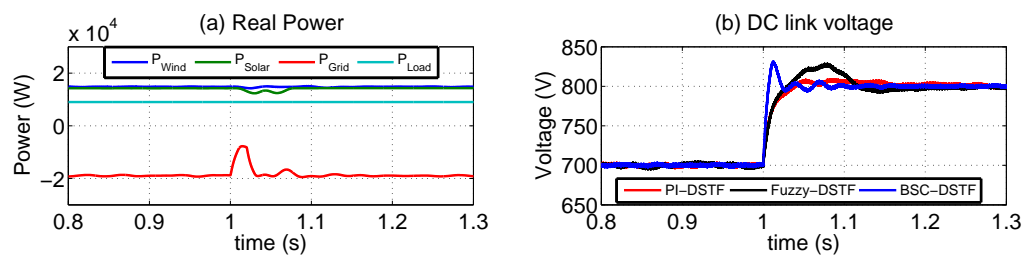
Figure 3.37: Power and DC-link voltage plots when DC-link reference changes from 700 to
800 V
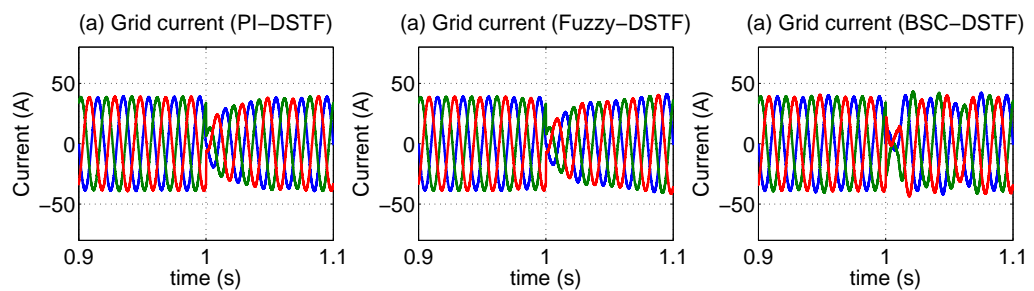
Figure 3.38: Grid current waveforms when DC-link reference changes from 700 to 800 V
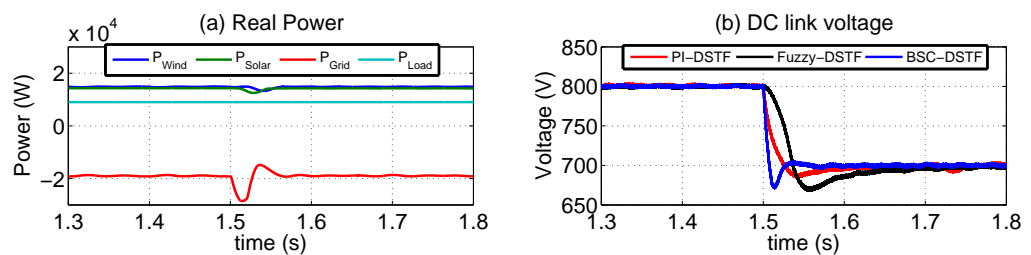
Figure 3.39: Power and DC-link voltage plots when DC-link reference changes from 800 to
700 V
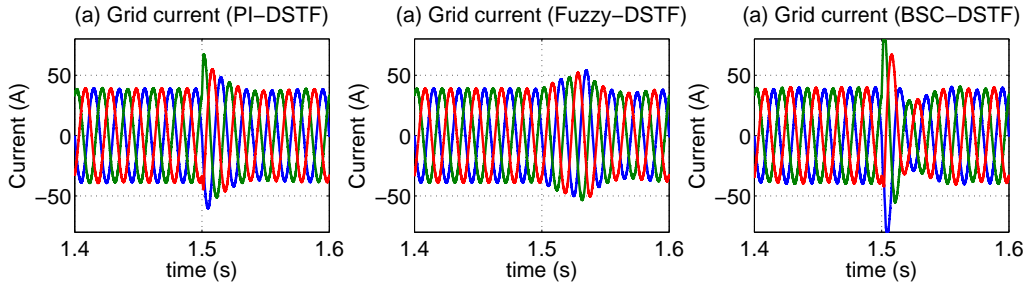
Figure 3.40: Grid current waveforms when DC-link reference changes from 800 to 700 V

For all the dynamic cases considered, the integral square error and integral time square error are minimum for BSC-DSTF-pq controller compared to PI-DSTF-pq and Fuzzy-DSTF-pq controllers. This implies lesser steady-state error and faster response for BSCDSTF-pq controller. This shows that the dynamic performance of BSC-DSTF-pq is superior compared to other controllers. The dynamic state results are summarized in table 3.5. It is observed that in all the cases, the integral square error and integral time square error are minimum for BSC-DSTF-pq controller.

Table 3.5: Summary of dynamic state results

Condition	Error parameter	Controller		
		PI-DSTF-pq	Fuzzy-DSTF-pq	BSC-DSTF-pq
Starting	ISE	0.0124	0.0121	0.0121
	ITSE	6.01×10^{-4}	3.45×10^{-4}	1.44×10^{-4}
50% decrease in load	ISE	5.13×10^{-6}	1.84×10^{-5}	2.55×10^{-6}
	ITSE	5.06×10^{-7}	1.02×10^{-6}	2.31×10^{-7}
50% increase in load	ISE	5.06×10^{-6}	5.20×10^{-6}	2.73×10^{-6}
	ITSE	4.65×10^{-7}	5.50×10^{-7}	2.50×10^{-7}
Change in wind speed from 12 to 10 m/s	ISE	2.87×10^{-4}	9.40×10^{-5}	1.00×10^{-5}
	ITSE	1.32×10^{-5}	4.08×10^{-6}	4.78×10^{-7}
Change in solar irradiation from 1 to 0.8 kW/m^2	ISE	6.65×10^{-5}	3.06×10^{-5}	4.42×10^{-6}
	ITSE	2.94×10^{-6}	1.23×10^{-6}	3.95×10^{-7}
Power generation from RES becomes zero	ISE	1.91×10^{-3}	8.77×10^{-4}	2.08×10^{-5}
	ITSE	1.30×10^{-4}	3.61×10^{-5}	4.25×10^{-7}
DC-link voltage reference changes from 700 to 800 V	ISE	9.66×10^{-5}	1.59×10^{-4}	4.90×10^{-5}
	ITSE	1.55×10^{-6}	5.90×10^{-6}	4.58×10^{-7}
DC-link voltage reference changes from 800 to 700 V	ISE	1.15×10^{-4}	4.61×10^{-4}	5.85×10^{-5}
	ITSE	1.96×10^{-6}	1.11×10^{-5}	5.08×10^{-7}

3.4 CONCLUSION

A dynamic model of wind-solar hybrid system has been simulated in MATLAB/ Simulink platform. The DC-link voltage loop of the controller has been designed using three different methods; using PI, Fuzzy and Back Stepping techniques. The proposed Back Stepping Controller has an additional switching loss estimator for effective loss compensation of the system. The harmonic compensator has been realized using DSTF-pq theory for enhanced performance compared to conventional LPF-pq theory. The stability analysis using Barbalat lemma has proved the wide-range stability of the system with BSC. From the simulation results, it has been observed that the current harmonics at the grid side has been compensated successfully. The THD of the grid current with PI-DSTF, Fuzzy-DSTF and BSC-DSTF controllers are found to be less than 5% for all steady-state conditions, which is well within limits specified by IEEE standard-519. It has been observed that the proposed BSC-DSTF is faster, more robust and offers better dynamic performance compared to PI-DSTF and Fuzzy-DSTF controllers under different dynamic conditions.

Chapter 4

Control System Design and Simulation of a Three-phase UPQC Interfacing Wind-Solar Hybrid System to the Distribution Grid

4.1 INTRODUCTION

Voltage sag, swell and voltage harmonic distortions are some of the major power quality problems in distribution system utilities which cannot be addressed by shunt active power filters (Edomah, 2009; Kumar et al., 2016). The equipment in modern industrial plants, like process controllers, programmable logic controllers, adjustable speed drives etc. are susceptible to these kinds of power quality issues. A combination of shunt and series active filters (Unified Power Quality Conditioner - UPQC) can mitigate the majority of power quality problems in the distribution level.

The control system of UPQC consists of series active filter controller and shunt active filter controller. The series active power filter controller mainly consists of a positive sequence fundamental voltage calculator, a voltage controller and a pulse generator. Conventionally positive fundamental voltages are calculated by using low pass

filters (Kanjiya et al., 2012). The low pass filter introduces an additional phase lag, and it affects the performance of the series active filter. This can be overcome by cascading a lag compensator circuit, which increases the complexity and cost of the overall control system (Kanjiya et al., 2012). A stable closed loop voltage controller is needed for effective control of output AC voltage of the voltage source inverter. Since the accurate modelling of dynamic states of the inverter is difficult, voltage controller design and tuning using conventional PI controllers is a complex task (Mohebbi et al., 2017; Yi et al., 2008). A Fuzzy controller based voltage controller can overcome this limitation.

In this chapter, a UPQC interfacing wind-solar hybrid system to the distribution grid is designed, simulated and analysed. A novel control strategy is proposed for the series active filter. It consists of a self-tuning filter (STF) based fundamental positive sequence detector and a Fuzzy logic based stable closed loop voltage controller. A PWM controller is used for generating switching pulses for controlling the series active filter inverter. The details of shunt active filter control system are discussed in 3.2.3.

In the first section, the power circuit of UPQC is discussed. The control schematic of UPQC and the design of its components are illustrated in the second section. In the third section, the simulation results for different system conditions are shown which verifies the effectiveness of the controller. The last section is the conclusion of the observations from the results.

4.2 POWER CIRCUIT OF UPQC

The shunt and series active filters are connected back to back with a common DC-link. The wind–solar hybrid renewable system is connected at the DC-link. The series active filter acts as a voltage regulator and a voltage harmonic isolator between grid and load centre by injecting compensating voltage, whereas shunt active filter balances the load and blocks the current harmonics to enter the grid by injecting compensating current. The dc-link voltage controller associated with shunt active filter controls the power flow from renewable energy to the grid. The overall schematic diagram of UPQC interfacing renewable systems to grid at the distribution level is shown in Figure 4.1. It

consists of two 3 phase, four leg IGBT inverters; VSI-1 for the series active filter, and VSI-2 for shunt active filter. It also consists of a DC-link capacitor, an inductive filter for shunt active filter, an LC filter for the series active filter, three single phase injection transformers with their primary windings connected to VSI-1 AC output terminals and secondary windings connected in series with the grid, and non-linear loads at PCC.
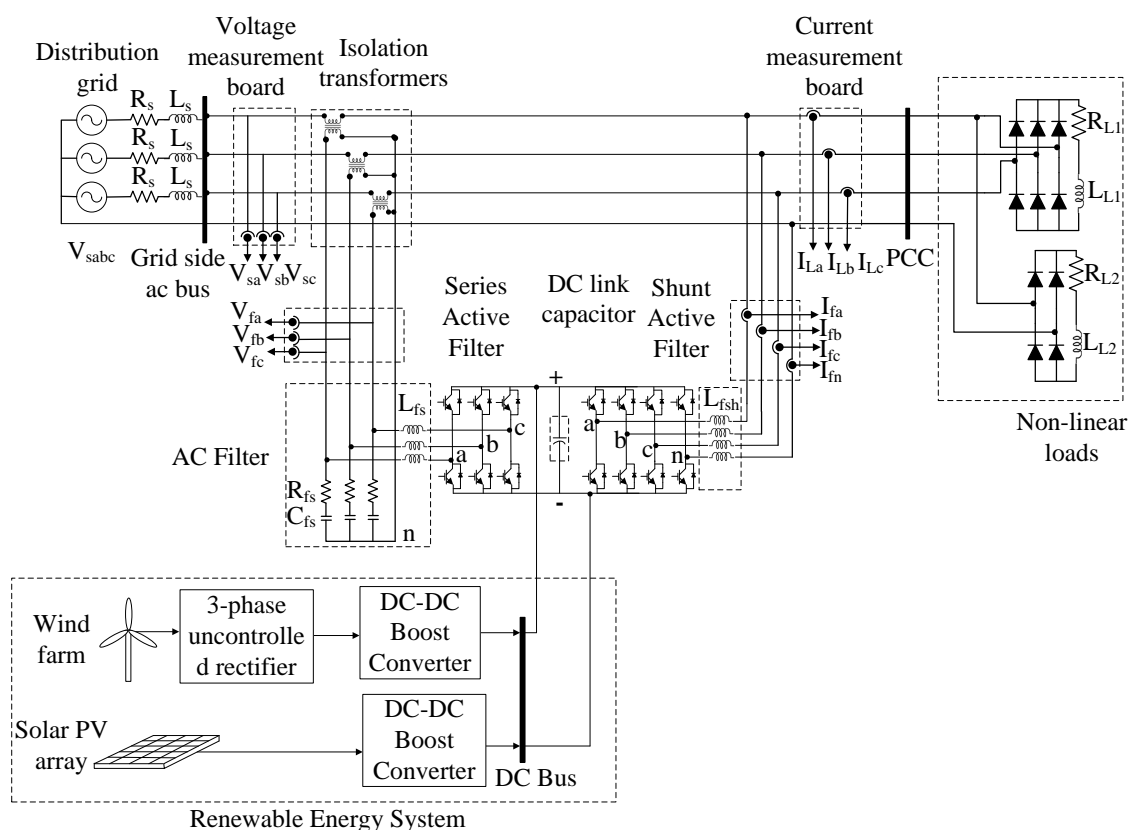
Figure 4.1: Schematic diagram of a UPQC interfacing renewable energy system to the grid, with non-linear load at load centre

4.3 CONTROL SYSTEM DESIGN OF UPQC

The block diagram representation of the overall control system is shown in Figure 4.2. It is a combination of control systems of a series active power filter and a shunt active power filter. Following subsections deals with the control system design in detail.

Figure 4.2: Control system of UPQC interfacing renewable energy systems to grid

4.3.1 Series active filter control system design

The basic principle of the series active filter is that it senses the changes in grid side voltage and injects compensation voltage in series with the grid voltage to nullify the change. The change can be a voltage sag, voltage swell or voltage distortion in grid voltage. The control scheme of the series active filter is shown in Figure 4.3.

Figure 4.3: Control system of the series active filter with non-linear load at load centre

The grid voltages are transformed into $\alpha\beta0$ frame using (4.1) to get $V_s^\alpha, V_s^\beta, V_s^0$.

$$
\begin{bmatrix} V_s^\alpha \\ V_s^\beta \\ V_s^0 \end{bmatrix} = \sqrt{\frac{2}{3}} \begin{bmatrix} 1 & -\frac{1}{2} & -\frac{1}{2} \\ 0 & \frac{\sqrt{3}}{2} & -\frac{\sqrt{3}}{2} \\ \frac{1}{\sqrt{2}} & \frac{1}{\sqrt{2}} & \frac{1}{\sqrt{2}} \end{bmatrix} \begin{bmatrix} V_s^a \\ V_s^b \\ V_s^c \end{bmatrix}
\tag{4.1}
$$

A self tuning filter (STF) is used for detecting the positive sequence fundamental component of grid voltage. $V_{s1}^\alpha, V_{s1}^\beta$ are the fundamental positive sequence components of grid voltage in $\alpha\beta0$ frame.

An abc to $\alpha\beta0$ transformation is done to convert fundamental positive sequence grid voltages to abc frame as shown in (4.2). A peak detector detects the peak amplitude of the grid voltages $V_{s1}^a, V_{s1}^b, V_{s1}^c$ in every half cycle of their fundamental frequency. The grid voltage is divided with the corresponding peak amplitude values to get three phase unit amplitude signals, U_a, U_b, U_c which are in phase with the grid voltages. The unit amplitude signals are multiplied by V_{Lp} to form the reference load voltage signals with required amplitude. The resultant voltage signals are then subtracted from grid voltages, to get the reference signals for the series active filter, V_{fref}^{abc}.

$$
\begin{bmatrix} V_{s1}^a \\ V_{s1}^b \\ V_{s1}^c \end{bmatrix} = \sqrt{\frac{2}{3}} \begin{bmatrix} 1 & 0 & \frac{1}{\sqrt{2}} \\ -\frac{1}{2} & \frac{\sqrt{3}}{2} & \frac{1}{\sqrt{2}} \\ -\frac{1}{2} & -\frac{\sqrt{3}}{2} & \frac{1}{\sqrt{2}} \end{bmatrix} \begin{bmatrix} V_{s1}^\alpha \\ V_{s1}^\beta \\ V_{s1}^0 \end{bmatrix}
\tag{4.2}
$$

The reference V_{fref}^{abc} are subtracted from the inverter output voltage V_f^{abc} and the error is processed using a Fuzzy logic based voltage controller. Five Fuzzy levels, BP (Big Positive), P (Positive), Z (Zero), N (Negative), and BN (Big Negative) are chosen for both the inputs, i.e.; error e and change in error de. Fuzzy rules are formed based on the facts listed below.

1. If the error is high, the controller output should also be high. Else if the error is small, the controller output should be small

2. If the error is positive and the change in error is also positive, the controller out-

71

put should be positive. Else if both error and change in error are negative, the controller output should be negative

3. If the error is a large positive value, and the change in error is a large negative value, controller output should be zero.

Fuzzy rule table is shown in Table 4.1. Figure 4.4 shows the normalized input and output membership functions. Fuzzification is done with triangular membership functions, and defuzzification using the centroid method. Inputs are multiplied with input gains for normalizing the inputs. The output of Fuzzy controller is multiplied with output gain.
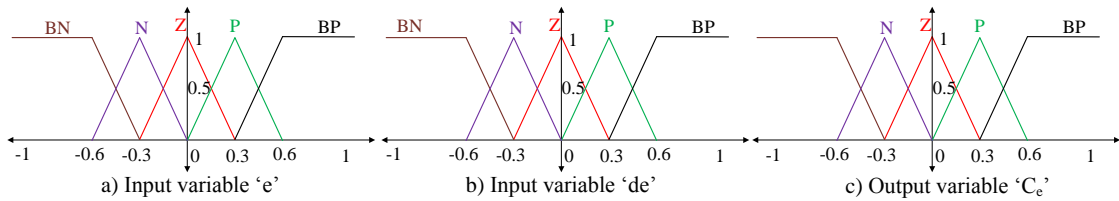
Figure 4.4: Normalized membership functions of a) Input variable 'e', b) input variable 'de' and c) Output variable 'C_{de}'

Table 4.1: FuzzyRule Table

de \ e	BN	N	Z	P	BP
BN	BN	BN	BN	N	Z
N	BN	BN	N	Z	P
Z	BN	N	Z	P	BP
P	N	Z	P	BP	BP
BP	Z	P	BP	BP	BP

The output of voltage controller is given to a PWM controller to generate switching pulses for the VSI.

4.3.2 Shunt active filter control system design

The DC-link voltage controller of SHAF is designed using Back Stepping Controller and the harmonic current mitigation by DSTF-pq control. The design of control system of SHAF is discussed in Chapter 3.

72

4.4 SIMULATION RESULTS AND ANALYSIS

Numerical simulations are carried out in MATLAB/Simulink environment for different system conditions to verify the effectiveness of the control system. System parameters are listed in Table 4.1. A three phase programmable voltage source is used as grid. Non-linear load is simulated using a three phase rectifier with an RL load at the DC side. A three phase IGBT inverter is simulated with capacitors at its DC-link. The wind-solar hybrid system is connected at the DC-link of the system. A three phase LC filter is connected at the AC side of the inverter. Single phase 1:1 transformers are used as isolation transformers. Primaries of transformers are connected in inverter output, and secondary of transformers are connected in series with the line connecting grid to the load. Different cases considered for simulation are discussed and corresponding results are shown in following section.

Table 4.2: UPQC parameters

Sl. No	Particulars	Values
1	Supply Voltage	3Φ, 400 V (Line–line, RMS), 50Hz
2	Source Parameters	0.01mH, 0.1 Ω
3	DC-link capacitance	2350 μF
4	DC-link voltage	700V
5	SHAF Filter Parameters	5mH, 0.1 Ω
6	SAPF Filter Parameters	0.1 Ω , 0.25 mH, 100 μF
6	Load parameters	Three-phase rectifier with 30 Ω, 48 mH load

4.4.1 Grid Voltage Sag

A single phase 40% sag in grid voltage is simulated from 0.5 to 0.6 s by reducing the voltage in A phase to 0.6 pu keeping the other phase voltages at 1 pu. Figure 4.5 shows the three-phase grid voltages, the compensation voltages injected in phase with the grid voltages to mitigate sag, the load voltages, load currents, the compensation currents injected by SHAF to mitigate current harmonics, and grid currents. It is observed from Figure 4.5 that the sag in phase A is compensated by SAPF within a cycle. Also, the harmonic components present in load current are compensated by SHAF. The

results are summarized in table 4.3.
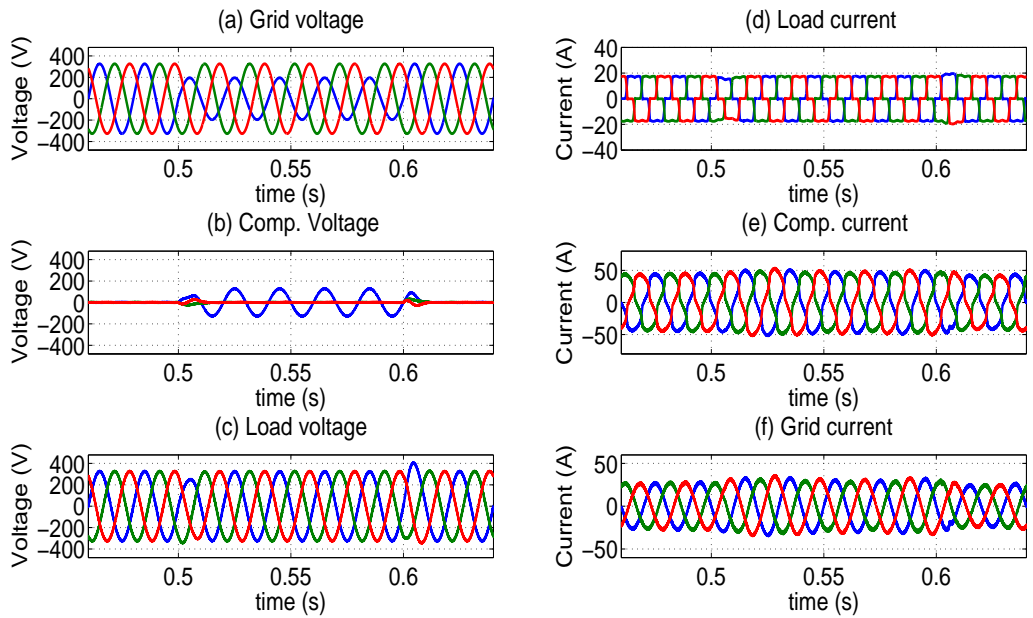
Figure 4.5: Simulation results: Single phase sag

Table 4.3: Summary of simulation results: Single phase grid voltage sag

Load voltages		Before	After	Grid currents		Before	After
RMS (V)	phase A	138.59	229.45	THD (%)	phase A	24.06	2.35
	phase B	230.94	229.88		phase B	24.03	3.41
	phase C	230.94	229.73		phase C	24.02	2.67

A three-phase 40% sag in grid voltage is simulated from 0.5 to 0.6 s by reducing the voltage in all three phase to 0.6 pu. Figure 4.6 shows the three phase grid voltages, the compensation voltages injected in phase with the grid voltages to mitigate sag, the load voltages, load currents, the compensation currents injected by SHAF to mitigate current harmonics, and grid currents. It is observed from Figure 4.6 that the sag in all phases are compensated by SAPF within a cycle. Also, the harmonic components present in load current are compensated by SHAF. The transient oscillations in the grid currents are due to the sudden disturbance created in the DC-link due to three phase sag in grid voltage. The DC-link voltage is regulated within two to three cycles by the Back Stepping algorithm based DC-link voltage controller. The results are summarized in table 4.4.
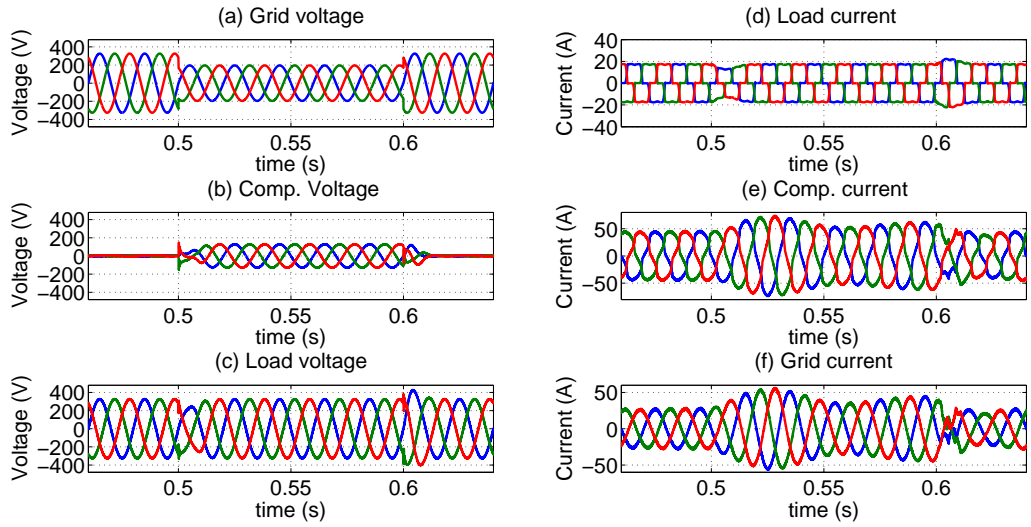
Figure 4.6: Simulation results: Three phase sag

Table 4.4: Summary of simulation results: Three phase grid voltage sag

Load voltages		Before	After	Grid currents		Before	After
RMS (V)	phase A	138.59	229.52	THD (%)	phase A	23.94	1.44
	phase B	138.59	229.52		phase B	23.95	1.87
	phase C	138.59	229.52		phase C	23.94	1.53

4.4.2 Grid Voltage Swell

A single phase 40% swell in grid voltage is simulated from 0.7 to 0.8 s by increasing the voltage in A phase to 1.4 pu keeping the other phase voltages at 1 pu. Figure 4.7 shows the three phase grid voltages, the compensation voltages injected in phase with the grid voltages to mitigate swell, the load voltages, load currents, the compensation currents injected by SHAF to mitigate current harmonics, and grid currents. It is observed from Figure 4.7 that the swell in phase A is compensated by SAPF within a cycle. Also, the harmonic components present in load current are compensated by SHAF. The results are summarized in table 4.5.

A three-phase 40% swell in grid voltage is simulated from 0.7 to 0.8 s by increasing the voltage in all three phases to 1.4 pu. Figure 4.8 shows the three phase grid voltages, the compensation voltages injected in phase with the grid voltages to

75
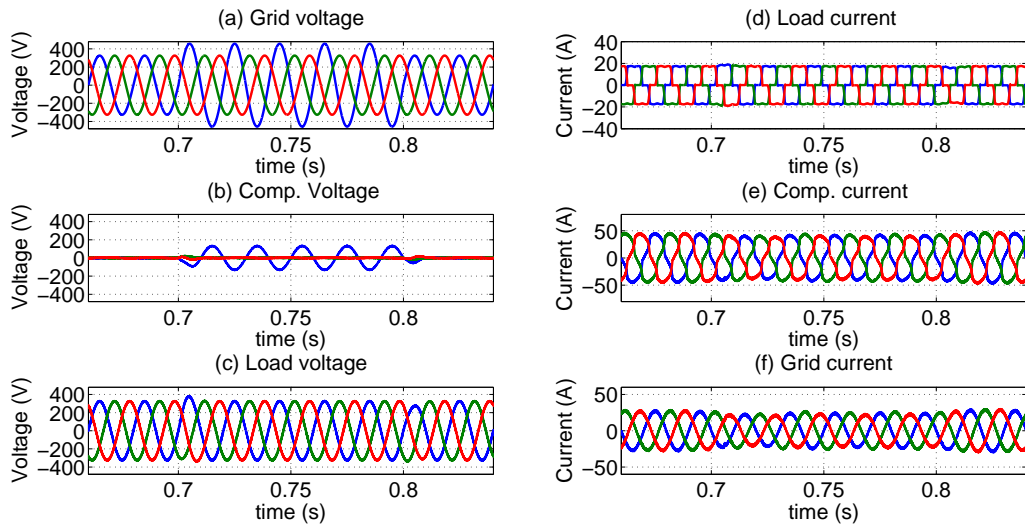
Figure 4.7: Simulation results: Single phase swell

Table 4.5: Summary of simulation results: Single phase grid voltage swell

Load voltages		Before	After	Grid currents		Before	After
	phase A	323.28	230.16		phase A	23.96	2.40
RMS (V)	phase B	230.94	229.73	THD (%)	phase B	23.92	2.50
	phase C	230.94	229.95		phase C	23.96	3.39

mitigate swell, the load voltages, load currents, the compensation currents injected by SHAF to mitigate current harmonics, and grid currents. It is observed from Figure 4.8 that the swell in phase A is compensated by SAPF within a cycle. Also, the harmonic components present in load current are compensated by SHAF. The power generated by renewable sources is utilized by the load and the remaining power is injected to the grid. During swell, the SAPF draws power from the grid, and hence the reduction in magnitude of grid currents. The results are summarized in table 4.6.

Table 4.6: Summary of simulation results: Three phase grid voltage swell

Load voltages		Before	After	Grid currents		Before	After
	phase A	323.28	230.09		phase A	23.94	1.36
RMS (V)	phase B	323.28	230.09	THD (%)	phase B	23.95	1.54
	phase C	323.28	230.09		phase C	23.95	1.58

76
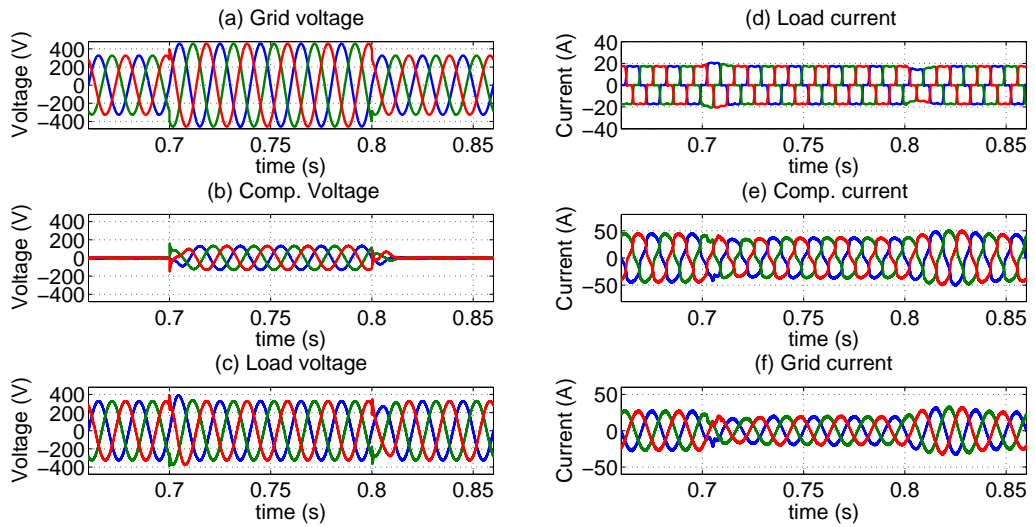
Figure 4.8: Simulation results: Three phase swell

4.4.3 Grid Voltage Distortion

A 10% distorted grid voltage condition is simulated by injecting 8% of 5th order voltage harmonic component and 6% of 7th order voltage harmonic component at grid.
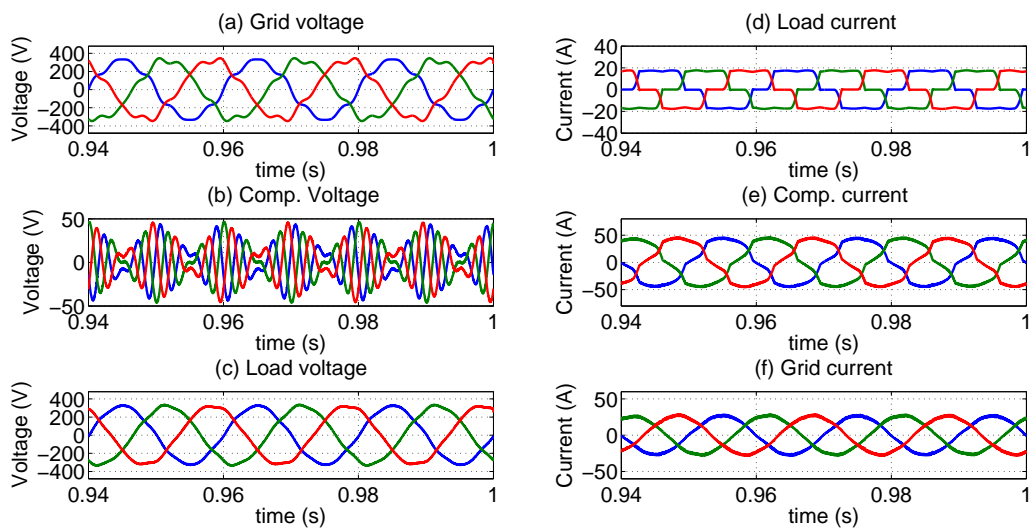
Figure 4.9: Simulation results: Grid voltage distortion

Figure 4.9 shows the three phase grid voltages, the injected voltages in phase with the grid voltages to compensate the harmonics, the load voltages, the load currents, the

compensation currents injected by SHAF to mitigate current harmonics, and the grid currents. The summary of results are shown in table 4.7.

Figure 4.10 shows harmonic spectrum of grid voltage, load current, load voltage and grid current for phase A respectively. It is observed that the load voltage harmonics and grid current harmonics are within the harmonic limits at distribution level.

(a) Grid Voltage harmonic spectrum

(b) Load Current harmonic spectrum

(c) Load Voltage harmonic spectrum

(d) Grid Current harmonic spectrum
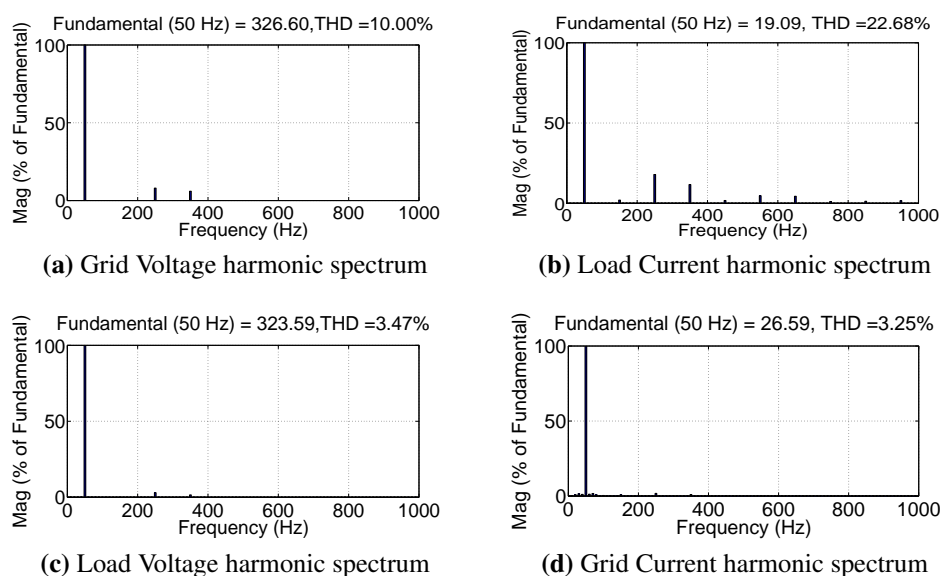
Figure 4.10: Harmonic analysis results of phase A under 10% distorted grid voltage condition

Table 4.7: Summary of simulation results: Grid voltage distortion

Load voltages		Before	After	Grid currents		Before	After
	phase A	10	3.37		phase A	22.58	3.70
THD (%)	phase B	10	3.38	THD (%)	phase B	23.29	3.51
	phase C	10	3.33		phase C	25.25	3.70

4.5 CONCLUSION

A unified shunt - series active filter interfacing renewable energy systems to the distribution grid has been designed and simulated. In the series active filter, the control system computes the compensation voltages using a self-tuning filter and a peak detection algorithm. The Fuzzy logic based closed loop voltage controller effectively controls the output AC voltage of the voltage source inverter in the series active filter.

A shunt active filter, connected back to back with the series active filter, consists of a Back Stepping Controller for DC-link voltage control and instantaneous active and reactive theory based current controller for harmonic mitigation. The simulation studies have been conducted for sag, swell and distorted grid voltage conditions. It has been observed that the shunt active filter effectively compensates the load current harmonics and maintains a constant DC-link voltage, and thereby balances the power flow in the system. Series active filter compensates the voltage sag/swell/distortions in grid voltage. The grid current THDs, load voltage THDs and load voltage RMS values are well within limits for all cases, as prescribed by IEEE - 519.

Chapter 5

Hardware Implementation of Single-phase SHAF with Backstepping-Dual STF-pq Controller

5.1 INTRODUCTION

The real-time implementation of control algorithms for SHAF is commonly achieved using digital signal processing (DSP) cards, microcontrollers, Field Programmable Gate Arrays (FPGA) etc. The inherently optimised RAM and parallel processing capability of FPGA offer reduced execution time and rapid prototyping compared to DSPs and microcontrollers. The hardware programmable arrays of logic elements and a large number of configurable inputs and outputs are the significant specialities of FPGA. The adaptability, higher accuracy, low design cost and high sampling period are the additional advantages of using FPGA (Charles and Vivekanandan, 2015).

This chapter deals with the hardware implementation of the laboratory prototype of single-phase SHAF. The FPGA implementation of the control algorithm proposed in 3.2.3 and the details of sensing and signal conditioning circuits are discussed in this chapter. The study and analysis of the hardware results are also presented.

5.2 IMPLEMENTATION OF HARDWARE SET-UP

The laboratory prototype of SHAF is implemented with the system parameters as given in Table 5.1. The IGBT inverter (SKM75GB12T4) with SKYPER 32R gate driver is used for realising shunt active filter. The specification of IGBT module used in the inverter is given in Appendix C. The block diagram of the overall experimental set-up is shown in Figure 5.1.
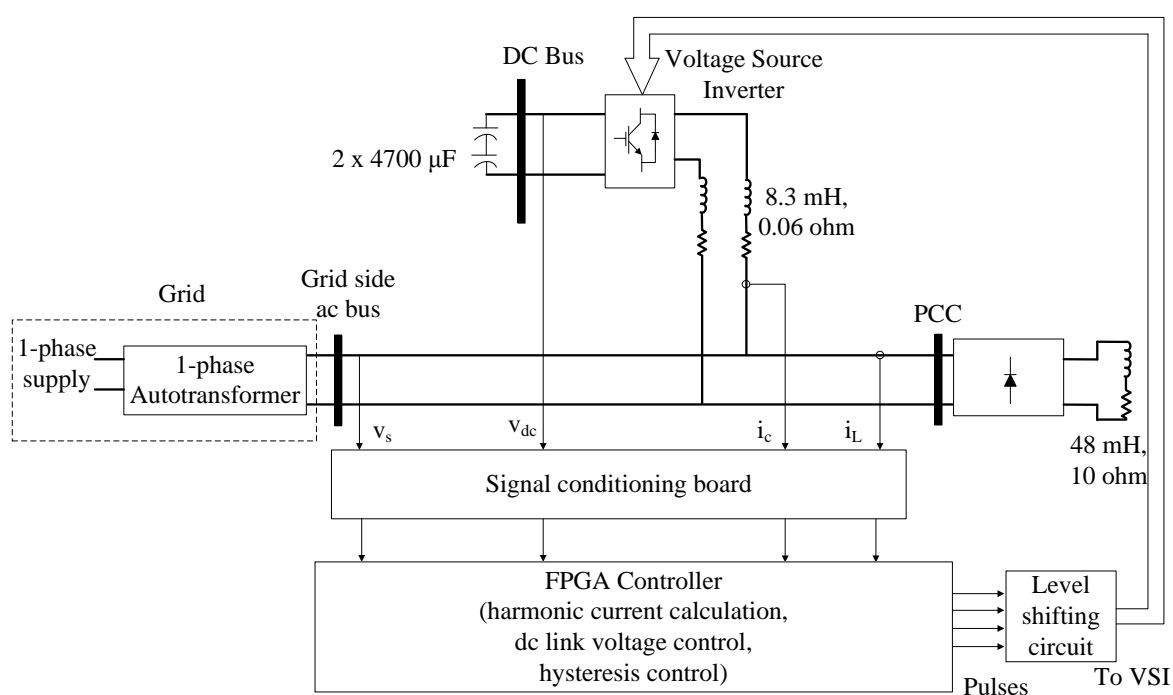
Figure 5.1: Block diagram of overall experimental set-up

The overall experimental set-up is shown in Figure 5.2. The proposed control algorithm is implemented in Xilinx (XC7a35t cpg236-1) FPGA.

Table 5.1: System Parameters

Sl. No	Particulars	Values
1	Supply Voltage	1Φ, 30 V (RMS), 50 Hz
2	Source Parameters	0.01 mH, 0.1 Ω
3	DC-link capacitance	2350 μF
4	DC-link voltage	50 V
5	Filter Parameters	8.3 mH, 0.06 Ω
6	Load parameters	A 1Φ H-bridge rectifier loaded with 10 Ω, 48 mH
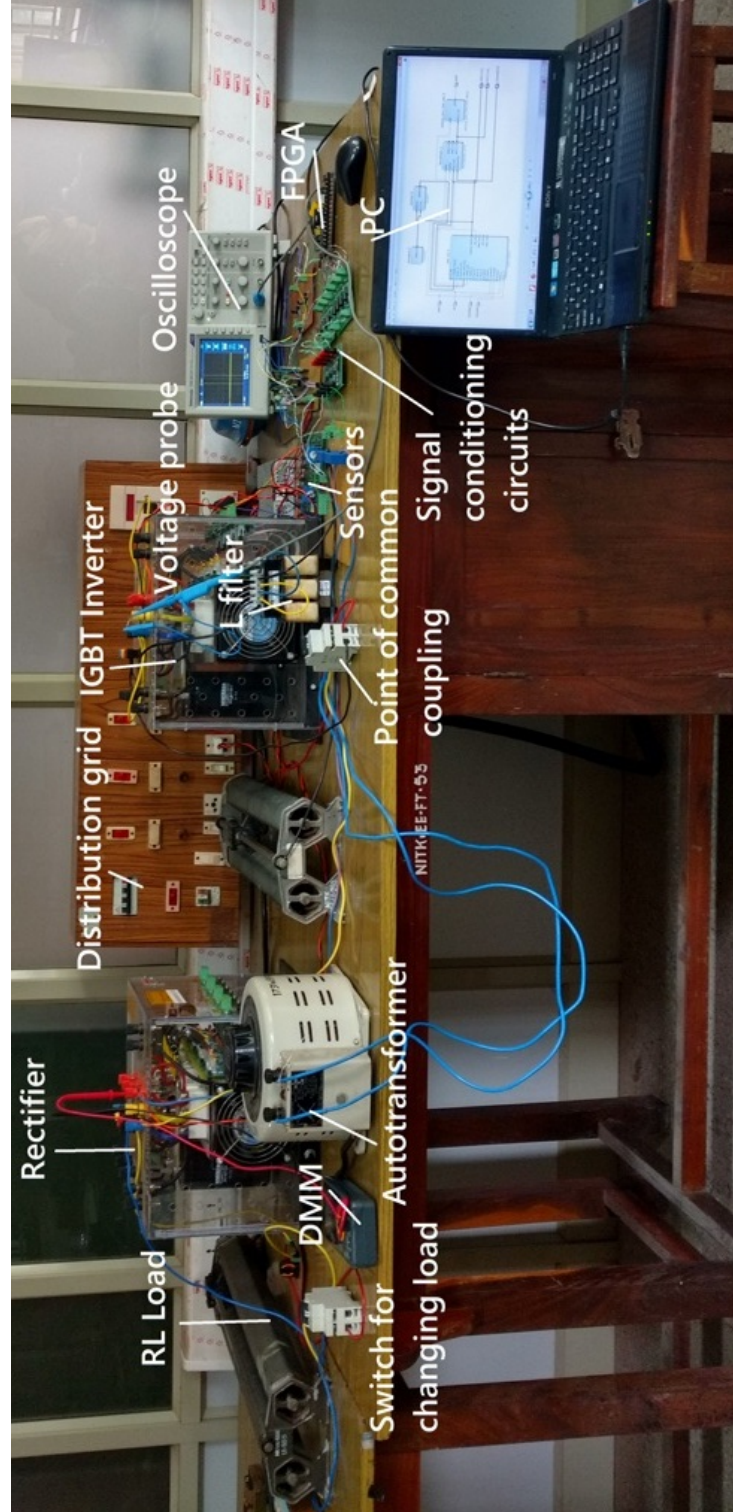
Figure 5.2: Laboratory prototype of single phase SHAF

5.2.1 Design and implementation of sensing and signal conditioning circuits

In order to establish a closed loop control, sensors are the primary block of the feedback. The voltage and current sensor signals need to be interfaced to the FPGA, which generates PWM pulses to control the inverter. This involves 3 steps :

- Sensing the signals with appropriate components and circuits.
- Conditioning the obtained signals to meet the specifications of the FPGA's ADC.
- Instantiating the FPGA to receive the converted signals from its ADC.

5.2.1.1   *Implementation of sensing and signal conditioning circuits*

The Hall effect sensors LEM LV-25p and LEM LA-55p are used for sensing voltage and current respectively. The specifications of the sensors used are shown in Appendix D. The current and voltage sensing circuits are shown in Figure 5.3a and 5.3b respectively.

The design equation of measuring resistance (R_M) is given by $R_{Mmax} = V_{ADC}/I_{Smax}$, where R_{Mmax} is the maximum value of measuring resistance, I_{Smax} is the maximum value of secondary current of the sensor, V_{ADC} is the input voltage range of Xilinx ADC; which is limited to 0.5 V in Xilinx ADC. For the target application, a current of the value of 10 A (peak) is necessary to be sensed. The conversion ratio of LA 55-P is 1: 1000. Hence, the value of the resistor R_M is chosen as 50 Ω. Similarly, 100 V (peak) voltage is necessary to be sensed using LV 25-P. The input resistance (R_1) is selected, in order to limit the primary current of LV 25-P to less than 10 mA. The values of R_1 and R_M are chosen as 60 kΩ and 100 Ω respectively.

The sensed signals are filtered and conditioned to match with the Xilinx ADC input specifications. An anti-aliasing filter is designed using four op amps using the precision op-amp package LT1014, for a cut-off frequency of 40 kHz. A differential amplifier is cascaded to this output to feed it to the ADC through the differential inputs. Since both the differential inputs of Xilinx ADC need to be positive signals, a DC-offset generator circuit is also incorporated. The overall signal conditioning circuit is shown

in Figure 5.3c.

The current sensor output waveform for an input current of 2.8 A is shown in Figure 5.4a. The voltage sensor output waveform for an input voltage of 63 V is shown in Figure 5.4b. Figure 5.5 shows the output waveforms of the signal conditioning circuit. The sensor output is filtered, converted to differential mode and clamped by +0.5 V.

5.2.2 FPGA based design of control algorithm

The implementation of the proposed algorithm in FPGA requires a well defined modular structure as shown in Figure 5.6. The system is divided into different modules. These modules are implemented using MATLAB and Xilinx system generator.

5.2.2.1 Analog to digital conversion module

The Xilinx Basys3 FPGA contains two onboard 12-bit bipolar ADCs with a sampling rate of 1 MSPS. Total four auxiliary analog signals can be connected to the ADC with an input signal range of $\pm$ 0.5 V. Maximum DC offset allowed is 0.5 V. The ADC is configured for 4 auxiliary input signals with a sampling rate of approximately 250 kilo samples per second for each signal. The voltage and current sensor outputs signals are filtered and signal conditioned using analog electronic circuits and given to analog input channel of the ADC. Detailed specifications of Xilinx Basys3 FPGA is given in Appendix E.

5.2.2.2 Decode XADC module

The 12 bit ADC output signals are obtained as 16-bit time multiplexed digital outputs. Decode XADC module slices the most significant 12 bits from the ADC output and stores the digital data of each channel in corresponding registers.

Figure 5.3: Sensing and signal conditioning circuits
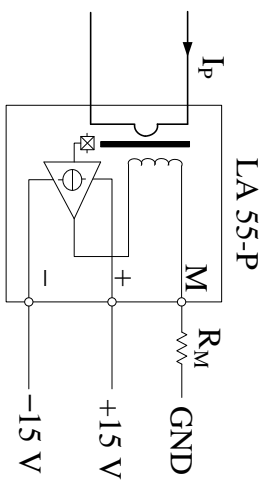
(a) Current sensing circuit using LEM LA 55-P Current Transducer
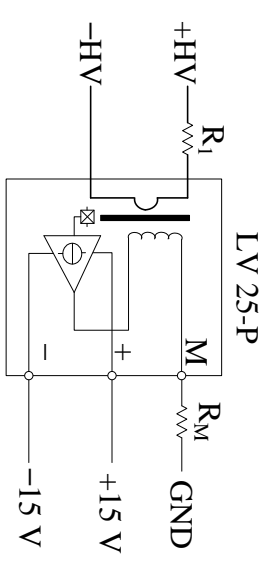
(b) Voltage sensing circuit using LV25-P Voltage Transducer

(c) Signal conditioning circuit
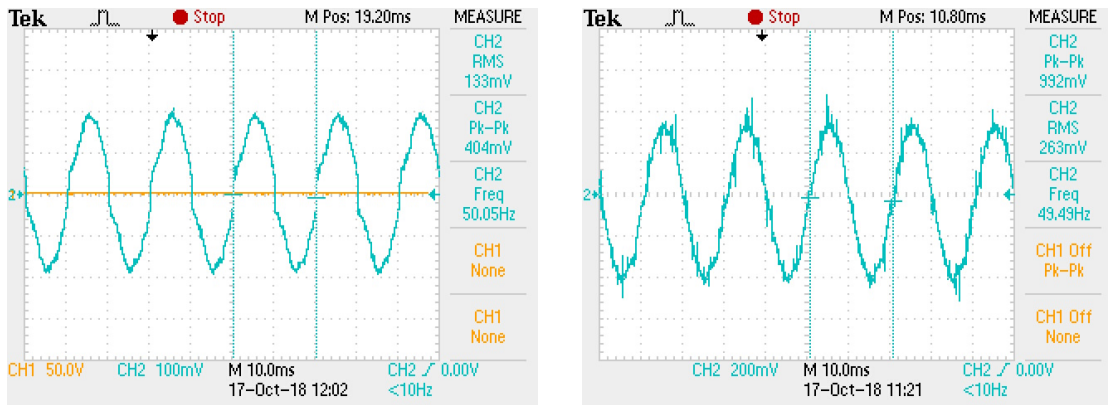
(a) Current sensor output waveform for an input current of 2.8 A

(b) Voltage sensor output waveform for an input voltage of 63 V

Figure 5.4: Output waveforms of sensor circuits
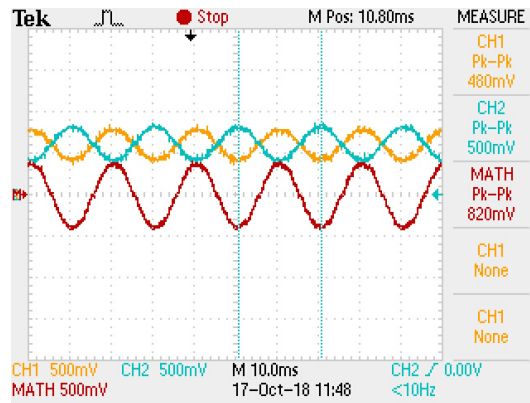
Figure 5.5: Output waveforms of signal conditioning circuit

5.2.2.3   Shunt active filter control module

Different control blocks like STF, instantaneous power calculation, reference current calculation, Back Stepping controller, and the hysteresis controller are implemented using system generator blocks. IP cores are generated for synthesising the algorithms in Xilinx Vivado design suite. Finally the design synthesis, implementation and bitstream generation are done using Xilinx Vivado design suite software.

5.2.3   Implementation of Opto-coupler based level shifting circuit

The pulses generated by the FPGA based control system are at 3.3 V however, the voltage to trigger IGBT switches are 15.0 V. An optocoupler based level shifting
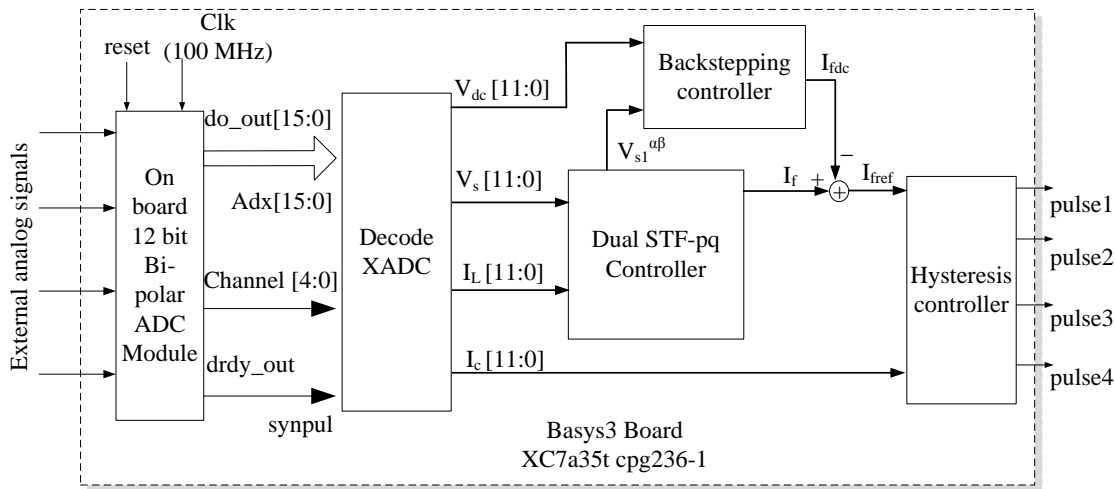
Figure 5.6: Modular Design of FPGA Controller

circuit shown in Figure 5.7a is used for level shifting the pulses from 3.3 V to 15.0 V. This circuit separates the power circuit and control circuit using optical isolation. The circuit also creates a dead band of 2 μs. The input and output waveforms of the level shifting circuit are shown in Figure 5.7b.

(a) Optocoupler based level shifting circuit

(b) Input and output waveforms of level shifting circuit
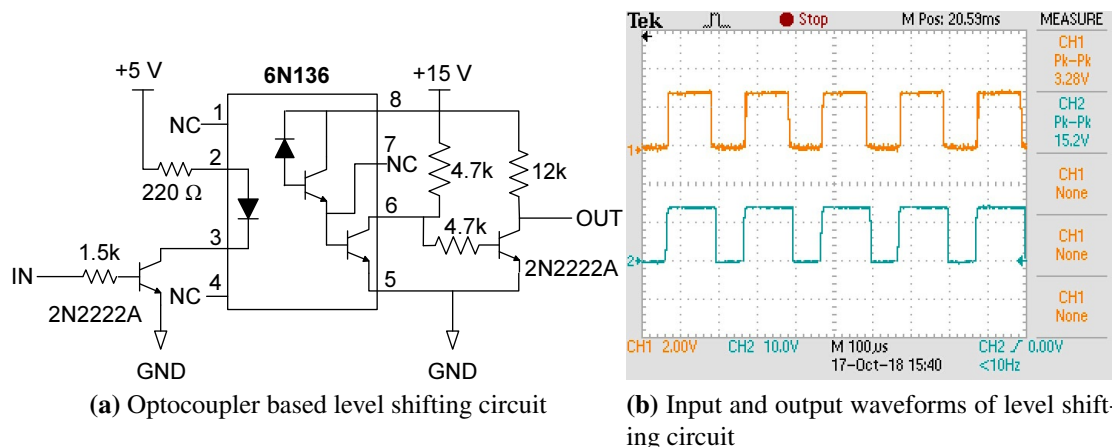
Figure 5.7: Level shifting circuit and corresponding waveforms

5.3 RESULTS AND DISCUSSION

The laboratory prototype of single-phase SHAF with BSC-DSTF-pq controller is tested under steady state and Dynamic conditions. The parameters of BSC are tuned by trial and error method. The value of 'c' and 'γ' are varied to get a fast and accurate

88

control response. The value of 'c' determines how fast the DC-voltage error approaches zero, and the value of 'γ' determines how accurately the switching loss is being estimated. The inequality $c > 2\sqrt{\gamma}$ is considered while tuning the parameters for assuring stability. The tuned values are c = 200, γ = 2500. The performance of BSC is compared with a PI controller. The K_p and K_i values of PI controller are tuned by using Ziegler-Nicholas method. The system transfer function used for the PI controller tuning is shown in (5.1), where I_{co} is the rated compensation current, V_s is the RMS value of grid voltage, R_c, L_c are the resistance and inductance of filter inductor respectively, and V_{dco} is the rated DC-link voltage.

$$\frac{V_{dc}(s)}{V_{dcref}(s)} = (K_p + \frac{K_i}{s})(\frac{V_s - 2I_{co}R_c - I_{co}L_cs}{V_sC_{dc}V_{dco}s}) \tag{5.1}$$

For a fair comparison, the PI controller parameters are tuned so as to get the best possible response under nominal steady-state condition. The tuned values of K_p and K_i are 5 and 0.001 respectively. Following sections deal with the discussion on the results.

5.3.1 Steady state condition

The performance of the proposed BSC-DSTF controller under steady state is compared with two other controllers;

- PI-LPF-pq (PI for DC-link voltage control and LPF based pq theory for current harmonic compensation)

- PI-DSTF-pq (PI for DC-link voltage control and DSTF based pq theory for current harmonic compensation)

The steady-state results of SHAF with PI-LPF-pq, PI-DSTF-pq and BSC-DSTF-pq controllers are shown in Figure 5.8. Figure 5.9 shows the frequency spectrum of grid voltage, load current and grid current with PI-LPF-pq, PI-DSTF-pq and BSC-DSTF-pq.
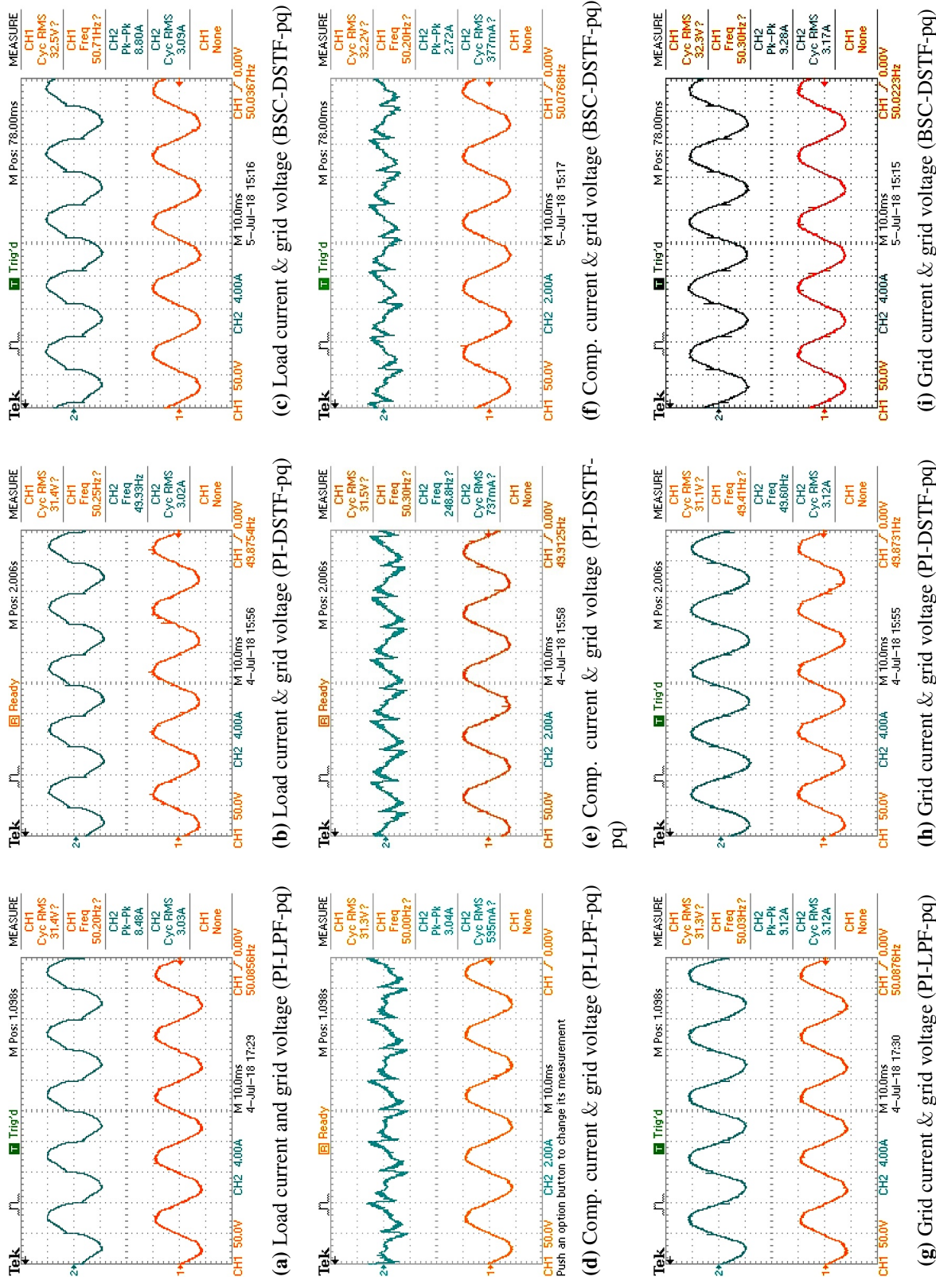
Figure 5.8: Steady state results under distorted grid voltage with LPF-pq and DSTF-pq controllers

(a) Load current and grid voltage (PI-LPF-pq)

(b) Load current & grid voltage (PI-DSTF-pq)

(c) Load current & grid voltage (BSC-DSTF-pq)

(d) Comp. current & grid voltage (PI-LPF-pq)

(e) Comp. current & grid voltage (PI-DSTF-pq)

(f) Comp. current & grid voltage (BSC-DSTF-pq)

(g) Grid current & grid voltage (PI-LPF-pq)

(h) Grid current & grid voltage (PI-DSTF-pq)

(i) Grid current & grid voltage (BSC-DSTF-pq)

90
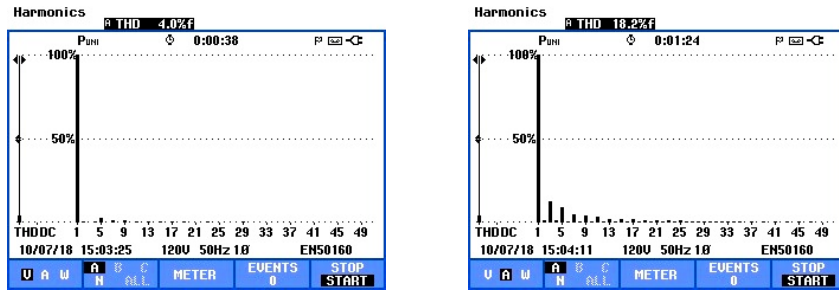
(a) Grid voltage   (b) Load current
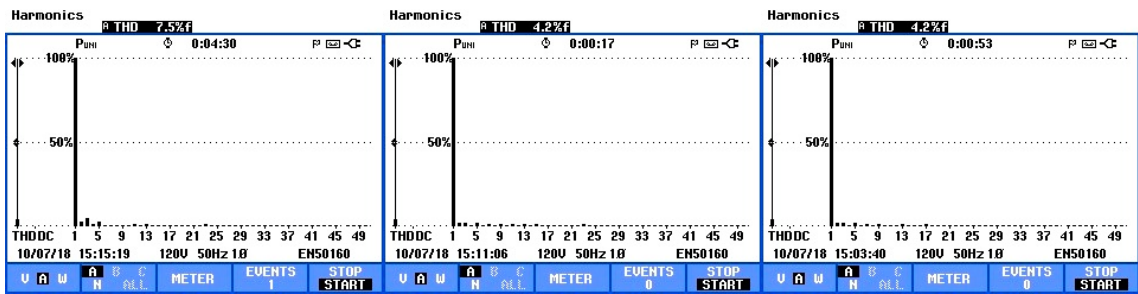
(c) Grid current(LPF-pq)   (d) Grid current(DSTF-pq)   (e) Grid current (BSC-DSTF-pq)

Figure 5.9: Harmonic analysis results with LPF-pq and DSTF-pq controllers

The grid current THD with PI-LPF-pq, PI-DSTF-pq and BSC-DSTF-pq are observed as 7.5%, 4.2% and 4.2% respectively. The grid current THDs for PI-DSTF-pq and BSC-DSTF-pq are within the limits specified by IEEE-519.

The DC-link voltage waveforms with PI and BSC are shown in Figure 5.10. The PI and BSC controllers show a similar response in the nominal steady-state condition. The peak to peak DC-link voltage ripple values are observed as similar for both the controllers.
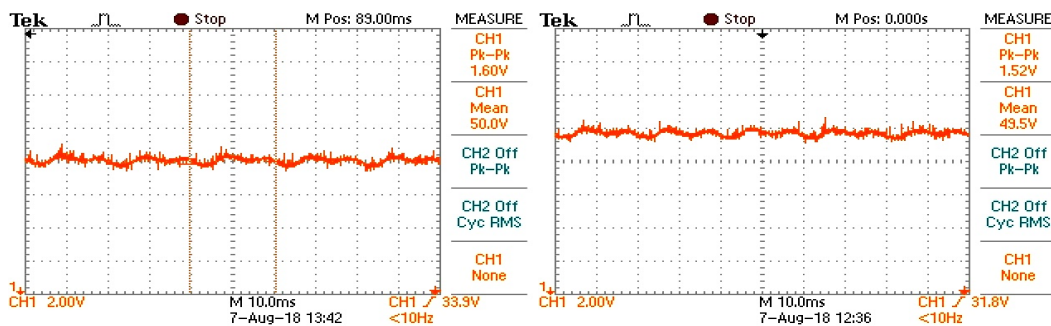
(a) DC-link voltage (PI)   (b) DC-link voltage (BSC)

Figure 5.10: Steady state DC-link voltage waveforms with PI and BSC controllers

91

5.3.2 Dynamic state condition

Different test conditions for dynamic state are;

- Starting

- 50% step change in load

- Change in reference value of DC-link voltage

The performance of the BSC-DSTF-pq controller is compared with PI-DSTF-pq controller, under each of these conditions.

5.3.2.1 *Starting*

Figure 5.11 shows the dynamic DC-link and grid current waveforms with PI and BSC during initial start-up. A 5 Ω resistor is included in series with the inductor filter during starting up to limit the huge inrush current. The resistor is removed once the DC-link voltage reaches its steady state value, by closing the switch connected across it. The settling times for PI and BSC are observed as 116 ms and 68 ms respectively.
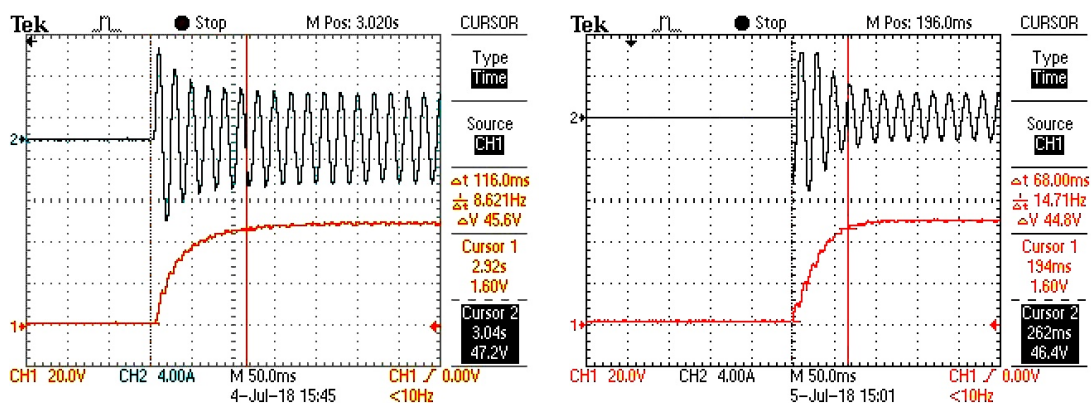
(a) Grid current and DC-link voltage with PI-DSTF-pq theory controller

(b) Grid current and DC-link voltage with BSC-DSTF-pq theory controller

Figure 5.11: Dynamic condition results: Starting

5.3.2.2   50% step decrement in load

The transients during 50% step decrement in load is shown in Figure 5.12. The settling times for PI and BSC are 66 ms and 42 ms respectively.

(a) Grid current and DC-link voltage with PI-DSTF-pq theory controller

(b) Grid current and DC-link voltage with BSC-DSTF-pq theory controller
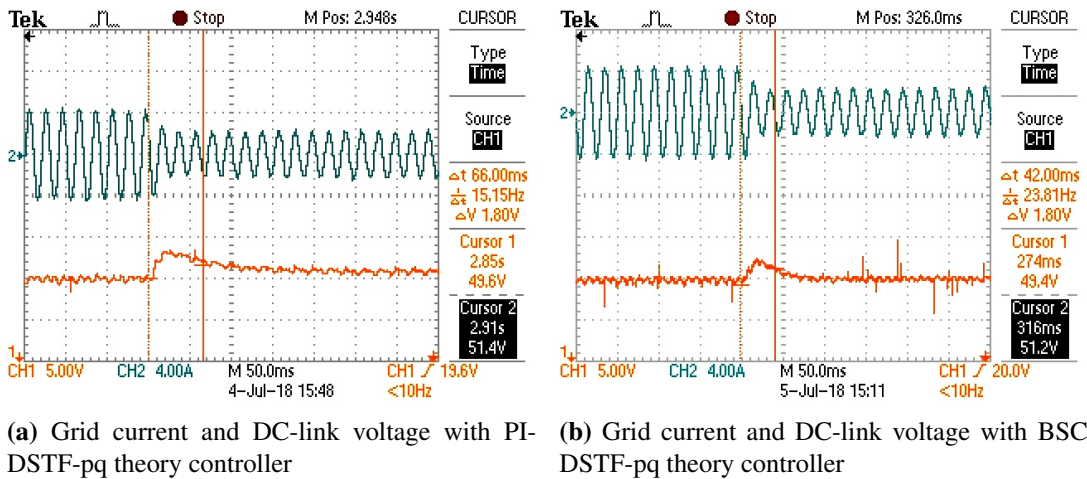
Figure 5.12: Dynamic condition results: Load is decreased by 50%

The load is step incremented by 50% and the corresponding waveforms are shown in Figure 5.13. The settling times after the load increment are 56 ms and 36 ms respectively.

(a) Grid current and DC-link voltage with PI-DSTF-pq theory controller

(b) Grid current and DC-link voltage with BSC-DSTF-pq theory controller
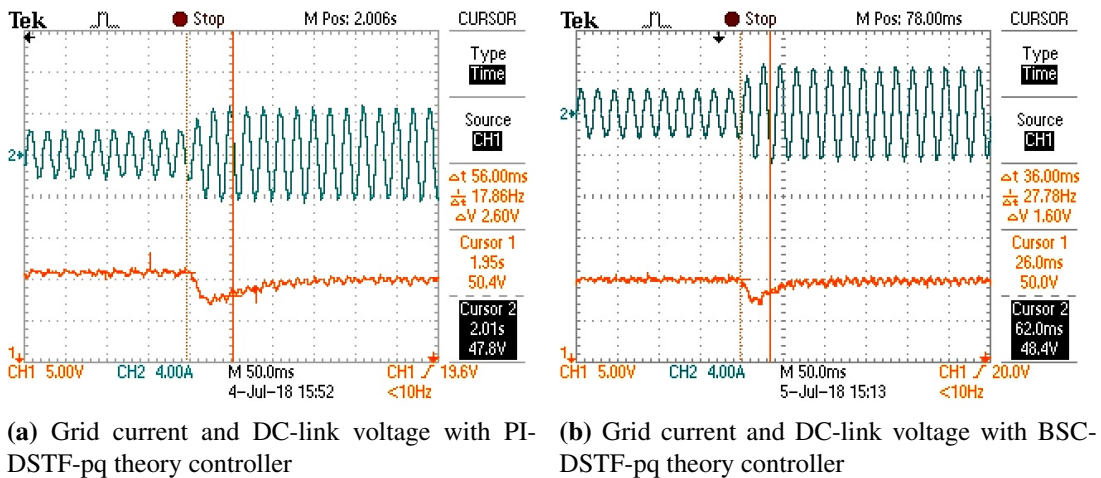
Figure 5.13: Dynamic condition results: Load is increased by 50%

93

5.3.2.3   Change in reference value of DC-link voltage

The DC-link voltage reference is changed from 50 V to 60 V and the performance of the system with PI and BSC are analysed. The results are shown in Figure 5.14. The settling times are 78 ms and 37 ms for PI and BSC respectively. The DC-link voltage reference is changed back to 50 V and the results during this transition are shown in Figure 5.15. The settling times for PI and BSC for this condition are 82 ms and 37 ms respectively.

(a) Grid current and DC-link voltage with PI-DSTF-pq theory controller

(b) Grid current and DC-link voltage with BSC-DSTF-pq theory controller
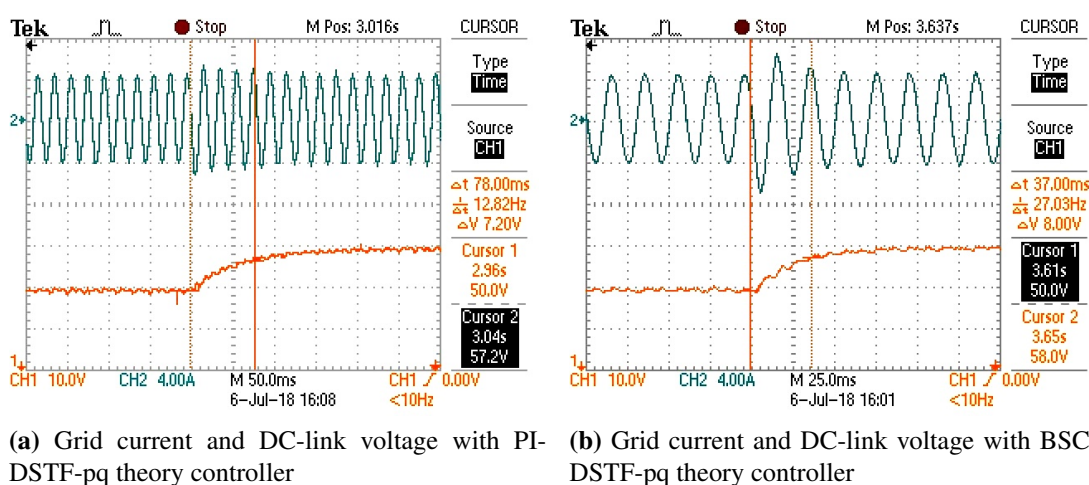
Figure 5.14: Dynamic condition results: DC-link voltage reference is changed from 50 to 60 V

(a) Grid current and DC-link voltage with PI-DSTF-pq theory controller

(b) Grid current and DC-link voltage with BSC-DSTF-pq theory controller
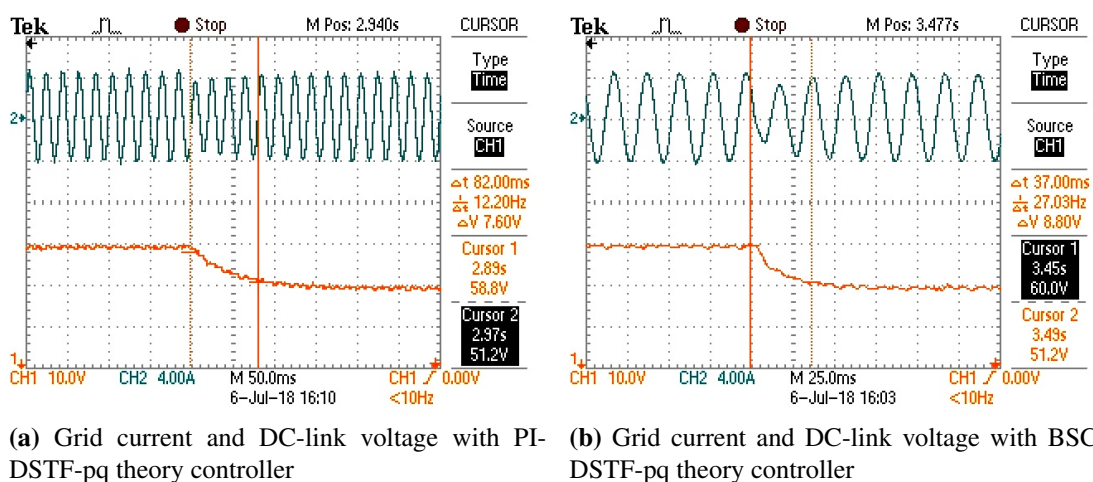
Figure 5.15: Dynamic condition results: DC-link voltage reference is changed from 60 to 50 V

The dynamic results from the hardware experiments are summarized in Table 5.2. It is observed that under all dynamic test cases, BSC-DSTF-pq controller has less settling time compared to PI-DSTF-pq controller.

Table 5.2: Comparison of DC Voltage Controllers under Dynamic Conditions

Sl. No.	Case	Settling time (ms)	
		PI with DSTF-pq	BSC with DSTF-pq
1	Starting	116	68
2	50% Load decrement	66	42
3	50% Load is increment	56	36
4	Change in V_{dcref} from 50-60 V	78	37
5	Change in V_{dcref} from 60-50 V	82	37

5.4 CONCLUSION

An adaptive, non-linear, robust DC-link voltage controller and an enhanced current harmonic compensator for a single-phase SHAF have been designed and implemented in FPGA. A Back Stepping Controller has been used for DC-link voltage control, with an additional switching loss estimator for effective loss compensation of the system. The harmonic compensator has been realized using DSTF-pq theory for enhanced performance compared to conventional LPF-pq theory. From the hardware results, it has been observed that the proposed BSC-DSTF-pq controller is faster, more robust and offers better dynamic performance compared to the PI-DSTF-pq controller under different dynamic conditions. The steady-state performances of both the controllers are observed as similar. The current harmonics at the grid side has been compensated successfully. The THD of the grid current is found to be 4.2%, which is less than 5%, well within limits specified by IEEE standard-519.

Chapter 6

Conclusion and Recommendations for Future Work

6.1 INTRODUCTION

In this chapter, the key points made in this thesis are summarised in chronological order. The discussion on the results with reference to the active filter interfacing hybrid wind-solar hybrid system is presented. This is followed by the major contributions of this thesis and the scope of future work.

6.2 KEY POINTS MADE IN THE THESIS

In chapter 1, different topologies of wind and solar systems are reviewed. The grid interconnection schemes of hybrid wind-solar systems, major power quality issues, the international power quality standards and the mitigation techniques are also discussed. The recent developments in shunt and series active filter control are reviewed. The major challenges associated with employing active filters for interfacing hybrid renewable system to the distribution grid are also reviewed. The summary of the work and the contents of chapters that follow are presented.

Chapter 2 discussed the modelling of the wind energy system and solar energy system. The design of different power circuit components involved is also discussed.

This includes boost converter design, the switching device selection for the inverter, the DC-link capacitor design and the filter inverter design.

Chapter 3 presented the design of the control system for a three-phase shunt active power filter interfacing wind-solar hybrid system to the grid. A dynamic model of the wind-solar hybrid system is simulated in MATLAB/ Simulink platform. A robust DC-link voltage controller for the system, using the Back Stepping technique is presented. The proposed Back Stepping Controller consists of an additional switching loss estimator for the effective loss compensation of the system. The realization of harmonic compensator using DSTF-pq theory is also discussed. The stability analysis using Barbalat lemma is presented, which proves the wide-range stability of the system with BSC. The simulation results showed that the THD of the grid current with PI-DSTF, Fuzzy-DSTF and BSC-DSTF controllers are less than 5% for all steady-state conditions, which is well within limits specified by IEEE standard-519. It is concluded that the proposed BSC-DSTF is faster, more robust and offers better dynamic performance compared to PI-DSTF and Fuzzy-DSTF controllers under different dynamic conditions.

In Chapter 4, a unified shunt - series active filter interfacing renewable energy systems to the distribution grid are designed and simulated. A series active filter, in which the control system computes the compensation voltages using a self-tuning filter and a peak detection algorithm is presented. A Fuzzy logic based closed loop voltage controller, which effectively controls the output AC voltage of the voltage source inverter in the series active filter is proposed. A shunt active filter, connected back to back with the series active filter, with a Back Stepping Controller for DC-link voltage control and instantaneous active and reactive theory based current controller for harmonic mitigation is considered for the simulation. From the simulation studies conducted for sag, swell and distorted grid voltage conditions, it is observed that the shunt active filter effectively compensates the load current harmonics and maintains a constant DC-link voltage, and thereby balances the power flow in the system. Series active filter compensates the voltage sag/ swell / distortions in grid voltage. The grid current THDs, load voltage THDs and load voltage RMS values are well within limits for all cases, as prescribed by IEEE

98

- 519.

Chapter 5 presented the design and FPGA implementation of an adaptive, non-linear, robust DC-link voltage controller and an enhanced current harmonic compensator for a single-phase SHAF. The SHAF with a Back Stepping Controller with an additional switching loss estimator for the DC-link voltage control and DSTF-pq theory for the harmonic compensator is implemented. The hardware results showed that the proposed BSC-DSTF-pq controller is faster, more robust and offers better dynamic performance compared to the PI-DSTF-pq controller under different dynamic conditions. The steady-state performances of both the controllers are observed as similar. The THD of the grid current is found to be less than 5%, well within limits specified by IEEE standard-519.

In brief, the research work presented in this thesis is an effort to improve the control performance of the shunt active filter interfacing hybrid wind-solar system to the distribution grid. The following points highlight the significant contributions of the thesis.

6.3 MAJOR CONTRIBUTIONS

- Development of the dynamic model for the representation of a variable speed wind turbine driven by PMSG connected to a DC bus by means of a DC-DC boost converter with MPPT feature.
- Development of the dynamic model for the representation of a solar PV array connected to a DC bus using a DC-DC boost converter with MPPT feature.
- Development of a dynamic model for the representation of a hybrid wind-solar system connected to the distribution grid through a three-phase four leg VSI.
- Implementation of the robust Backstepping algorithm based control scheme for effectively regulating the DC-link voltage for varying input conditions and varying load conditions and thereby regulating the power flow into the grid. Employment of current harmonics mitigation control scheme, based on Dual-STF-pq theory and thereby assigning additional current harmonics filtering feature to the

99

VSI.

- Studies on the response of the controller under different steady-state and dynamic conditions. The steady-state studies are conducted at balanced, unbalanced and distorted grid voltage conditions with constant input power and constant non-linear load conditions. The dynamic studies are conducted for step variations of wind speed, solar irradiation, load and DC-link voltage reference.

- Comparison of the proposed Backstepping based DC-link voltage control scheme with the existing control techniques such as PI and Fuzzy under different steady-state and dynamic conditions. The comparison of the proposed harmonic current mitigation technique using Dual-STF-pq theory with the conventional LPF-pq theory under different steady state conditions.

- Implementation of a control scheme based on peak detection algorithm, STF and the Fuzzy controller for mitigating voltage sag, swell and distortions at PCC.

- Implementation of a control scheme for the unified shunt-series active power filter (UPQC) interfacing hybrid wind-solar system to the distribution grid.

- Studies on the performance of the controller of the UPQC interfacing hybrid wind-solar hybrid system to the distribution grid, under different grid disturbances such as sag, swell and distortions with constant input power and constant non-linear loads at PCC.

- Development of laboratory prototype of a single-phase shunt active power filter and the implementation of the proposed BSC-DSTF-pq control scheme using FPGA.

- Study and analysis of the performance of the controller implemented in FPGA, under different steady-state and dynamic conditions using the experimental set-up.

6.4 SCOPE FOR FUTURE WORK

A laboratory prototype of a single-phase shunt active power filter with BSC-DSTF-pq control scheme is implemented. Other robust DC-link voltage controllers and current harmonic mitigation techniques can be implemented and tested on the lab-

oratory prototype. The work can be extended to a three-phase, four leg system. The wind and solar systems can be emulated and integrated into the system to analyse the effectiveness of the controller under input power variations. A prototype of a series active power filter can be developed and integrated with the system to develop a prototype of UPQC interfacing wind-solar hybrid system to the grid.

References

Akagi, H. (2005). The state-of-the-art of active filters for power conditioning. In *Power Electronics and Applications, 2005 European Conference on*, pages 1–15.

Akagi, H., Watanabe, E., and Aredes, M. (2017). *Shunt Active Filters*, chapter 4, pages 111–236. Wiley-Blackwell.

Ali, S., Chauhan, Y. K., and Kumar, B. (2013). Study amp;amp; performance of dvr for voltage quality enhancement. In *2013 International Conference on Energy Efficient Technologies for Sustainability*, pages 983–988.

Anderson, P. M. and Bose, A. (1983). Stability simulation of wind turbine systems. *IEEE Transactions on Power Apparatus and Systems*, PAS-102(12):3791–3795.

Asadi, M., Ebrahimirad, H., Mousavi, M. S., and Jalilian, A. (2016). Sliding mode control of dc-link capacitors voltages of a npc 4-wire shunt active power filter with selective harmonic extraction method. In *2016 7th Power Electronics and Drive Systems Technologies Conference (PEDSTC)*, pages 273–278.

Bagheri, A., Mardaneh, M., Rajaei, A., and Rahideh, A. (2016). Detection of grid voltage fundamental and harmonic components using kalman filter and generalized averaging method. *IEEE Transactions on Power Electronics*, 31(2):1064–1073.

Benchouia, M., Ghadbane, I., Golea, A., Srairi, K., and Benbouzid, M. E. H. (2015). Implementation of adaptive fuzzy logic and pi controllers to regulate the dc bus voltage of shunt active power filter. *Applied soft computing*, 28:125–131.

Biricik, S., Redif, S., Khadem, S. K., and Basu, M. (2016). Improved harmonic suppres-

sion efficiency of single-phase apfs in distorted distribution systems. *International Journal of Electronics*, 103(2):232–246.

Biricik, S., Redif, S., Ozerdem, . C., Khadem, S. K., and Basu, M. (2014). Real-time control of shunt active power filter under distorted grid voltage and unbalanced load condition using self-tuning filter. *IET Power Electronics*, 7(7):1895–1905.

Blaabjerg, F., Iov, F., Teodorescu, R., and Chen, Z. (2006). Power electronics in renewable energy systems. In *2006 12th International Power Electronics and Motion Control Conference*, pages 1–17.

Boehringer, A. F. (1968). Self-adapting dc converter for solar spacecraft power supply. *IEEE Transactions on Aerospace and Electronic Systems*, AES-4(1):102–111.

Carrasco, J. M., Franquelo, L. G., Bialasiewicz, J. T., Galvan, E., PortilloGuisado, R. C., Prats, M. A. M., Leon, J. I., and Moreno-Alfonso, N. (2006). Power-electronic systems for the grid integration of renewable energy sources: A survey. *IEEE Transactions on Industrial Electronics*, 53(4):1002–1016.

Charles, S. and Vivekanandan, C. (2015). An efficient fpga based real-time implementation shunt active power filter for current harmonic elimination and reactive power compensation. *Journal of Electrical Engineering and Technology*, 4(4).

Chen, B., Pin, G., Ng, W. M., Parisini, T., and Hui, S. Y. R. (2017). A fast-convergent modulation integral observer for online detection of the fundamental and harmonics in grid-connected power electronics systems. *IEEE Transactions on Power Electronics*, 32(4):2596–2607.

Chen, S. and Joos, G. (2001). Rating issues of unified power quality conditioners for load bus voltage control in distribution systems. In *2001 IEEE Power Engineering Society Winter Meeting. Conference Proceedings (Cat. No.01CH37194)*, volume 2, pages 944–949.

Chen, Y., Zha, X., Wang, J., Liu, H., Sun, J., and Tang, H. (2000). Unified power quality conditioner (upqc): the theory, modeling and application. In *PowerCon*

2000. 2000 International Conference on Power System Technology. Proceedings (Cat. No.00EX409), volume 3, pages 1329–1333.

Chen, Y.-M., Cheng, C.-S., and Wu, H.-C. (2006). Grid-connected hybrid pv/wind power generation system with improved dc bus voltage regulation strategy. In *Twenty-First Annual IEEE Applied Power Electronics Conference and Exposition, 2006. APEC '06.*, pages 7 pp.–.

Czarkowski, D. (2011). 13 -dcdc converters. In Rashid, M. H., editor, *Power Electronics Handbook (Third Edition)*, pages 1193 – 1228. Butterworth-Heinemann, Boston, third edition edition.

Davari, M., Aleemran, S. M., Nafisi, H., Salabeigi, I., and Gharehpetian, G. B. (2009). Modeling the combination of upqc and photovoltaic arrays with multi-input single-output dc-dc converter. In *2009 IEEE International Conference on Industrial Technology*, pages 1–6.

Demirdelen, T., Kayaalp, R. I., and Tmay, M. (2016). Pso-pi based dc link voltage control technique for shunt hybrid active power filter. In *2016 International Conference on Systems Informatics, Modelling and Simulation (SIMS)*, pages 97–102.

Devassy, S. and Singh, B. (2018). Design and performance analysis of three-phase solar pv integrated upqc. *IEEE Transactions on Industry Applications*, 54(1):73–81.

Ding, F., Li, P., Huang, B., Gao, F., Ding, C., and Wang, C. (2010). Modeling and simulation of grid-connected hybrid photovoltaic/battery distributed generation system. In *CICED 2010 Proceedings*, pages 1–10.

Edomah, N. (2009). Effects of voltage sags, swell and other disturbances on electrical equipment and their economic implications. In *CIRED 2009 - 20th International Conference and Exhibition on Electricity Distribution - Part 1*, pages 1–4.

El-Gammal, M., Abou-Ghazala, A., and El-Shennawy, T. (2011). Fifteen years of the dynamic voltage restorer: A literature review. *Australian Journal of Electrical and Electronics Engineering*, 8(3):279–287.

Escobar, G., Mattavelli, P., and Martinez-Montejano, M. F. (2009). Modifications to repetitive-based controllers using fir filters for practical implementation. In *2009 35th Annual Conference of IEEE Industrial Electronics*, pages 3246–3251.

Ezoji, H., Taheri, A., Saki, M., Sheikholeslami, A., and samani, A. G. (2012). Dynamic voltage restorer using sliding mode control to improve power quality in distribution system. In *2012 11th International Conference on Environment and Electrical Engineering*, pages 947–951.

Fitzer, C., Barnes, M., and Green, P. (2002). Voltage sag detection technique for a dynamic voltage restorer. In *Conference Record of the 2002 IEEE Industry Applications Conference. 37th IAS Annual Meeting (Cat. No.02CH37344)*, volume 2, pages 917–924 vol.2.

Fujita, H. and Akagi, H. (1998). The unified power quality conditioner: the integration of series and shunt-active filters. *IEEE Transactions on Power Electronics*, 13(2):315–322.

Ghamri, A., Mahni, T., Benchouia, M., Srairi, K., and Golea, A. (2015). Comparative study between different controllers used in three-phase four-wire shunt active filter. *Energy Procedia*, 74:807–816.

Gow, J. A. and Manning, C. D. (1996). Development of a model for photovoltaic arrays suitable for use in simulation studies of solar energy conversion systems. In *1996 Sixth International Conference on Power Electronics and Variable Speed Drives (Conf. Publ. No. 429)*, pages 69–74.

Hajizadeh, A. and Golkar, M. A. (2007). Intelligent power management strategy of hybrid distributed generation system. *International Journal of Electrical Power & Energy Systems*, 29(10):783 – 795.

Halpin, S. M. and Card, A. (2011). 40 - power quality. In Rashid, M. H., editor, *Power Electronics Handbook (Third Edition)*, pages 1179 – 1192. Butterworth-Heinemann, Boston, third edition edition.

Han, B., Bae, B., Kim, H., and Baek, S. (2006). Combined operation of unified power-

quality conditioner with distributed generation. *IEEE Transactions on Power Delivery*, 21(1):330–338.

Hoon, Y., Mohd Radzi, M. A., Hassan, M. K., and Mailah, N. F. (2017). A refined self-tuning filter-based instantaneous power theory algorithm for indirect current controlled three-level inverter-based shunt active power filters under non-sinusoidal source voltage conditions. *Energies*, 10(3).

IEEE-1159 (2009). IEEE recommended practice for monitoring electric power quality. *IEEE Std 1159-2009 (Revision of IEEE Std 1159-1995)*, pages c1–81.

IEEE-519 (2014). IEEE recommended practice and requirements for harmonic control in electric power systems. *IEEE Std 519-2014 (Revision of IEEE Std 519-1992)*, pages 1–29.

Jean-Jacques Slotine, W. L. (1991). Advanced stability theory. In *Applied Nonlinear Control*, pages 100 – 154. Prentice Hall, Englewood Cliffs, New Jersey 07632.

Jindal, A. K., Ghosh, A., and Joshi, A. (2007). Interline unified power quality conditioner. *IEEE Transactions on Power Delivery*, 22(1):364–372.

Joos, G. (1999). Three-phase static series voltage regulator control algorithms for dynamic sag compensation. In *Industrial Electronics, 1999. ISIE '99. Proceedings of the IEEE International Symposium on*, volume 2, pages 515–520.

Joos, G., Chen, S., and Lopes, L. (2004). Closed-loop state variable control of dynamic voltage restorers with fast compensation characteristics. In *Conference Record of the 2004 IEEE Industry Applications Conference, 2004. 39th IAS Annual Meeting.*, volume 4, pages 2252–2258.

Kanjiya, P., Khadkikar, V., Zeineldin, H. H., and Singh, B. (2012). Reactive power estimation based control of self supported dynamic voltage restorer (dvr). In *2012 IEEE 15th International Conference on Harmonics and Quality of Power*, pages 785–790.

Karuppanan, P. (2012). *Design and Implementation of Shunt Active Power Line Con-*

ditioner using Novel Control Strategies. PhD thesis, Department of Electronics and Communication Engineering, National Institute of Technology, Rourkela, India.

Kesler, M. and Ozdemir, E. (2010). A novel control method for unified power quality conditioner (upqc) under non-ideal mains voltage and unbalanced load conditions. In *2010 Twenty-Fifth Annual IEEE Applied Power Electronics Conference and Exposition (APEC)*, pages 374–379.

Khadkikar, V. (2012). Enhancing electric power quality using upqc: A comprehensive overview. *IEEE Transactions on Power Electronics*, 27(5):2284–2297.

Khadkikar, V. and Chandra, A. (2009). A novel structure for three-phase four-wire distribution system utilizing unified power quality conditioner (upqc). *IEEE Transactions on Industry Applications*, 45(5):1897–1902.

Khadkikar, V. and Chandra, A. (2011). Upqc-s: A novel concept of simultaneous voltage sag/swell and load reactive power compensations utilizing series inverter of upqc. *IEEE Transactions on Power Electronics*, 26(9):2414–2425.

Khadkikar, V., Chandra, A., and Singh, B. (2011). Digital signal processor implementation and performance evaluation of split capacitor, four-leg and three h-bridge-based three-phase four-wire shunt active filters. *IET Power Electronics*, 4(4):463–470.

Krithiga, S. and Ammasai Gounden, N. (2014). An improved power electronic controller with unity power factor for a single-stage grid-tied pv system. *Arabian Journal for Science and Engineering*, 39(10):7173–7182.

Kumar, A., Pal, N. S., and Ansari, M. A. (2016). Mitigation of voltage sag/swell and harmonics using self-supported dvr. In *2016 IEEE 1st International Conference on Power Electronics, Intelligent Control and Energy Systems (ICPEICES)*, pages 1–5.

Lada, M. Y., Zolkifri, N. I., Gani, J. A. M., Nawawi, M. R. M., and Kim, G. C. (2016). Reduction of harmonic using single phase shunt active filter based on fft method for cascaded multilevel inverter. In *4th IET Clean Energy and Technology Conference (CEAT 2016)*, pages 1–5.

Li, P., Bai, Q., and Li, G. (2006). Coordinated control strategy for upqc and its verification. In *2006 IEEE Power Engineering Society General Meeting*, pages 1–8.

Liang, X. (2017). Emerging power quality challenges due to integration of renewable energy sources. *IEEE Transactions on Industry Applications*, 53(2):855–866.

Ma, S., Wilkinson, A. J., and Paulson, K. S. (2010). A phase modulation-based ultrasonic communication system using variable structure control. In *2010 IEEE 12th International Conference on Communication Technology*, pages 857–860.

Mahfouz, A., Zaid, S., Saad, S., and Hagras, A. (2015). Sensorless dc voltage control with backstepping design scheme for shunt active power filter. *Journal of Electrical Engineering*, 15:303–312.

Malla, S. G., Deepu, D. J., Kumar, D. P., and Malla, J. M. R. (2016). Solar powered mobile phone: An innovative experiment. In *2016 International Conference on Signal Processing, Communication, Power and Embedded System (SCOPES)*, pages 1015–1020.

Melin, P. E., Espinoza, J. R., Munoz, J. A., Baier, C. R., and Espinosa, E. E. (2010). Decoupled control of a unified power quality conditioner based on a current source topology for fast ac mains disturbance compensation. In *2010 IEEE International Conference on Industrial Technology*, pages 730–736.

Mikkili, S. and Padamati, A. (2017). PHC,id-iq and p-q control strategies for mitigation of current harmonics in three-phase three-wire shunt active filter with pi controller. *International Journal of Emerging Electric Power Systems*, 18(2):1–29.

Mikkili, S. and Panda, A. K. (2011). Instantaneous active and reactive power and current strategies for current harmonics cancellation in 3-ph 4wire shaf with both pi and fuzzy controllers. *Energy and Power Engineering*, 3(03):285–298.

Mishra, S., Hussain, I., Singh, B., Chandra, A., and Al-Haddad, K. (2017). Frequency adaptive pre filtering stage for differentiation based control of shunt active filter under polluted grid conditions. In *2017 IEEE Industry Applications Society Annual Meeting*, pages 1–8.

Mohebbi, M., McIntyre, M. L., and Latham, J. (2017). A backstepping controller for voltage source inverter with inductor current and output current observers. In *2017 IEEE Power and Energy Conference at Illinois (PECI)*, pages 1–5.

Morain, L. and Dixon, J. (2011). 41 - active filters. In Rashid, M. H., editor, *Power Electronics Handbook (Third Edition)*, pages 1193 – 1228. Butterworth-Heinemann, Boston, third edition edition.

Nejabatkhah, F., Li, Y. W., and Wu, B. (2016). Control strategies of three-phase distributed generation inverters for grid unbalanced voltage compensation. *IEEE Transactions on Power Electronics*, 31(7):5228–5241.

Nielsen, J. (2002). *Design and Control of a Dynamic Voltage Restorer*. PhD thesis.

Nielsen, J. G. and Blaabjerg, F. (2005). A detailed comparison of system topologies for dynamic voltage restorers. *IEEE Transactions on Industry Applications*, 41(5):1272–1280.

Orabi, M., El-Sousy, F., Godah, H., and Youssef, M. Z. (2004). High-performance induction generator-wind turbine connected to utility grid. In *INTELEC 2004. 26th Annual International Telecommunications Energy Conference*, pages 697–704.

Park, S.-W., Chung, I.-Y., Choi, J.-H., Moon, S.-I., and Kim, J.-E. (2003). Control schemes of the inverter-interfaced multi-functional dispersed generation. In *2003 IEEE Power Engineering Society General Meeting (IEEE Cat. No.03CH37491)*, volume 3, pages 1924–1929.

Patel, K. C., Sant, A. V., and Gohil, M. H. (2017). Shunt active filtering with narx feedback neural networks based reference current generation. In *2017 International Conference on Power and Embedded Drive Control (ICPEDC)*, pages 280–285.

Patil, K. and Mehta, B. (2014). Modeling and simulation of variable speed wind turbine with direct drive permanent magnet synchronous generator. In *2014 International Conference on Green Computing Communication and Electrical Engineering (ICGCCEE)*, pages 1–6.

Peng, F. Z., Akagi, H., and Nabae, A. (1990). A new approach to harmonic compensation in power systems-a combined system of shunt passive and series active filters. *IEEE Transactions on Industry Applications*, 26(6):983–990.

Raheni, T. D. and Thirumoorthi, P. (2017). Intelligent control of shunt active power filter for minimization of current harmonics. In *TENCON 2017 - 2017 IEEE Region 10 Conference*, pages 2846–2851.

Rajasekaran, D., Dash, S. S., and Teja, D. R. A. (2011). Dynamic voltage restorer based on fuzzy logic control for voltage sag restoration. In *International Conference on Sustainable Energy and Intelligent Systems (SEISCON 2011)*, pages 26–30.

Ramachandaramurthy, V. K., Arulampalam, A., Fitzer, C., Zhan, C., Barnes, M., and Jenkins, N. (2004). Supervisory control of dynamic voltage restorers. *IEE Proceedings - Generation, Transmission and Distribution*, 151(4):509–516.

Ribeiro, R. L. D. A., Rocha, T. D. O. A., de Sousa, R. M., dos Santos, E. C., and Lima, A. M. N. (2015). A robust dc-link voltage control strategy to enhance the performance of shunt active power filters without harmonic detection schemes. *IEEE Transactions on Industrial Electronics*, 62(2):803–813.

Rubilar, I. A., Espinoza, J. R., Munoz, J. A., and Moran, L. A. (2007). Dc link voltage unbalance control in three-phase upqcs based on npc topologies. In *2007 IEEE Industry Applications Annual Meeting*, pages 597–602.

Ruilin, P. and Yuegen, Z. (2005). Sliding mode control strategy of dynamic voltage restorer. In *2005 International Conference on Industrial Electronics and Control Applications*, pages 1–3.

Saleh, S. A., Moloney, C. R., and Rahman, M. A. (2008). Implementation of a dynamic voltage restorer system based on discrete wavelet transforms. *IEEE Transactions on Power Delivery*, 23(4):2366–2375.

Salimi, M., Soltani, J., and Zakipour, A. (2017). Experimental design of the adaptive backstepping control technique for single-phase shunt active power filters. *IET Power Electronics*, 10(8):911–918.

Samir, A., Taha, M., Sayed, M. M., and Ibrahim, A. (2018). Efficient pv-grid system integration with pv-voltage-source converter reactive power support. *The Journal of Engineering*, 2018(2):130–137.

Slootweg, J. G., de Haan, S. W. H., Polinder, H., and Kling, W. L. (2003). General model for representing variable speed wind turbines in power system dynamics simulations. *IEEE Transactions on Power Systems*, 18(1):144–151.

Tan, K. T., So, P. L., Chu, Y. C., and Kwan, K. H. (2010). Modeling, control and simulation of a photovoltaic power system for grid-connected and stand-alone applications. In *2010 Conference Proceedings IPEC*, pages 608–613.

Toodeji, H., Fathi, S. H., and Gharehpetian, G. B. (2009). Power management and performance improvement in integrated system of variable speed wind turbine and upqc. In *2009 International Conference on Clean Electrical Power*, pages 609–614.

Vahedi, H., Kukandeh, Y. R., Kashani, M. G., Dankoob, A., and Sheikholeslami, A. (2011). Comparison of adaptive and fixed-band hysteresis current control considering high frequency harmonics. In *2011 IEEE Applied Power Electronics Colloquium (IAPEC)*, pages 185–188.

Villalva, M. G., Gazoli, J. R., and Filho, E. R. (2009). Comprehensive approach to modeling and simulation of photovoltaic arrays. *IEEE Transactions on Power Electronics*, 24(5):1198–1208.

Wang, G. D., Wai, R. J., and Liao, Y. (2013). Design of backstepping power control for grid-side converter of voltage source converter-based high-voltage dc wind power generation system. *IET Renewable Power Generation*, 7(2):118–133.

Wang, Y. F. and Li, Y. W. (2013). A grid fundamental and harmonic component detection method for single-phase systems. *IEEE Transactions on Power Electronics*, 28(5):2204–2213.

Wasynczuk, O. (1983). Dynamic behavior of a class of photovoltaic power systems. *IEEE Power Engineering Review*, PER-3(9):36–37.

Wei, F., Zhang, X., Vilathgamuwa, D. M., Choi, S. S., and Wang, S. (2013). Mitigation of distorted and unbalanced stator voltage of stand-alone doubly fed induction generators using repetitive control technique. *IET Electric Power Applications*, 7(8):654–663.

Woodley, N. H., Sundaram, A., Holden, T., and Einarson, T. C. (2000). Field experience with the new platform-mounted dvrtm. In *PowerCon 2000. 2000 International Conference on Power System Technology. Proceedings (Cat. No.00EX409)*, volume 3, pages 1323–1328.

Wu, Y. and Guo, J. (2008). Research on current predictive control for active power filter. In *2008 IEEE International Conference on Industrial Technology*, pages 1–5.

Xiaojie, Y. and Yongdong, L. (2002). A shunt active power filter using dead-beat current control. In *IEEE 2002 28th Annual Conference of the Industrial Electronics Society. IECON 02*, volume 1, pages 633–637 vol.1.

Yi, H., Dai, J., and Wu, J. (2008). Research on modeling and control of the single-phase inverter system with a nonlinear load. In *2008 7th World Congress on Intelligent Control and Automation*, pages 6095–6100.

Zainuri, M. A. A. M., Radzi, M. A. M., Soh, A. C., Mariun, N., and Rahim, N. A. (2016). Dc-link capacitor voltage control for single-phase shunt active power filter with step size error cancellation in self-charging algorithm. *IET Power Electronics*, 9(2):323–335.

Zhili, T. and Dongjiao, Z. (2010). A new control strategy for three-phase four-wire upqc when voltage fluctuating on its dc side. In *The 2nd International Symposium on Power Electronics for Distributed Generation Systems*, pages 190–195.

Appendix A

The parameters considered in the models of wind turbine coupled with PMSG and solar PV modules are given in table A.1 and A.2 respectively.

Table A.1: Parameters of Wind Turbine coupled with PMSG

Parameters	Values
Radius of turbine rotor	3.2 m
Air density	1.225 kg/m^3
Stator resistance	0.05 Ω
d axis inductance	603.3 μH
q axis inductance	666.8 μH
Number of pole pairs	4
Inertia	0.005 kgm^2
Flux linkage established by magnets	0.3 Vs

Table A.2: Parameters of Solar PV Module

Parameters	Values
Nominal open circuit voltage of PV cell	22.2 V
Nominal short circuit current of PV cell	7.52 A
Nominal photo current of PV cell	7.6435 A
Nominal temperature	298 K
Number of series modules	12
Number of parallel modules	10
Number of series cells	36
Temperature co-efficient of current	0.089202 A/K
Temperature co-efficient of voltage	-0.31 V/K
Series resistance of PV cell	0.3431 Ω
Shunt resistance of PV cell	53 Ω

Ratings of Wind and Solar Energy Systems

The power output of a wind energy system is given by (A.1).

$$P_w = \frac{1}{2}\rho A v_w^3 C_P \eta \tag{A.1}$$

The maximum power output is calculated by substituting the design parameters shown in Table A.1 in (A.1).

$$P_{wmax} = \frac{1}{2} \times 1.225 \times (\pi \times 3.2^2) \times 12^3 \times 0.45 \times 0.95 \approx 15 kWp \tag{A.2}$$

The rated power of a single PV module considered in this study is 120 W. Connecting 12 such modules in series and 10 in parallel, total power rating of solar energy system is $\approx$ 15 kWp.

Selection of V_{dc}

The value of DC-link voltage is selected using the inequality shown in (A.3).

$$\left(\sqrt{2}V_s\right) < V_{dc} < \left(1.5 \times \sqrt{2}V_s\right) \tag{A.3}$$

Substituting the known values,

$$\left(\sqrt{2} \times 415\right) < V_{dc} < \left(1.5 \times \sqrt{2} \times 415\right) \tag{A.4}$$

$$(586.89)) < V_{dc} < (880.34)) \tag{A.5}$$

Select V_{dc}= 700 V.

Selection of Inverter

The maximum power generated by RES $\approx$ 30 kW

Considering 10% overload capacity and the switching and conduction losses, volt-ampere rating of the grid interfacing inverter is taken as 35 kVA

Maximum voltage stress on the inverter switch = V_{dc} = 700 V.

Maximum current flow through the inverter = $\sqrt{2}\dfrac{35 \times 10^3}{\sqrt{3} \times 415} \approx 68.86A.$

Maximum switching frequency of inverter should be greater than twice the frequency of highest harmonic current to be compensated. Selected an inverter of maximum switching frequency 10 kHz.

Selection of C_{dc}

The value of DC-link capacitor is selected using (A.6).

$$C_{dc} \geq \frac{S}{2\omega V_{dc}\Delta V_{dc}} \tag{A.6}$$

$$C_{dc} \geq \frac{35 \times 10^3}{2 \times 2 \times 50 \times 700 \times 0.05 \times 700} \geq 2273.6\mu F \tag{A.7}$$

Selected 2350 μF

Selection of L_f

The filter inductance is calculated using (A.8).

$$L_f = \frac{V_{dc}}{6hf_{max}} = \frac{700}{6 \times 0.05 \times 55 \times 10 \times 10^3} \approx 5mH \tag{A.8}$$

Selection of boost converter components

The design equations for boost converter are shown in (A.9) and (A.10).

$$L_b = \frac{V_i d}{2\Delta I_i f_s} = \frac{306 \times 0.56}{2 \times 0.05 \times 20.8 \times 10 \times 10^{-3}} \approx 10mH \tag{A.9}$$

$$C_b = \frac{I_o d^2}{(\Delta V_o)(1-d)f_s} = \frac{14 \times 0.83^2}{(0.01 \times 700)(1-0.83) \times 10 \times 10^{-3}} \approx 2000\mu F \tag{A.10}$$

Appendix B

For a sinusoidal signal $x(t) = A\sin(\omega t + \phi)$, the amplitude integration output can be written as $y(t) = At\sin(\omega t + \phi)$. $x(t)$ can be expanded as shown in (B.1) and the Laplace transforms of $x(t)$ can be written as (B.2). Consider an auxiliary signal $x_c(t) = A\cos(\omega t + \phi)$. The Laplace transform of $x_c(t)$ is shown in (B.3). The Laplace transforms of $y(t)$ can be written as (B.4).

$$x(t) = A(\sin \omega t \cos \phi + \cos \omega t \sin \phi) \tag{B.1}$$

$$X(s) = A(\frac{\omega}{s^2 + \omega^2} \cos \phi + \frac{s}{s^2 + \omega^2} \sin \phi) \tag{B.2}$$

$$X_c(s) = A\{\frac{s}{s^2 + \omega^2} \cos \phi - \frac{\omega}{s^2 + \omega^2} \sin \phi\} \tag{B.3}$$

$$Y(s) = -\frac{d}{ds}X(s) = A\{\frac{2\omega s}{(s^2 + \omega^2)^2} \cos \phi + \frac{2s^2}{(s^2 + \omega^2)^2} \sin \phi - \frac{s^2 + \omega^2}{(s^2 + \omega^2)^2} \sin \phi\} \tag{B.4}$$

$Y(s)$ can be re arranged as shown in (B.5).

$$Y(s) = \frac{As}{s^2 + \omega^2}\{\frac{\omega}{s^2 + \omega^2} \cos \phi + \frac{s}{s^2 + \omega^2} \sin \phi\} + \frac{A\omega}{s^2 + \omega^2}\{\frac{s}{s^2 + \omega^2} \cos \phi - \frac{\omega}{s^2 + \omega^2} \sin \phi\} \tag{B.5}$$

From (B.5), we get (B.6). The sinusoidal integrator can be configured as shown in Figure B.1.
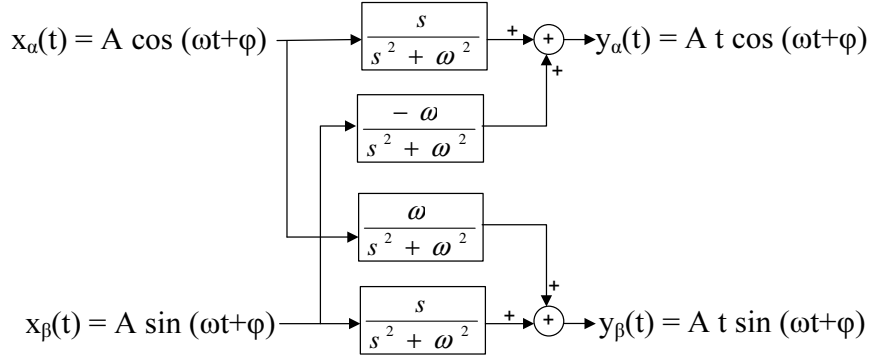
$$Y(s) = \frac{s}{s^2 + \omega^2}X(s) + \frac{w}{s^2 + \omega^2}X_c(s) \tag{B.6}$$

The resonance frequency of integrator is 'ω'. The integral output is negligible for
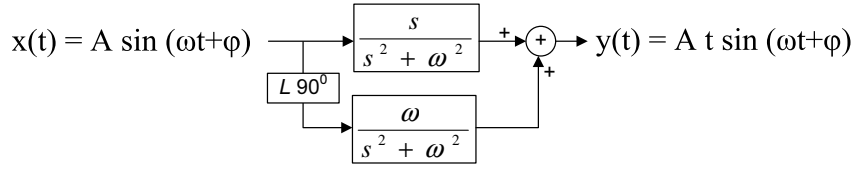
Figure B.1: Integrator for a sinusoidal signal

$$x(t) = A \sin(\omega t + \varphi) \quad \boxed{\dfrac{s}{s^2 + \omega^2}} \quad \oplus \quad y(t) = A\, t \sin(\omega t + \varphi)$$

Figure B.2: Integrator for signals in $\alpha\beta$ frame

frequency components other than 'ω'.

For signals in $\alpha\beta$ frame, with α axis leads β axis by 90^0, a positive sequence integrator can be implemented as shown in Figure B.2. The transfer function of integrator for signals in $\alpha\beta$ frame, $H(s)$ can be written as (B.7).

$$H(s) = \frac{s + j\omega}{s^2 + \omega^2} \tag{B.7}$$

SELF TUNING FILTER IN $\alpha\beta$ FRAME

A negative feedback to the positive sequence signal integrator makes it a self tuning filter. A constant K can be included in the transfer function, for controlling response time and bandwidth. The transfer function of STF, H_{STF} is shown in (B.8). The STF can be implemented as shown in Figure B.3.

$$H_{STF}(s) = K \frac{s + K + j\omega}{(s + K)^2 + \omega^2} \tag{B.8}$$

The attenuation of the signal is zero only at fundamental frequency. The phase
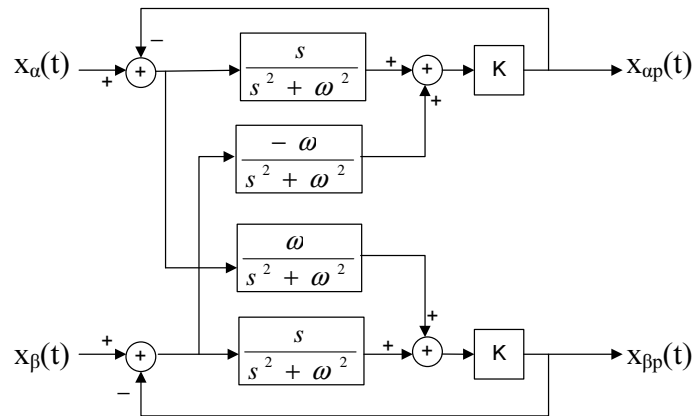
Figure B.3: Self tuning filter

delay is also zero at fundamental frequency. The frequency response is similar to a filter, with no phase delay at cut off frequency.

Appendix C

Table C.1: Specification of IGBT

Symbol	Description	Condition	Rating
V_{CES}	Collector to Emitter Voltage	$T_j = 25^0$ C	1200 V
V_{GES}	Gate to Emitter Voltage		± 20 V
I_C	Collector Current	$T_C = 25^0$ C	115 A
		$T_C = 80^0$ C	88 A
I_{Cnom}	Nominal Collector Current		75 A
T_j	Junction Temperature		-40 to 175^0 C

Table C.2: Specification of Free Wheeling Diode

Symbol	Description	Condition	Rating
V_{RPM}	Max. Reverse Repetitive Voltage	$T_j = 25^0$ C	1200 V
I_F	Forward Current	$T_C = 25^0$ C	97 A
		$T_C = 80^0$ C	73 A
I_{Fnom}	Nominal Forward Current		75 A
T_j	Junction Temperature		-40 to 175^0 C

Appendix D

The hall effect voltage transducer is used for the electronic measurement of voltages like DC, AC, pulsed voltage, with a galvanic isolation between the primary circuit (high voltage) and secondary circuit (electronic circuit).

Features

- Closed loop (compensated) voltage transducer using the Hall effect.
- Insulating plastic case recognized according to UL 94-V0.

Principle

For voltage measurements, a current proportional to the measured voltage is passed through an external resistance connected in series with the primary circuit of the transducer.

Advantages

- Excellent accuracy
- Very good linearity
- Low thermal drift
- Low response time
- High bandwidth
- High immunity to external interference
- Low disturbance in common mode

Electrical specifications

<div align="center">

Table D.1: Electrical specifications of LV 25-P

</div>

Parameters		Values	
I_{PN}	Primary nominal rms current	10 mA	
I_{PM}	Primary current, measuring range	0 to $\pm$ 14 mA	
R_M	Measuring resistance	R_{Mmin}	R_{Mmax}
	with $\pm$ 12 V @ $\pm$ 10 mA$_{max}$	30 Ω	190 Ω
	with $\pm$ 12 V @ $\pm$ 14 mA$_{max}$	30 Ω	100 Ω
	with $\pm$ 15 V @ $\pm$ 10 mA$_{max}$	100 Ω	350 Ω
	with $\pm$ 15 V @ $\pm$ 14 mA$_{max}$	100 Ω	190 Ω
I_{SN}	Primary nominal rms current	25 mA	
K_N	Conversion ratio	2500:1000	
I_c	Current consumption	10(@ $\pm$ 15 V)+I_s mA	

HALL EFFECT CURRENT SENSOR LA 55-A

The hall effect voltage transducer is used for the electronic measurement of currents like DC, AC, pulsed current, with a galvanic isolation between the primary circuit and the secondary circuit.

Features

- Closed loop (compensated) current transducer using the Hall effect.
- Insulating plastic case recognized according to UL 94-V0.

Advantages

- Excellent accuracy
- Very good linearity
- Low temperature drift
- Optimized response time
- Wide frequency bandwidth
- No insertion losses
- High immunity to external interference

- Current overload capability

Table D.2: Electrical specifications of LA 55-P

Parameters		Values			
I_{PN}	Primary nominal rms current	50 A			
I_{PM}	Primary current, measuring range	0 to $\pm$ 70 A			
R_M	Measuring resistance	T_A = 70 ^{0}C		T_A = 85 ^{0}C	
		R_{Mmin}	R_{Mmax}	R_{Mmin}	R_{Mmax}
	with $\pm$ 12 V @$\pm$ 50 A$_{max}$	10 Ω	100 Ω	60 Ω	95 Ω
	with $\pm$ 12 V @$\pm$ 70 A$_{max}$	10 Ω	50 Ω	60 [1] Ω	60 [1] Ω
	with $\pm$ 15 V @$\pm$ 50 A$_{max}$	50 Ω	160 Ω	135 Ω	155 Ω
	with $\pm$ 15 V @$\pm$ 70 A$_{max}$	50 Ω	90 Ω	135 [2] Ω	135 [2] Ω
I_{SN}	Primary nominal rms current	50 mA			
K_N	Conversion ratio	1:1000			
I_c	Current consumption	10(@$\pm$ 15 V)+I_s mA			

[1] Measuring range limited to $\pm$60 A$_{max}$

[2] Measuring range limited to $\pm$55 A$_{max}$

Appendix E

The Basys 3 board is a complete, ready-to-use digital circuit development platform based on Artix-7 Field Programmable Gate Array (FPGA) from Xilinx. With its high-capacity FPGA (Xilinx part number XC7A35T- 1CPG236C), low overall cost, and collection of USB, VGA, and other ports, the Basys 3 can host designs ranging from introductory combinational circuits to complex sequential circuits like embedded processors and controllers.

It includes a single 100 MHz oscillator, sixteen slide switches, five push buttons, sixteen individual LEDs, a four-digit seven-segment display, and Pmod ports. The Basys-3 FPGA Board is shown in Figure E.1. The description on different components of the FPGA board are given in table E.1.
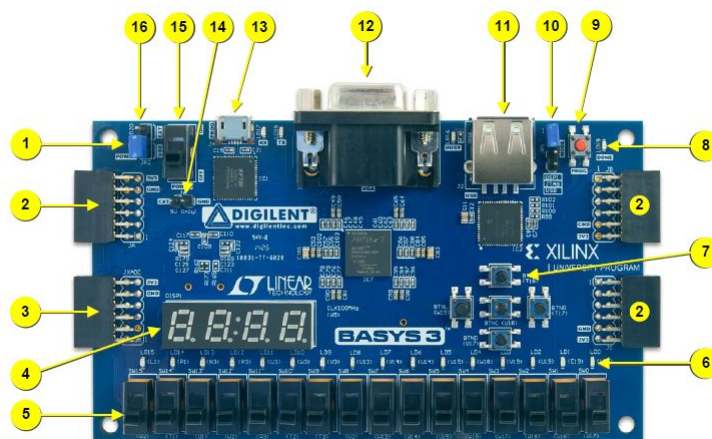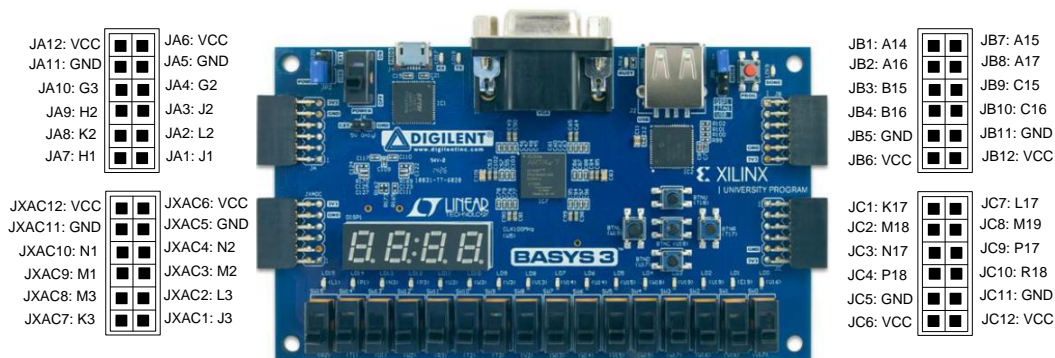

Figure E.1: Basys-3 FPGA Board (*Source: Basys 3^{TM} FPGA Board Reference Manual*)

129

Table E.1: Callouts and component descriptions

Call out	Component description	Call out	Component description
1	Power good LED	9	FPGA configuration reset button
2	Pmod port(s)	10	Programming mode jumper
3	Analog signal Pmod port (XADC)	11	USB host connector
4	Four digit 7-segment display	12	VGA connector
5	Slide switches (16)	13	Shared UART/ JTAG USB port
6	LEDs (16)	14	External power connector
7	Pushbuttons (5)	15	Power Switch
8	FPGA programming done LED	16	Power Select Jumper

The Basys-3 FPGA based designs can be expanded using Digilent Pmods or other custom boards and circuits. The Pmod ports are arranged in a 2×6 right-angle, and are 100-mil female connectors that mate with standard 2×6 pin headers. Each 12-pin Pmod port provides two 3.3 V VCC signals (pins 6 and 12), two Ground signals (pins 5 and 11), and eight logic signals. The VCC and Ground pins can deliver up to 1A of current. Pmod data signals are not matched pairs, and they are routed using best-available tracks without impedance control or delay matching. The on-board Pmod expansion port, labeled "JXADC", is wired to the auxiliary analog input pins of the FPGA. Depending on the configuration, this connector can be used to input differential analog signals to the analog-to digital converter inside the Artix-7 (XADC). Any or all pairs in the connector can be configured either as analog input or digital input-output. Pin assignments for the Pmod I/O connected to the FPGA are shown in Figure E.2.

Figure E.2: Pmod Pin-out Diagram (*Source: Basys 3^{TM} FPGA Board Reference Manual*)

Curriculum Vitae

Address for correspondence:	JAYASANKAR V N VADAKKE NEELAMANA, M.M. BAZAR (P .O), KANNUR, KERALA-670306. Email : jayasankarvn@gmail.com Landline: 04985277566 Contact No: +91-8050243818
Educational Qualifications:	M. Tech in Power Systems, from National Institute of Technology Calicut, Kerala. B. Tech in Electrical & Electronics Engineering, from Government College of Engineering Kannur, Kannur University
Areas of Research Interest:	Renewable Energy, Power Quality and Application of Power Electronics in Power Systems.
Languages Known :	English (Professional working proficiency) Malayalam (Native proficiency)
Packages Known:	MATLAB, HOMER, Xilinx Vivado Design Suite, LT-Spice, PSCAD, Mi-Power.
Achievements :	Best paper award in 2nd International Conference on Systems, Energy and Environment, Kannur, India, Dec. 2017
Job Experience:	Research Scholar, NITK Surathkal, Dec. 2014-Present Adhoc Faculty, NITK Surathkal, Jul. 2014-Dec. 2014 Power System Engineer, Sep. 2012-Mar. 2014

List of Publications

INTERNATIONAL JOURNALS

1. Jayasankar, V.N. and Vinatha, U. (2018). Design of Back Stepping Controller for PV–Wind Hybrid System with Grid–interfacing and Shunt Active Filter Functionality. *International Journal of Power Electronics, Inderscience Publishers*, 9(2), 167–188. (*Indexed in Scopus*)

2. Jayasankar, V.N. and Vinatha, U. (2018). Advanced Control Approach for a Shunt Active Filter Interfacing Wind-Solar Hybrid Renewable System to Distribution Grid. *Journal of Electrical Systems (JES)*, 14(2), 88–102. (*Indexed in Scopus and Web of Science*)

INTERNATIONAL CONFERENCE PROCEEDINGS

1. Gururaj, M. V., Vinatha, U. and Jayasankar, V. N. (2015). Interconnection of wind–solar hybrid Renewable Energy source to the 3 phase–3 wire distribution system along with power quality improvements at the grid side. *2015 IEEE International Conference on Power and Advanced Control Engineering (ICPACE)*, pages 168–172. (*Indexed in Scopus*)

2. Aravind, S., Vinatha, U., and Jayasankar, V. N. (2016). Wind–solar grid connected renewable energy system with series active self tuning filter. *2016 IEEE International Conference on Electrical, Electronics, and Optimization Techniques (ICEEOT)*, pages 1944–1948. (*Indexed in Scopus*)

3. Jayasankar, V.N., Gururaj, M. V., and Vinatha, U. (2016). A study on hybrid Renewable Energy Source interface to the non-ideal grid at distribution level with

power quality improvements. *2016 IEEE 6th International Conference on Power Systems (ICPS)*, pages 1–5.(*Indexed in Scopus*)

4. Jayasankar, V.N. and Vinatha, U. (2016). Implementation of adaptive fuzzy controller in a grid connected wind-solar hybrid energy system with power quality improvement features. *2016 IEEE Biennial International Conference on Power and Energy Systems: Towards Sustainable Energy (PESTSE)*, pages. 1–5.(*Indexed in Scopus*)

5. Jayasankar, V.N., Nisha, B. Kumar, and Vinatha, U. (2017). Grid Connected Hybrid Wind-Solar System with Shunt Active Filter Functionality. *2nd International Conference on Systems, Energy and Environment (ICSEE 2017)*, pages 265–270. (*Achieved Best Paper Award*)

6. Jayasankar, V.N., Nisha, B. Kumar, and Vinatha, U. (2017). Enhancement of Load Voltage Compensation using Positive Sinusoidal Sequence Regulator in Fuzzy Logic Controlled Three Phase Series Active Filter. *2017 IEEE International (biennial) Conference on Technological Advancements in Power $\&$ Energy – TAP Energy 2017*, pages 1–6. (*Indexed in Scopus*)

7. Jayasankar, V.N., Nisha, B. Kumar, and Vinatha, U. (2018). Design of Backstepping Controller for a Three-phase Shunt Active Filter Interfacing Solar Photovoltaic System to Distribution Grid. 8th *IEEE International Conference on Power Electronics, Drives and Energy Systems (PEDES-2018)*.

8. Nisha, B. Kumar, Jayasankar, V.N., and Vinatha, U. (2019). PI Control Based DC Link Voltage Controller for Grid Integrated Domestic Photo Voltaic Systems. 2nd *IEEE International Conference on Innovations in Power and Advanced Computing Technologies (i-PACT 2019)*(accepted for oral presentation to be held at VIT Vellore , TN ,22-23 March 2019).

9. Pavana Bhat, Disha Shetty, Jayasankar V.N., and Vinatha U (2019). Design and FPGA Implementation of Dual Self-Tuning Filter based Controller for Single Phase Shunt Active Filter. 2nd *IEEE International Conference on Innovations in Power and Advanced Computing Technologies (i-PACT 2019)*(accepted for oral presentation to be held at VIT Vellore , TN ,22-23 March 2019).